

Understanding the microscale spatial distribution and mineralogical residency of Re in pyrite: Examples from carbonate-hosted Zn-Pb ores and implications for pyrite Re-Os geochronology

Danny Hnatyshin^a, Robert A. Creaser^a, Sebastien Meffre^b, Richard. A Stern^a, Jamie J. Wilkinson^{c,d}

^aDepartment of Earth and Atmospheric Sciences, University of Alberta, Edmonton, Alberta

^b CODES – Centre for Ore Deposits and Earth Sciences, University of Tasmania, Hobart, TAS, Australia

^cLODE, Department of Earth Sciences, Natural History Museum, London SW7 5BD, UK

^dDepartment of Earth Science and Engineering, Imperial College London, SW7 2AZ, UK

Keywords: Re-Os geochronology; LA-ICPMS; Zn-Pb ore deposits; Sulfur isotopes; Pyrite; Lisheen

Abstract

Accurate and precise geochronology using the Re-Os isotopic system in pyrite is an invaluable tool for developing and confirming genetic models of ore systems. However, as a bulk method, the results produced by pyrite Re-Os geochronology are commonly complex, and many imprecise isochrons exist in the literature. Using LA-ICPMS methods it is now possible to map and quantify Re distribution at the ppb level, allow an unprecedented look into the Re-Os systematics of pyrite bearing ore.

Two samples from the Lisheen Zn-Pb ore deposit in Ireland showing disparate Re-Os isotopic behavior were investigated. In-situ sulfur isotope measurements using SIMS, an analytical technique not previously attempted on the Irish deposits, was used to supplement the Re-Os dataset. A massive pyrite sample from the Main Zone was used to produce a precise, low-scatter isochron (346.6 ± 3.0 Ma, MSWD = 1.6). The Re distribution in this sample is relatively homogeneous, with the Re budget dominated by pyrite containing 1-5 ppb Re, and $\delta^{34}\text{S}$ ranging from -45.2 ‰ to 8.2 ‰. A second, more paragenetically complex, sample from the Derryville Zone produced a younger age with high scatter (322 ± 11 Ma, MSWD = 206) and a large variation in $\delta^{34}\text{S}$ (-53 ‰ to +4 ‰). The cores of grains of main-stage iron sulfide are depleted in trace elements and show low Re abundances (< 10 ppb) but have been altered in an irregular fashion leading to Re-enriched domains that exceed 100 ppb. Additionally, micron-scale molybdenite crystals, found in close association with altered sulfides, contains Re at levels that locally exceed 10 ppm. The highly scattered (MSWD = 206), younger age (322 Ma), produced by the Derryville

Zone sample therefore resulted from mixing of different generations of sulfide and potentially from fluids associated with Variscan deformation (< 310 Ma). The Re-Os data produced from the Derryville Zone sample does not reflect the timing of iron sulfide mineralization, even though a relatively precise date was obtained.

A second Re-Os dataset from Zn-Pb mineralization at Hawker Creek, Nunavut, Canada was produced from massive pyrite that displays low Re concentrations (< 1 ppb). On grain boundaries, and in fractures, however, silicate-rich material contains Re at levels that can locally exceed 500 ppb. Analyses of fracture-free pyrite produced by bulk separation using magnetic separation yielded the oldest model age (1083 Ma), whereas mineral separates containing the highest fracture density produce the youngest age (413 Ma).

In general, therefore, the complexities of pyrite Re-Os geochronology can result from impurities in mineral separates. Attempts to eliminate impurities through different mineral separation techniques (e.g. crushing, heavy liquid separation, magnetic separation, acid leaching) are frequently only partially successful, and therefore full characterization of any resulting mineral separates is extremely important. We conclude that LA-ICPMS mapping of Re and Mo distributions is essential for the identification of such impurities. Although other trace element LA-ICPMS maps, in-situ sulphur isotope measurements, and petrographic evidence were of limited use in assessing the Re budget of a sample, they are invaluable in linking the documented Re distribution obtained through LA-ICPMS to Re-Os geochronological results.

Introduction

The determination of accurate and precise geochronology for ore-forming processes is a critical component for developing genetic models of ore formation. This is because such models appeal to tectonics, magmatism, and/or sedimentary basin evolution as large-scale controls on ore formation, but these linkages can be difficult to prove without robust age constraints. Pyrite Re-Os geochronology is becoming a widely used method for dating many types of ore systems, stemming from the near-ubiquity of pyrite and similar minerals (e.g. arsenopyrite) associated with ore-stage mineralization in many ore types. Importantly, the Re-Os system in these minerals has been shown to remain robust through post-mineralization thermal and metamorphic disturbances (Morelli et al., 2010; van Acken et al., 2014; Vernon et al., 2014). As a result, pyrite Re-Os geochronology has been widely and successfully used to date a large variety of ore types including orogenic gold, porphyry, SEDEX, and MVT deposits (e.g. Stein

et al., 2000; Morelli et al., 2004; Lawley et al., 2013; Hnatyshin et al., 2015; Zhang et al., 2016). Many examples have produced geologically plausible ages with relatively high precision (age uncertainty of < 10%) and low scatter in the data, with isochron regressions having MSWD < 10.

Although several studies have produced results with high degrees of scatter and/or imprecise ages (e.g. Liu et al., 2004; Munha et al. 2005; Mathur et al., 2008; Hnatyshin et al., 2016; Ding et al., 2016; Jiang et al., 2017), comparatively little effort has been expended to understand the fundamental causes of such scatter or imprecision, and how it affects the interpretation Re-Os isotopic data. This is, in part, due to the lack of understanding of the Re-Os systematics of pyrite and related minerals.

In a similar spirit to prior studies dedicated to refining the Re-Os systematics and processing protocols for molybdenite and organic-rich sediments (Stein et al., 2003; Selby and Creaser, 2003, 2004; Yin et al., 2017), we have investigated the Re-Os systematics of pyrite from carbonate-hosted Zn-Pb ores to understand the controls on Re-Os isochron quality and to evaluate methods that can be used to improve sample screening/processing techniques. Processing techniques are also scrutinized to determine their efficiency at producing the pure mineral separates used for Re-Os geochronology. To accomplish these goals, we characterize samples through bulk (petrography, Re-Os isotopes, trace elements, magnetic susceptibility) and microanalytical (S isotopes via SIMS, trace element mapping via LA-ICPMS) techniques, with the objectives of determining the mineralogical residence and spatial distribution of Re, and hence radiogenic ^{187}Os within the ore. Herein, both published (Hnatyshin et al., 2015; Hnatyshin et al., 2016) and unpublished datasets from carbonate-hosted Zn-Pb deposits are investigated: Lisheen from Ireland, and Hawker Creek from Baffin Island in Canada. These samples were chosen because previous studies on these samples used well-documented analytical protocols, and produced contrasting levels of precision in derived Re-Os ages.

Sample selection

The Lisheen deposit from Ireland was chosen for detailed investigation because pyrite from this deposit produced one of the most precise pyrite Re-Os ages reported in the literature (346.6 ± 3.0 Ma; Hnatyshin et al., 2015). Scrutinizing the sample (8S08FW) that yields this precise age provides insights into the Re-Os and mineralogical characteristics that may make a sample suitable for high-precision Re-Os dating. A sample from Lisheen that has a much more complex paragenesis and greater scatter in Re-Os systematics is also studied (LK 359), to investigate how a complex paragenesis may affect the precision and accuracy of Re-Os geochronology.

The Hawker Creek prospect from Baffin Island consists primarily of massive pyrite, and is broadly similar to the Lisheen sample that produced a precise isochron. However, the Re-Os data from the Hawker Creek sample produced an uninterpretable isochron (295 ± 250 Ma, Initial $^{187}\text{Os}/^{188}\text{Os} = 49 \pm 41$, MSWD = 139), although model ages from individual samples suggested that there may be mixing between two end-member components with ages of ~ 1100 Ma and ~ 400 Ma (Hnatyshin et al., 2016). A critical test of our capability to deconstruct the origin of scatter present in a Re-Os pyrite dataset lies in our ability to identify with confidence these two end members in the Hawker Creek sample.

Study location 1: Lisheen, Ireland

Background

Lisheen is the second-largest base-metal deposit in Ireland and is summarized below using the descriptions provided by Hitzman et al. (2002), Wilkinson et al. (2005), and Riegler and McClenaghan (2017). Lisheen consists of a series of stratabound sulfide lenses divided into the Main Zone, Derryville Zone, and Bog Zone, with each zone being controlled by its own normal fault (Fig. 1B). Ore is primarily hosted by the Waulsortian Limestone Formation in the hangingwall of normal faults, with a smaller proportion of the ore hosted by the Lisduff Oolite Member of the Ballysteen Limestone Formation in the footwall.

Mineralization

The general paragenesis (Fig. 2A) for Lisheen is constructed using our interpretation of the evidence provided by Hitzman et al. (2002), Wilkinson et al. (2005), and Riegler and McClenaghan (2017), as well as the smaller sample set used in this study (8S08FW and LK 359) and in that of Creaser et al. (2009) (LK 451). The onset of mineralization at Lisheen is marked by widespread dolomitization and brecciation of the host limestone. The first stage of sulfide mineralization is represented by minor amounts of disseminated pyrite associated with the earliest stages of dolomitization (D1 in Wilkinson et al., 2005) of the Waulsortian Limestone Formation. A later stage of dolomitization (D2) is associated with greater abundances of fine-grained pyrite and sphalerite. Pyrite mineralization is the most abundant sulfide during the early stages of hydrothermal activity (LG1-LG2). Early pyrites are locally overgrown by colloform bands of new iron sulfides (pyrite and marcasite) that contain minor amounts of sphalerite, which preferentially replaced individual iron sulfide framboids, dolomite, and galena (LG2-LG3). The colloform iron sulfide bands transition into an assemblage that is dominated by colloform sphalerite (LG3) and this marks the boundary between the pre-ore and main ore stages defined by

Wilkinson et al. (2005). Following the precipitation of colloform sphalerite, an assemblage of sphalerite, galena, tennantite and blocky dolomite developed (LG4). Two other major ore-stage assemblages have been identified. The first is sphalerite ± galena ± dolomite ± quartz ± barite that either infills vugs or occurs in crosscutting veins (LG5). Cross-cutting LG5 is an assemblage of primarily composed of sphalerite and illite (LG6). Late-stage mineralization includes minor Cu-sulfides, arsenopyrite and tennantite that locally replace other sulfides, but were not observed in this study. The Lisduff Oolite mineralization is generally similar to that observed in the Waulsortian Limestone, with the only major difference being that the earliest stage of sulfide mineralization is characterized by massive pyrite (LG1) that has replaced the host oolitic limestone.

Sample Description and Background

8S08FW

The Re-Os data from 8S08FW referenced here are from Hnatyshin et al. (2015), to which we have added trace element and sulfur isotope data for this study. 8S08FW is from the Lisduff Oolite member of the Ballysteen Formation at a depth of 176 m in the Main Zone at Lisheen and is composed primarily of LG1 pyrite containing small (<5 µm) sphalerite and galena inclusions (Hnatyshin et al., 2015; Fig. 3B). LG1 pyrite is very rarely crosscut by coarser galena crystals (> 100 µm) that are possibly from stage LG5, and more commonly cross-cut by calcite veins (LG7). Localized areas in LG1 pyrite contain fractures containing K-rich silicates, which suggest they may be part of the LG6 assemblage.

LK 359

Sample LK 359 contains a different textural type of iron sulfide to 8S08FW (LG2 rather than LG1) and is a more paragenetically complex sample (Fig. 2, Fig. 4). This sample was collected in the Derryville Zone from massive sulfide ore at a depth of 143.6 m within the Waulsortian Limestone Formation and is composed primarily of pyrite, marcasite, sphalerite, and illite. Brecciation and replacement of LG2 marcasite by LG6 sphalerite and illite is the dominant feature observed (Figs. 4B, C). The paragenetic sequence LG1-LG3 is well represented locally (Fig. 4D) and these domains are often veined by LG5 sphalerite and dolomite (Fig. 4B).

Study Location 2: Hawker Creek, Baffin Island, Canada

Background

The Mesoproterozoic Borden Basin of Baffin Island, Nunavut, Canada is known for its extensive, Zn-Pb mineralization. Although the past-producing Nanisivik mine was the largest known example of Zn-Pb mineralization, numerous smaller base-metal showings are present southeast of Nanisivik (e.g. Hawker Creek; Fig. 5). The geologic history of the region is complex and is summarized in the studies of Jackson and Innaelli (1981), Turner (2009, 2011), and Turner et al. (2016).

The predominant ore texture in these massive sulfide lenses is alternating bands of pyrite, sphalerite, galena, and dolomite that replaced dolostone of the Nanisivik Formation (Olson, 1984; Arne et al., 1991; Turner, 2011). The relative timing of the sulfides differs depending on the location sampled; Olson (1984) reported pyrite replacing sphalerite/galena, whereas Arne et al. (1991) described the opposite sequence. A minor proportion of the sulfides are fracture-hosted, vug-filling, or disseminated in the host rock. It is widely assumed that both Nanisivik and Hawker Creek formed contemporaneously at ~1100 Ma (Olson, 1984; Christensen et al., 1993; Symons et al. 2000; Hnatyshin et al., 2016).

Sample description and background

03-HC-8D

Sample 03-HC-8D is one of two samples used in Hnatyshin et al. (2016) to produce Re-Os model ages for Hawker Creek and is a relatively simple rock consisting primarily of massive pyrite with thin, semi-continuous bands of sphalerite (Fig. 6A). The sulfides minerals are primarily anhedral, and locally exhibit localized areas that are highly fractured (Fig. 6B). Backscattered electron (BSE) images show that much of this rock contains high concentrations of small (< 30 μm) inclusions of sphalerite and pyrrhotite (Hnatyshin et al., 2016).

Individual mineral separates from Hnatyshin et al. (2016) contain a wide range of Re-Os model ages, from 413 Ma to 805 Ma for 03-HC-8D, and 943 to 1083 Ma for 03-HC-8F (Table 4). The younger ages appeared to correlate with pyrite that exhibited higher fracture density, magnetic susceptibility and Re abundances. Based on these characteristics, and slightly different sulfur isotopic compositions, Hnatyshin et al. (2016) suggested that there were two stages of pyrite formation at ~1100 Ma and ~400 Ma. For the present study we studied 03-HC-8D in more detail, mapping Re distribution using LA-ICPMS to test this hypothesis.

Methods

Sample preparation and characterization

Because Re-Os pyrite geochronology is a bulk method, using up to 0.4 g of pyrite per analysis point, the sample preparation method is a critical step to ensure low abundances of impurities and that any isotopic analyses subsequently performed are on paragenetically-constrained separates. Preparation starts with the selection of samples of sufficient size to produce several grams of pyrite, with excess material (e.g. host rock) being removed with a rock saw. The remaining sample is then polished to remove weathering products and any contaminants ingrained into the rock from the rock saw. Samples are crushed and sieved in a manner to minimize the use of metallic components, which reduces the risk of contamination by steel that may contain ppb level Re and hundreds of ppt Os (R.A. Creaser, unpubl. data). First, the sample is wrapped in plastic and broken into $\sim 1 \text{ cm}^3$ pieces using a Duct Tape-wrapped hammer. An alumina ceramic grinding mill (SPEX 8505) further crushes the sample until it passes through disposable nylon sieve material (74-210 μm particle size) held between disposable HDPE food containers. This size distribution was chosen to allow grains to be easily filtered when being processed through heavy liquid procedures, as well as being an appropriate size for magnetic separation using a Frantz isodynamic separator. Directly following the crushing procedure, a hand magnet was passed over the sample to remove highly magnetic minerals (e.g. magnetite) and metallic contaminants.

To remove the majority of silicates and carbonates from a crushed sample, a heavy liquid separation procedure was used to exploit differences in mineral densities. For this study, methylene iodide (CH_2I_2) was used (density of 3.32 g/cm^3) to separate sulfides from carbonates and silicates.

To take advantage of the possible differences in magnetic susceptibility between different minerals, or mineral compositions, a Frantz isodynamic separator was used to produce a variety of mineral separates, each with a different bulk magnetic susceptibility.

A final experimental purification step applied to some samples involved using hydrochloric acid (0.2 N to 10 N) to dissolve impurities from the mineral separate (e.g. calcite, dolomite, sphalerite, galena, oxides). During the leaching process, acids were added to a crushed sample in a 22 mL borosilicate glass vial, either at either room temperature ($\sim 21^\circ\text{C}$) or at $\sim 80^\circ\text{C}$. After ~ 24 hours, the acid was decanted, and the sample was rinsed a total of four times, three times with milli-Q water and once with ethanol, to ensure no residual acid was present. Leaching procedures were first tested on pure mineral separates provided by the Mineralogy and Petrology Collection from the University of Alberta,

to determine the conditions required to dissolve various minerals (i.e. calcite, dolomite pyrite, sphalerite, galena, and magnetite), the results of which are shown in Figure A1. To test for possible effects of HCl leaching on the Re-Os isotope system, sample 8S08FW from Hnatyshin et al. (2015) was used. This sample yielded a precise isochron, so any preferential leaching of Re or Os from pyrite during acid dissolution should be easily demonstrated by plotting these analyses relative to the unleached isochron samples.

To determine the efficiency of these procedures, the modal abundances of minerals in representative mineral separates are compiled in Table 1. To determine the distribution of different paragenetic stages of iron sulfide within the mineral separates they were visually inspected using optical microscopy and SEM-BSE imaging and assessed using bulk chemistry and SIMS sulfur isotope measurements.

ICP-MS analysis

Bulk compositions of several mineral separates were analyzed for major, minor, and trace elements. Sample preparation consisted of digesting ~200 mg of sample using an 8N nitric acid solution. This solution was analyzed at the University of Alberta using a Perkin Elmer Elan 6000 Quadrupole Inductively Coupled Plasma Mass Spectrometer at the University of Alberta was used to analyze the major, minor, and trace elements. Element calibration was done with a DNC-1 silicate standard, with dwell times (10 – 20 ms) and integration times (350 – 700 ms) were selected to optimize counting statistics for each element.

Re-Os analytical procedure

All material prepared for Re-Os analysis were chemically purified and analyzed in the Crustal Re-Os Geochronology Laboratory at the University of Alberta. Chemical purification of Re and Os was accomplished by following the isotope dilution procedure outlined in Hnatyshin et al. (2016). The samples were then analyzed using a thermal ionization mass spectrometer (TIMS) running in negative ion mode using the sample preparation and analytical conditions specified in Hnatyshin et al. (2016). All age determinations were performed using Isoplot version 3.00 (Ludwig, 2003).

Sulfur isotope sample preparation

Sample preparation and SIMS analyses were carried out at the Canadian Centre for Isotopic Microanalysis (CCIM), University of Alberta, using the method described in Hnatyshin et al. (2016).

Briefly, pyrite mineral separates and rock fragments were co-mounted in 25 mm diameter epoxy assemblies along with fragments of CCIM pyrite reference material S0302A. SEM characterization was carried out with a Zeiss EVO MA15 instrument using beam conditions of 20 kV and 3 – 4 nA. Sulfur isotope ratios ($^{34}\text{S}/^{32}\text{S}$) were determined in pyrite using the IMS-1280 multi-collector ion microprobe at the CCIM. Primary beam conditions included the use of 20 keV $^{133}\text{Cs}^+$ ions focused to form a probe with diameter $\sim 10\ \mu\text{m}$ and beam current of 1.3 - 2.7 nA. The primary beam was rastered across an $18 \times 18\ \mu\text{m}$ area for 30 s prior to analysis, to clean the surface of Au and contaminants, and implant Cs. The analytical protocol interspersed analyses of unknowns with the pyrite reference material in a 4:1 ratio, with the pyrite reference material used to correct for instrumental mass fractionation ($\sim 4 - 6\ \text{‰}$ for $^{34}\text{S}/^{32}\text{S}$). The standard deviation of $^{34}\text{S}/^{32}\text{S}$ ratios for S0302A was 0.02 – 0.05 ‰ after small corrections for within-session IMF drift ($< 0.4\ \text{‰}$). Final uncertainties are reported at 95% confidence level (2σ) and include propagated within-spot counting errors, between-spot errors to account for geometric effects (blanket uncertainty of $\pm 0.10\ \text{‰}$ applied), and between-session error ($\leq \pm 0.02\ \text{‰}$) that accounts for uncertainty in the mean IMF for the session. The total uncertainties average $\pm 0.12 - 0.14\ \text{‰}$ (2σ) per spot, not including the absolute uncertainty in the true composition of S0302A pyrite. The $^{34}\text{S}/^{32}\text{S}$ value of VCDT utilized for normalization was 0.0441626 (Ding et al., 2001).

LA- ICPMS analysis

LA-ICPMS analysis was carried out at the CODES LA-ICPMS facility, University of Tasmania, using an Agilent 7500 ICPMS coupled to a Resolution S155 laser ablation cell and an ATL 193-nm excimer ArF laser using methods similar to that described in Large et al. (2009) and Danyushevsky et al. (2011). The focus of the LA-ICPMS mapping scheme was to determine the distribution of Re within pyrite at the sub-millimetre scale, whilst maintaining detection limits at the ppb level. To accomplish this goal, dwell times were biased towards Re (100 ms) compared to the other 21 isotopic masses analyzed (8 ms). Compositional maps were produced by rastering across the sample at a rate equal to the spot size (e.g. $10\ \mu\text{m}$ spot size = $10\ \mu\text{m/s}$ scan rate) using a laser frequency of 10 Hz and a fluence of 2.7 - 3.5 J/cm². Preceding and following each map one to three spot analyses of several external standards (STDGL2b2, BCR-2G, and GSD-1G) were measured for quantification. Following the analyses of the standards, but prior to the analysis of the sample, a spot analysis of quartz was used to clean the system and provide estimates of the Re blank during ablation of a mineral. In-house data reduction software packages were used to quantify the collected data. These calculations were similar to that done in a number of publications from the University of Tasmania (e.g. Steadman et al., 2015; Sykora et al., 2018)

The focus of this study was to map Re distributions, but many other elements were mapped to further characterize the sample. The major phases in these rocks include pyrite \pm sphalerite \pm galena \pm calcite \pm dolomite; therefore, the distribution of the major phases could be mapped quite effectively using Fe, Zn, Pb, S, Ca, Mg, and Mn. Common trace elements associated with sulfide mineralization, including Ni, Co, Cu, Ag, Sb, and As, were also mapped to resolve chemical zonation within sulfide phases. Elements that could be associated with the host rock or alteration phases included Si, Al, and K. Molybdenum was also selected for analysis due to its known association with Re (e.g. in molybdenite).

Results

Characterization of mineral separates

Semi-quantitative estimates of modal abundances and associated magnetic susceptibility for each mineral separate, prior to leaching, are provided in Table 1. Representative petrographic and BSE images can be found in Figure 7, and bulk minor and trace compositions for mineral separates are provided in Figure A2 and Table A1.

The Lisheen Main Zone sample 8S08FW, which was split into two pieces (8S08FW and 8S08FW-B), is dominated by pyrite, but there are slight differences in mineralogy between the most magnetic (8S08FW M1.0, 8S08FW-B M0.8) and least magnetic (8S08FW NM1.5) separates. Pyrite with minimal fracturing is the dominant phase in 8S08FW NM1.5 (Fig. 7A) with an estimated modal abundance of ~94%. The main impurities are small inclusions within the pyrite and are dominated by carbonates (~2%) and silicates (~3%). In 8S08FW-B M0.8 the pyrite is much more fractured and is complexly intergrown with other minerals such as galena and sphalerite (Fig. 7B). Pyrite is still the dominant phase (~83%) but this mineral separate has a greater abundance of sphalerite (~5%) and carbonate (~9%) compared to 8S08FW NM1.5. Carbonate was removed via HCl dissolution from 8S08FW NM1.5.

For the Lisheen Derryville Zone sample LK 359, two rock fragments split from the original piece of drillcore were analyzed (LK 359A and LK 359B). The Lisheen Derryville samples are complex, with very different mineralogical profiles between rock fragments LK 359A and LK 359B, even though they came from the same piece of core. In LK 359A, iron sulfides are enriched in the more magnetic end-members (~47% for LK 359A NM0.8) but are much less abundant in the least magnetic separate (~9% for LK 359A NM1.8). Sphalerite is an important phase in all mineral separates, making up ~69% in LK 359A NM1.8 and ~47% for LK 359A NM0.8. Galena is strongly enriched in the least magnetic separate (~19%) but is probably only present at < 1% in all other separates. In LK 359B, iron sulfide is probably the dominant

phase in all mineral separates except for the least magnetic separate (LK 359B NM1.8) in which sphalerite is abundant (~94%). Sphalerite is also an important component of all other separates (> 10%) where it is complexly intergrown with iron sulfide (Figs. 7C, D). Silicates and carbonates make up a minor proportion of both sub-samples (< 10%) and are present in greater abundance in separates with higher magnetic susceptibility. Leaching of some mineral separates (LK 359A NM0.8, LK 359A M1.2, LK 359B NM 1.4, LK 359B NM 1.6) using 6N and 10N HCl was expected to remove any residual carbonates, whereas galena and sphalerite would undergo partial to full dissolution in a trend similar to the experimental data shown in Figure A1.

Mineral separates from Hawker Creek are dominated by pyrite (> 90%) with minor amounts of sphalerite and carbonates. As shown in Figures 7E and 7F, the major difference between the most magnetic and least magnetic end-members are the density of fractures in pyrite, with the former containing much higher fracture densities. Highly fractured areas are common (Fig. 6C), whereas the unfractured, non-magnetic pyrites, probably come from regions such as the one shown in Figure 6D.

Re-Os results

A compilation of all the Re-Os results obtained from this study and the relevant data from Hnatyshin et al. (2015) and Hnatyshin et al. (2016) is provided in Tables 2-4. The isochron produced for 8S08FW (346.6 ± 3.0 , MSWD = 1.6, variation in initial osmium (VIOs) = 0.026) from Hnatyshin et al. (2015) is replicated in Figure 8 with additional detail indicating the position of leached mineral separates. To complement the Re-Os data from 8S08FW and 03-HC-8D, 21 analyses, including both leached and non-leached mineral separates, on the Lisheen Derryville sample LK 359 were produced.

Twelve analyses from LK 359A have a range of Re and Os concentrations of 338 - 6259 ppb and 1285 - 23597 ppt, respectively. Nine analyses for LK 359B have much lower concentrations of 40 - 506 ppb and 204 - 2724 ppt, for Re and Os, respectively. Using all analyses yields a model 3 age of 322 ± 11 Ma (MSWD = 206, n = 21) with an initial $^{187}\text{Os}/^{188}\text{Os}$ ratio of 0.9 ± 1.4 and a VIOs of 3.0 (Fig. 9A). Removing mineral separates that have the highest abundance of impurities results in a model 3 regression of 339 ± 13 Ma (MSWD = 94, n = 7) with an initial $^{187}\text{Os}/^{188}\text{Os}$ ratio of 0.3 ± 1.5 , and a VIOs of 1.6 (Fig. 9B).

Leaching experiments – effect on Re-Os isochrons

Lisheen Main Zone sample 8S08FW NM1.5, for which the mineral separate is of high purity (94% pyrite; Table 1), underwent leaching experiments to determine whether if preferential leaching of Re or

Os from pyrite took place. Separates leached with 6N (at ~21°C) and 10N HCl (at ~80°C) do not deviate from the 347 Ma isochron (Fig. 8) produced by Hnatyshin et al. (2015), suggesting that any preferential leaching of Re or Os is negligible. Therefore, HCl leaching of pyrite, even using conditions as strong as 10N HCl at elevated temperatures, does not appear to negatively impact the ability to produce a pyrite Re-Os isochron and so removing carbonate impurities appears to be safe to attempt. However, the acid solution began to turn yellow when 6N HCl was used suggesting that a mild reaction with the pyrite occurred even if a negligible (< 1 %) amount of pyrite was dissolved (Fig. A1). Therefore, we consider it preferable to prepare the mineral separates to a size of > 74 µm and then use low concentration HCl (i.e. 0.2N) to dissolve carbonate crystals out of the mineral separate. Finer grained material has not been rigorously tested, but the higher surface area per unit volume should be associated with a higher risk of Re and/or Os loss. Similarly, other minerals, such as sphalerite, have not been rigorously tested for preferential leaching of Re or Os.

SIMS sulfur isotope study

The Lisheen sample set used for SIMS pyrite sulfur isotopic analysis comprises several rock fragments and mineral separates that are identical to those used for Re-Os geochronology. Mineral separates were chosen based on their spread in Re-Os ratios and rock fragments were analyzed to reveal microscopic variations in sulfur isotope ratios. Prior to SIMS analysis, SEM images were taken to determine areas of interest and to avoid inclusions during SIMS analysis. Areas were typically chosen to help reveal any variability in sulfur isotope compositions in the rock; therefore, the distributions produced will have a strong bias towards outlier data and are unlikely to represent the true distribution of sulfur isotopic ratios in the rock as a whole. A summary of the measured $\delta^{34}\text{S}$ values is presented in Figures 10-11, with the full analytical data being provided in the Appendix (Tables A2, A3).

Lisheen

Four different separates from the Main Zone (8S08FW M0.8 and 8S08FW NM1.5) and the Derryville Zone (LK 359A NM0.8 and LK 359B NM1.6) were chosen for analysis. A single Main Zone rock fragment (8S08FW-1) and two Derryville rock fragments (LK 359-1, LK 359-2) were also analyzed (Fig. A3).

Rock fragment 8S08FW-1 is dominated by massive pyrite (LG1) containing numerous small sphalerite and galena inclusions (< 10 µm). Calcite veins cross-cut the sample (LG7?). Two anomalous areas are evident in this sample: a larger (200 µm) anhedral galena crystal (LG5) that appears to have

replaced pyrite can be seen on the left side of the image, and a heavily fractured area on the right-hand side. For 8S08FW, five transects were analyzed (Fig. 11). Pyrites associated with, or adjacent to LG1, LG5, LG6, and LG7, were measured with the intention to analyze areas that may contain the highest variability in sulfur isotopic composition. The mineral separate 8S08FW NM1.5 contains primarily clean LG1 pyrite, whereas the more magnetic separate 8S08FW M0.8 contains a higher abundance of inclusions and fractures. The $\delta^{34}\text{S}$ in 8S08FW-1 show a bimodal distribution, with peaks at approximately -40.0 ‰ and -20.0 ‰, but encompass the full range of $\delta^{34}\text{S}$ values between bacteriogenic sulfur (down to -45.2 ‰) and hydrothermal sulfur (up to +8.2 ‰) (Fig. 10).

Rock fragments LK 359-1 and LK 359-2 contain pyrite and marcasite (LG1, LG2, LG3) that is replaced, fractured, and pervasively infiltrated by sphalerite and carbonate (LG5, LG6). SIMS analysis focused on producing transects that started from the edge of the marcasite masses through to their cores (Figs. 11 E-G). As a result, all visually distinctive sections of LK 359 had their iron sulfide sulfur isotopic composition examined. Marcasite crystals from LK 359A-NM0.8 are replaced and crosscut by sphalerite (LG6), whereas LK 359B-NM1.6 is dominated by marcasite that is heavily fractured. Sample LK 359 displays a mean $\delta^{34}\text{S}$ of -37.15 ± 13.70 ‰, and a mode that lies between -47.5 to and -50 ‰ ($n = 101$). Sample LK 359A NM0.8 shows a broader span in $\delta^{34}\text{S}$, with a mean of -29.52 ± 16.23 ‰ ($n = 24$), whereas a more restricted $\delta^{34}\text{S}$ range is present in LK 359B NM1.6 (-42.96 ± 9.01 ‰, $n = 26$).

Laser ablation results

To improve confidence in the Re concentrations produced by LA-ICPMS at low ppb levels, we compared these results with those produced through TIMS analysis. Sample 8S08FW, being comparatively paragenetically simple and homogeneous provided the best opportunity for comparison as it probably provides the best scalability between element maps and TIMS analysis. From Table 2, bulk sulfide material (8S08FW) has a Re concentration of 3.70 ppb, and the minimum concentration from an unleached separate is 2.52 ppb (8S08FWB NM1.2). Map 1 and Map 2 from 8S08FW-1 (Fig. 12), which have the lowest detection limits, contain mean Re concentrations of 1.3 ppb. There is some concern in the precision of LA-ICPMS analyses at low concentrations, close to the detection limit, because the data becomes discontinuous. However, we cautiously suggest that the accuracy of LA-ICPMS measurements may be within a factor of 2-3 of the true concentration at these low levels, and comparisons made at the order of magnitude level are probably robust.

Maps of Re, Mo, Co, As, K, and Ca for each sample are shown in Figures 12-14 and the full dataset available in Tables A4-A12. It should be emphasized that comparisons between phases should be done cautiously because the data reduction was optimized for pyrite analysis.

For sample 8S08FW, the Re abundance varies between <1 to 78 ppb (Fig. 12). However, the bulk Re budget of this sample is controlled by pyrite containing 1-5 ppb Re, similar to the results of the TIMS dataset (Table 2), resulting in a relatively homogeneous Re profile. Rare, higher abundance Re excursions of > 10 ppb are present in highly fractured areas (e.g. Figure 12 Map 2). These are associated with enrichments of K, Mo, and Co, and depletion of As. In the higher-resolution images (Figure 12, Maps 3-4), Mo, Co and As show more complex patterns, with higher concentrations possibly following fractures.

Re abundances in LK 359 vary by over three orders of magnitude, from a low of < 10 ppb in the cores of LG2 iron sulfide (e.g. top of Map 2 in Figure 13) to levels exceeding 10 ppm in localized LG6 areas (Fig. 15), with the bulk Re budget being dominated by phases containing > 100 ppb Re. Iron sulfide within a few hundred micrometers of either LG6 sphalerite or illite show enrichments of up to several hundred ppb Re (Fig. 13). Similar patterns of enrichment of several orders of magnitude are evident for Mo, As, Co, and K (Fig. 13).

The Hawker Creek sample shows a clear bimodal distribution of trace elements (Fig. 14). The pyrite cores typically have very low abundances of Re (< 3 ppb), Mo (< 0.03 ppm), Co (< 0.03 ppm), As (< 1 ppm), and K (< 3 ppm), are, in general, below the detection limits of LA-ICPMS analysis. Based on the results of TIMS analysis on bulk mineral separates, Re concentrations in these cores are expected to be 0.1-0.5 ppb. In the fractures in these pyrites there are significant enrichments of Re (up to 511 ppb), Mo (up 19 ppm), Co (up to 9 ppm) and As (up to 35 ppm). The high K (up to 3400 ppm) in this sample is probably hosted in small inclusions of silicates.

Discussion

Rhenium spatial distribution within sulfide ore

Ideally, pyrite Re-Os geochronology should use only unaltered pyrite from a single paragenetic stage of mineralization, but for the samples used here, images of mineral separates (Fig. 7) and compositional maps (Figs. 12-14) show this is not the case. Fortunately, both 8S08FW and 03-HC-8D are dominated volumetrically by primary pyrite, which, when extracted, can produce meaningful ages. In

both of these samples, primary pyrite has low Re abundances (< 10 ppb), potentially exacerbating any effects caused by incorporation of impurities. Based on this observation, LK 359 may contain relatively pristine material in the cores of iron sulfide masses based on their Re abundance (< 10 ppb; Fig. 13) and $\delta^{34}\text{S}$ values (< -40 ‰; Figs. 10, 11), similar to pristine pyrite in 8S08FW.

In samples LK 359 and 03-HC-8D the Re budget is dominated by impurities and alteration products. In LK 359 much of the iron sulfide has been altered, as indicated by enrichment of trace elements along crystal rims (Fig. 13), or higher values of $\delta^{34}\text{S}$ ($\delta^{34}\text{S} > -40$; Figs. 11F, G). Altered areas contain several hundred ppb Re, which commonly correlates with elements associated with silicate minerals (e.g. K, Si, Al). Localized enrichments of other trace elements (e.g. Ni, Co, Mo, As) is also common. This is demonstrated in LK 359 where LG2 marcasite in proximity to LG6 has high trace element concentrations (Figs. 4 and 13). Similarly, 03-HC-8D also shows trace element enrichment in post-mineralization fractures. Whenever alteration or impurities are identified there is a risk that open-system behavior or mixing may have occurred, resulting in the isotopic composition of the sample being modified in an unpredictable fashion.

Another significant characteristic of LK 359 is localized regions (< 100 μm^2) containing very high levels of Re (> 1 ppm), correlated with very high concentrations of Mo (> 1000 ppm) (Fig. 15). Micron-scale molybdenite crystals are the mostly probable explanation for this observation. Molybdenite crystals are expected to have a negligible common Os signature and their presence can elevate the $^{187}\text{Re}/^{188}\text{Os}$ and $^{187}\text{Os}/^{188}\text{Os}$ in the mineral separates. The observation of micron-scale molybdenite suggests that molybdenite inclusions may be a widespread issue associated with pyrite Re-Os geochronology. Many examples of pyrite, chalcopyrite, and arsenopyrite having extremely radiogenic Os and with high Re/Os are known (e.g. Barra et al., 2003; Zhang et al., 2005; Morelli et al., 2007; Selby et al., 2009; Lawley et al., 2013), and it is plausible that the Re-Os age information in these studies is carried by molybdenite inclusions, rather than by pyrite.

A spatial association between Re and Mo, and, to a lesser degree, other elements (e.g. K, Co, As) is evident (Figs 12-14). This relationship is supported through more detailed spatial analysis of Map 1 from LK 359 (Fig. 13), a sample chosen for the continuous nature of its dataset. Correlograms were produced in both pyrite and sphalerite-rich areas to determine how different elements predict the concentration of Re up to a range of 200 μm (Fig. 16). Molybdenum shows the strongest correlation with Re for both pyrite and sphalerite, whereas all other elements have modest (e.g. Co), or insignificant (e.g. As), correlations (Fig. 16A). Curiously, K is a reasonable predictor of Re distribution in sphalerite and

probably is a result of the intimate spatial association between illite and sphalerite (LG6). A series of scatter plots shows the relationship Re has with other elements (Fig. 17; Mo, As, Co, and K) for each pixel in the LA-ICPMS maps created in this study as well as additional unpublished map data from Lisheen and Nanisivik. Molybdenum shows the best correlation with Re, corroborating the results of visual inspection and spatial analysis. Other elements (e.g. Co, As, K) that in Figures 12-14 suggest positive correlations at local scales do not have a well-correlated nature at a bulk scale (Fig. 17). Mo/Re ratios do not vary much from ~1000 and are almost independent of Re concentration, but all other elements show a much wider variability and higher dependence on the Re concentration. A unique characteristic of the Mo-Re ratio is that it is insensitive to ore locality (excluding Hawker Creek, which is discussed below), resulting in overlapping patterns, even though each sample is composed of a different mineral assemblage. This behavior implies that Re substituted exclusively into Mo-rich minerals (e.g. molybdenite) or in a similar fashion to Mo, which in some cases adsorbs on pyrite surfaces as Fe-Mo-S cuboidal clusters (Vorlicek et al., 2004; Helz et al., 2014), as opposed to following lattice-bound elements such as Ni, Co, or As.

The apparent association between silicates and Re in LK 359 and 03-HC-8D is enigmatic due to the relatively low resolution of LA-ICPMS analysis. We speculate that Re is still hosted in sulfides since there is scant evidence to suggest otherwise (e.g. peculiar correlations). The only sample that appears to show unusual Re behavior is Hawker Creek. Examination of the Hawker Creek data-points with enriched Re contents (>10 ppb), reveals a Mo-Re ratio that is much lower than those from all other locations (Fig. 17). The reason for this is unclear, but it may be a consequence of Re being hosted in a different phase (e.g. clays), being incorporated into minerals in a different fashion than the other samples, or being carried by a fundamentally different fluid.

Based on the strong Re-Mo correlation documented here, the use of Mo as a Re proxy when Re analyses are unable to be made due to technical or fiscal limitations is suggested. Identifying high-risk areas of samples (e.g. alteration associated with silicates) is also useful in evaluating the potential of a rock for Re-Os geochronology.

Variability in sulfur isotope signatures potentially can be used to fingerprint fluid sources and constrain ore-forming processes. Figures 10-11 show a non-random distribution of sulfur isotopic compositions in these rocks that are clearly correlated with specific textures (Fig. 11), but not necessarily with pyrite composition (Figure A5). The absolute range in sulfur isotopes is not useful in determining if a sample will produce a highly precise isochron. For example, 8S08FW's variation in $\delta^{34}\text{S}$

exceeds 40 ‰ but produced a precise isochron (MSWD = 1.6), whereas the Nanisivik material from Hnatyshin et al. (2016) produced an isochron with far greater scatter (MSWD = 97) with only ~ 5 ‰ variation. The utility of sulfur isotopes therefore lies in their ability to test for possible sources of mineralizing fluids and identify paragenetically distinct areas within a sample that can then be scrutinized using other methods (e.g. LA-ICPMS).

Assessment of Lisheen Re-Os geochronology

Alteration and Impurities

8S08FW

Sample 8S08FW is dominated by massive LG1 pyrite that is characterized by few fractures and $\delta^{34}\text{S}$ values of < -35 ‰. Local alteration of LG1 pyrite associated with LG5 galena, LG6 fractures is suggested by anomalous sulfur isotope (> -35 ‰) and/or trace element patterns in the vicinity of these phases (Figs. 11A-C). Veins of LG5 galena are rare but appear to have 100 – 200 μm halos within which the sulfur isotope signature of LG1 pyrite has been shifted to higher $\delta^{34}\text{S}$ values (~ -20 ‰; Figs. 11A-C). Calcite veins of LG7 are much more common and are locally associated with trace element enrichment (e.g. Fig. 12, Map 2), but do not show anomalous $\delta^{34}\text{S}$. Changes to the original LG1 pyrite Re distribution appears minor, because Re concentrations near LG5 or LG7 veins are unchanged. Pyrite adjacent to LG6 fractures (e.g. Figs. 12, Map 2) is enriched in trace elements, including Re, and exhibits the highest $\delta^{34}\text{S}$ in 8S08FW, with values up to +8.2 ‰, and may represent conduits of hydrothermal fluid (Figs. 11B, C).

The spatial data, as well as bulk chemical analysis, reveal that the mineral separates with lower magnetic susceptibility are correlated with lower trace element concentrations (Fig. A2), a lower density of fractures (Fig. 7), and fewer carbonates (Table 1). This implies that they contain a higher proportion of primary pyrite than the more magnetic samples, and contain fewer impurities (e.g. sphalerite, and calcite). There is no relationship linking the distribution of data points along the isochron and the amount of impurities or alteration contained in the sample. This suggests that alteration associated with LG5, LG6, and LG7, as well as the calcite and sphalerite impurities themselves, had a negligible effect on the 8S08FW pyrite Re-Os isochron.

LK 359

Sample LK 359 contains illite associated with trace element enrichment and overprinted LG1-LG3 pyrite and marcasite. The fractured areas within LG1-LG3 iron sulfides show high variability in sulfur

isotope compositions that are not possible to link to textural relationships (Figs. 11E, F). Unfractured areas containing low $\delta^{34}\text{S}$ ($< -40\text{‰}$) signatures are plausible locations where early pyrite may have been preserved (Figs. 11F, G). Extrapolating these relationships to the LA-ICPMS images (Fig. 13) it appears that the core regions of the iron sulfide masses generally contain fewer fractures, inclusions and display lower trace element concentrations. These regions also appear to have the lowest Re contents (< 10 ppb). During the precipitation of LG6 sphalerite/illite, the associated hydrothermal fluids appear to have altered the earlier iron sulfides resulting in enriched trace element profiles, including Re, and elevated $\delta^{34}\text{S}$ values ($> -40\text{‰}$). The rhenium budget is dominated by putative molybdenite crystals (Figs. 16), LG6 sphalerite/illite mixtures.

Based on the calculated modal mineralogy (Table 1) for the prepared separates, it appears that most of the silicates (e.g. illite) have been removed. However, the high concentration of Re associated with these phases means that they can still significantly influence the measured Re-Os isotopic ratios. Furthermore, because these silicates, and likely the embedded molybdenite crystals, are from a distinctly different event than the primary pyrite cores (LG2), the mixing lines they create may negatively affect the validity of the Re-Os results. For LK 359A, the much higher Re contents are probably a consequence of this sample containing more LG6 sphalerite/illite. This relationship is consistent with the higher (i.e. more hydrothermal input) and more variable $\delta^{34}\text{S}$ measured for LK 359A NM1.6 ($-29.52 \pm 16.23\text{‰}$) compared to LK 359B NM1.6 ($-42.96 \pm 9.02\text{‰}$). No mineral separate contains pure unaltered pyrite; all contain appreciable sphalerite and a minor amount of silicates.

Validity of Model 3 Regressions

One important criterion when using the isochron method for dating rocks is that the initial isotope ratio of the daughter element is invariant (i.e. VIOs = 0) for the sample set used (Model 1) or can be modelled in a predictable fashion (e.g. Model 3, Figure A4). The limits of what constitutes reasonable variability in initial $^{187}\text{Os}/^{188}\text{Os}$, and in turn the VIOs required by Model 3 isochrons, is poorly constrained. In environments in which fluid mixing was possible, such as in the Irish system (Wilkinson 2010; Wilkinson et al. 2014), significant differences in $^{187}\text{Os}/^{188}\text{Os}$ could occur in both time and space. Modern ocean-floor hydrothermal systems mixing with seawater are known to produce a continuum of $^{187}\text{Os}/^{188}\text{Os}$ values between mantle (~ 0.125) and seawater Os (~ 1.06); therefore, VIOs of up to ~ 0.9 could be considered a liberal bound on possible VIOs, at least until better constraints can be determined (Sharma et al., 2000, 2007). Variation in $^{187}\text{Os}/^{188}\text{Os}$ during mineralization, may be identified when

comparing the calculated initial ratio for an individual mineral separate to the its paragenetic character (e.g. later generations may have a different initial ratio than younger generations).

For sample 8S08FW, the calculated initial $^{187}\text{Os}/^{188}\text{Os}$ for individual mineral separates, assuming an age of 347 Ma, range from 0.21 to 0.30, and is not greatly different than the VIOs required for the Model 3 isochron (0.026). This small variation is considered negligible, considering that analytical uncertainty could account for much of this variation, and therefore we consider the use of a Model 3 regression appropriate for 8S08FW. The narrow range VIOs suggest that the Os source is dominated by one end-member fluid in the Lisheen system, and has not been negatively influenced by the mixing processes thought to produce ore at Lisheen. This contrasts with sample LK 359, which shows substantial variation (range > 1) in initial ratios (Table 3) and similarly high VIOs of 3.0 and 1.6 (assuming an age of 347 Ma) for the isochrons in Figure 9A and 9B, respectively. No clear trend is evident between initial $^{187}\text{Os}/^{188}\text{Os}$ and the magnetic susceptibility of a sample, suggesting that variability is not strongly controlled by the relative proportions of major phases. Furthermore, many of the calculated initial ratios for an age of 347 Ma are impossibly low, below that of a mantle value of 0.13 (Meisel et al., 2001). Therefore, in contrast to 8S08FW, a Model 3 regression is inappropriate for LK 359, and would provide an inaccurate result for the age of ore at Derryville.

Interpretation of Lisheen Re-Os geochronology

The Main Zone sample 8S08FW gives the most precise estimate for the age of Lisheen mineralization (Fig. 8, 346.6 ± 3.0 Ma). Closer inspection of the original dataset from Hnatyshin et al. (2015) identifies several important aspects that made 8S08FW a successful candidate for pyrite Re-Os geochronology. The homogeneity in the Re maps for 8S08FW, coupled with the observation that alteration is localized and did not significantly modify the Re concentration (i.e. by orders of magnitude) gives confidence that 8S08FW retains age information from ore mineralization. Additionally, all isochron assumptions (e.g. reasonably low VIOs) have been, in our opinion, passed to a reasonable degree, with the majority, if not all, observed scatter being related to the analytical errors. We conclude that the interpretations, and age produced, from Hnatyshin et al. (2015) are upheld for Lisheen based on our detailed analysis of 8S08FW.

The calculated Model 3 age for LK 359 (322 ± 11 Ma: Fig. 9A) is significantly younger than 8S08FW (346.6 ± 3.0 Ma) and there are many issues with the dataset which makes the LK 359 age suspect. There are clear differences in Re-Os systematics (Table 3) between LK 359A and LK 359B, with higher scatter (LK 359A) being correlated with a higher proportion of LG6 (sphalerite in Table 1). It

appears that incorporation of LG6 has made the calculated initial Os ratio impossibly low (assuming a 347 Ma age) for the majority of samples, and excessively variable. By focusing on the samples with the fewest impurities (LK 359B NM1.6, samples leached in 10N HCl; Fig 9B), and assuming an initial $^{187}\text{Os}/^{188}\text{Os}$ of 0.25, the mean model age, which is 340 ± 8 Ma, is in much better agreement with the “expected” age of ~ 347 Ma. Even within these separates, impurities and altered pyrite are still present, so it is suggested that this estimate may be a lower bound on the age. Together with the age of the host rock (~ 353 Ma; Waters, 2011) the best estimate we can give for the age of LK 359 is 332 – 353 Ma. However, this estimate requires a lot of assumptions and is not as robust as the age determined for 8S08FW. It is important to emphasize that the Model 3 isochron (322 ± 11 Ma) created from the dataset, although fairly precise for Re-Os pyrite geochronology, with an uncertainty of $\pm 3\%$, is probably inaccurate.

The youngest age implied by individual model ages is ~ 309 Ma (assuming an initial ratio of 0.25), a time during which Ireland was beginning to experience heating and tectonic activity associated with the Variscan orogeny (Quinn et al., 2005). During this time the Irish Midlands underwent extensive reverse faulting and folding (Woodcock and Strachan, 2000; Graham, 2001), and older normal faults were reactivated (Chadwick et al., 1993). Reverse faulting in the Lisheen area resulted in the deformation of the Lisheen ore (Fusciardi et al., 2003; Carboni et al., 2003). Variscan burial and deformation are thought to be responsible for the remagnetization of magnetic grains found at Lisheen and other Irish deposits (Wilkinson et al., 2017), resulting in the Variscan paleomagnetic ages observed (Symons et al., 2007; Pannalal et al. 2008a, 2008b). Therefore, it could be speculated that fluids may have migrated into the Lisheen deposit during the Variscan orogeny in response to heating and/or tectonic activity, potentially altering/remobilizing preexisting material, and producing the young model ages observed in LK 359.

Hawker Creek Re-Os geochronology

The Hawker Creek pyrite Re-Os dataset did not produce a well-defined regression (Hnatyshin et al., 2016). However, some constraints can be placed on the Re-Os systematics of the mineralization using key observations on the dated material. Older model ages are correlated with lower magnetic susceptibility, lower Re abundances, homogeneous sulfur isotope patterns, and a lower density of fractures in the analyzed pyrite separates (Figs. 7E, F). Younger ages are correlated with the opposite characteristics. It was previously argued that the samples contain two end members, an older generation of pyrite at ~ 1.1 Ga and a younger generation at ~ 400 Ma. The LA-ICPMS mapping

undertaken here clearly identifies these two predicted end member domains within the 03-HC-8D pyrite (Fig. 14). The fractures in 03-HC-8D do contain the bulk of the Re, and other trace elements, with Re concentrations ranging up to several hundred ppb. However, the exact phase that the Re is hosted in is unclear because of the limited spatial resolution of the mapping. The pyrite crystals appear to have very low trace element concentrations, with Re < 1 ppb. As suggested by Hnatyshin et al. (2016), mineral separates with the lowest magnetic susceptibility, which contain the lowest density of fractures, represent the best estimate of the age of the ore (i.e. 1083 Ma from sample 03-HC-8F NM1.2; Hnatyshin et al., 2016). Pyrite enveloped within trace element-rich fractures (e.g. 03-HC-8D M0.8) has the youngest model age at 413 Ma. This, combined with an Ar-Ar age of 461 Ma from adularia alteration at Nanisivik (Sherlock et al. 2004), suggests that the Borden basin experienced fluid flow in the Paleozoic. There is sparse evidence of major fluid flow at that time, but it has been speculated that evaporite deposition to the northwest may have initiated deep-crustal brine convection during this time (Turner, 2011; Hnatyshin et al., 2016).

Evaluation of magnetic separation, and effects on Re-Os isochrons

The effect that magnetic separation has on the mineralogy of a mineral separate is complex and sample specific (Table 1). Pyrite (and sphalerite) have a wide range of magnetic susceptibilities and may (e.g. pyrite in 8S08FW NM1.5) or may not become highly concentrated in a specific separate (e.g. iron sulfide in LK 359). This complex behavior necessitates follow up imaging, such as that shown in Figure 7, when mineral processing is undertaken. Magnetic separation can have a significant effect on the quality of age beyond simply removing impurities. For example, for sample 8S08FW, the two mineral separates that did not undergo magnetic separation had a very restricted range of Re-Os ratios (919 - 953) but this range expanded to 556 - 1502 when accounting for variation in magnetic susceptibility (Table 2, Fig. 8). The large range in Re/Os ratio is in part responsible for the highly precise age of this sample. Furthermore, the Hawker Creek dataset is an extremely important example in showing the potential application of magnetic separation on the retrieval of Re-Os age information from pyrite. The Hawker Creek mineral separates show extreme physical differences (Fig. 7), which allow them to be correlated with compositional imaging (Fig. 14), and different ages, as was discussed above. The Hawker Creek dataset shows that it is possible in some circumstances to distinguish different generations of pyrite through differences in magnetic susceptibility. The differences in magnetic susceptibility in the Hawker Creek material probably resulted from precipitation of magnetic minerals during alteration.

One trend evident in the magnetic susceptibility data is a positive correlation between relative magnetic susceptibility and the bulk concentration of Re in prepared mineral separates (Tables 2-4, Fig. A6). In most of the published datasets for which this information is available, a similar correlation between magnetic susceptibility and Re concentrations exists, (e.g. van Acken et al., 2014; Hnatyshin et al., 2015; Hnatyshin et al., 2016). This relationship could be used to select pyrite with higher Re concentrations in future studies, would be useful for reducing the amount of blank correction or to reduce the mass of sample required for analysis, and to remove altered mineral separates (e.g. Hawker Creek). Until a dedicated study is undertaken, perhaps one that integrates LA-ICPMS and scanning SQUID microscopy (Fong et al. 2005), the cause of the documented Re vs. χ correlation remains enigmatic.

Conclusions

Pyrite from Lisheen sample 8S08FW has a relatively homogeneous Re distribution, with the Re budget dominated by pyrite containing 1-5 ppb Re, and corresponds to a high-quality Re-Os isochron (346.6 ± 3.0 Ma, MSWD = 1.6). In LK 359 (Lisheen) relatively pristine iron sulfide cores, assumed to represent mineralization at ~ 347 Ma, contain < 10 ppb, are mixed with altered sulfides (> 100 ppb Re) and secondary molybdenite crystals (> 1 ppm Re), hypothesized to be from Variscan remobilization at ~ 309 Ma based on model age constraints. For 03-HC-8D (Hawker Creek), pyrite contains very low Re abundances (< 1 ppb) that represent mineralization at ~ 1100 Ma. Alteration and fracture fill material contain Re abundances > 100 ppb and is associated with post-mineralization alteration at ~ 400 Ma. Without the availability of LA-ICPMS Re spatial data to identify complexities within these samples, the corresponding Re-Os results are easily misinterpreted resulting in possibly spurious ages.

The characterization of the samples used in this study demonstrates that commonly used mineral separation procedures (crushing, heavy liquid separation, magnetic separation) produce mineral separates of variable quality. The crushing procedure can produce composite grains with silicates and carbonates, which may still comprise $> 10\%$ of some mineral separates, even after heavy liquid separation. Removal of these impurities is required because low density minerals may be associated with non-isochronous behavior. Removal of carbonates is relatively straightforward, as applying mild leaching (e.g. 0.2N HCl) appears effective and does not influence the Re-Os systematics of pyrite. Magnetic separation may be vital in removing additional alteration/impurities, as shown in 03-HC-8D, and may expand the range of the Re-Os ratio in a dataset.

ACKNOWLEDGMENTS

This work was supported by a NSERC Discovery Grant to Dr. Robert A. Creaser. We would like to thank Ken Kocon from Statistics Canada for his useful discussion regarding the statistical methods used in this study.

References

Arne, D. C., Curtis, L. W., & Kissin, S. A. (1991). Internal zonation in a carbonate-hosted Zn-Pb-Ag deposit, Nanisivik, Baffin Island, Canada. *Economic Geology*, *86*(4), 699-717.

Barra, F., Ruiz, J., Mathur, R., & Titley, S. (2003). A Re-Os study of sulfide minerals from the Bagdad porphyry Cu-Mo deposit, northern Arizona, USA. *Mineralium Deposita*, *38*(5), 585-596.

Carboni, V., Walsh, J. J., Stewart, D. R. A., Güven, J. F., & Eliopoulos, D. G. (2003). Timing and geometry of normal faults and associated structures at the Lisheen Zn/Pb deposit, Ireland—investigating their role in the transport and the trapping of metals. In *Mineral Exploration and Sustainable Development: Proceedings of the 7th Biennial SGA Meeting* (pp. 665-668).

Chadwick, R. A., Evans, D. J., & Holliday, D. W. (1993). The Maryport fault: the post-Caledonian tectonic history of southern Britain in microcosm. *Journal of the Geological Society*, *150*(2), 247-250.

Christensen, J. N., Halliday, A. N., Kesler, S. E., & Sangster, D. F. (1993). Further evaluation of the Rb-Sr dating of sphalerite: the Nanisivik Precambrian MVT deposit, Baffin Island, Canada. In *Abstracts with Programs-Geological Society of America* (Vol. 25, p. 471).

Creaser, R. A., Wilkinson, J. J., & Hnatyshin, D. (2009). Re-Os dating of sulfide mineralization (pyrite) from the Lisheen Pb-Zn deposit, Ireland. In *2009 Portland GSA Annual Meeting*.

Danyushevsky, L. V., Robinson, P., Gilbert, S.E. (2011). Routine quantitative multi-element analysis of sulphide minerals by laser ablation ICP-MS: Standard development and consideration of matrix effects. *Geochemistry Exploration Environment Analysis*, 11(1), 51-60.

Ding, T., Valkiers, S., Kipphardt, H., De Bièvre, P., Taylor, P. D. P., Gonfiantini, R., & Krouse, R. (2001). Calibrated sulfur isotope abundance ratios of three IAEA sulfur isotope reference materials and V-CDT with a reassessment of the atomic weight of sulfur. *Geochimica et Cosmochimica Acta*, 65(15), 2433-2437.

Ding, C., Nie, F., Bagas, L., Dai, P., Jiang, S., Ding, C., ... & Shao, G. (2016). Pyrite Re–Os and zircon U–Pb dating of the Tugurige gold deposit in the western part of the Xing'an–Mongolia Orogenic Belt, China and its geological significance. *Ore Geology Reviews*, 72, 669-681.

Fong, L. E., Holzer, J. R., McBride, K. K., Lima, E. A., Baudenbacher, F., & Radparvar, M. (2005). High-resolution room-temperature sample scanning superconducting quantum interference device microscope configurable for geological and biomagnetic applications. *Review of Scientific Instruments*, 76(5), 053703.

Fusciardi, L. P., Guven, J. F., Stewart, D. R. A., Carboni, V., & Walshe, J. J. (2003). The geology and genesis of the Lisheen Zn-Pb deposit, Co. Tipperary, Ireland. *Europe's major base metal deposits: Dublin, Irish Association for Economic Geology*, 455-481.

Graham, J.R., 2001, Variscan structures, in Holland, C.H., ed., *The geology of Ireland:*

Edinburgh, Dunedin Academic Press, p. 312–330.

Helz, G. R., Erickson, B. E., & Vorlicek, T. P. (2014). Stabilities of thiomolybdate complexes of iron; implications for retention of essential trace elements (Fe, Cu, Mo) in sulfidic waters. *Metallomics*, 6(6), 1131-1140.

Hitzman, M.W., Redmond, P.B., and Beaty, D.W. (2002), The carbonate hosted Lisheen Zn-Pb-Ag deposit, County Tipperary, Ireland: *Economic Geology*, 97, 1627–1655.

Hnatyshin, D., Creaser, R. A., Wilkinson, J. J., & Gleeson, S. A. (2015). Re-Os dating of pyrite confirms an early diagenetic onset and extended duration of mineralization in the Irish Zn-Pb ore field. *Geology*, 43(2), 143-146.

Hnatyshin, D., Kontak, D. J., Turner, E. C., Creaser, R. A., Morden, R., & Stern, R. A. (2016). Geochronologic (Re Os) and fluid-chemical constraints on the formation of the Mesoproterozoic-hosted Nanisivik Zn Pb deposit, Nunavut, Canada: Evidence for early diagenetic, low-temperature conditions of formation. *Ore Geology Reviews*, 79, 189-217.

Jackson, G. D., & Iannelli, T. R. (1981). Rift-related cyclic sedimentation in the Neohelikian Borden Basin, northern Baffin Island. *Geological Survey of Canada, Paper*, 81-10.

Jiang, S. H., Bagas, L., & Liang, Q. L. (2017). Pyrite Re-Os isotope systematics at the Zijinshan deposit of SW Fujian, China: Constraints on the timing and source of Cu-Au mineralization. *Ore Geology Reviews*, 80, 612-622.

Large, R. R., Danyushevsky, L., Hollit, C., Maslennikov, V., Meffre, S., Gilbert, S., & Singh, B. (2009). Gold and trace element zonation in pyrite using a laser imaging technique: Implications for the timing of gold in orogenic and Carlin-style sediment-hosted deposits. *Economic Geology*, 104(5), 635-668.

Lawley, C. J. M., & Selby, D. (2012). Re-Os geochronology of quartz-enclosed ultrafine molybdenite: Implications for ore geochronology. *Economic Geology*, *107*(7), 1499-1505.

Lawley, C., Selby, D., & Imber, J. (2013). Re-Os molybdenite, pyrite, and chalcopyrite geochronology, Lupa goldfield, southwestern Tanzania: tracing metallogenic time scales at midcrustal shear zones hosting orogenic Au deposits. *Economic Geology*, *108*(7), 1591-1613.

Liu, Y., Yang, G., Chen, J., Du, A., & Xie, Z. (2004). Re-Os dating of pyrite from giant Bayan Obo REE-Nb-Fe deposit. *Chinese Science Bulletin*, *49*(24), 2627-2631.

Ludwig, K. R. (2003). Isoplot 3.00: A geochronological toolkit for Microsoft Excel, 71 pp. *Berkeley Geochronol. Center Spec. Publ*, *4.1*.

Mathur, R., Mutti, L., Barra, F., Gold, D., Smith, R. C., Doden, A., ... & McWilliams, A. (2008). Fluid inclusion and Re-Os isotopic evidence for hot, Cenozoic mineralization in the central Pennsylvanian Valley and Ridge Province. *Mineralogy and Petrology*, *93*(3-4), 309.

Meisel, T., Walker, R. J., Irving, A. J., & Lorand, J. P. (2001). Osmium isotopic compositions of mantle xenoliths: a global perspective. *Geochimica et Cosmochimica Acta*, *65*(8), 1311-1323.

Morelli, R. M., Creaser, R. A., Selby, D., Kelley, K. D., Leach, D. L., & King, A. R. (2004). Re-Os sulfide geochronology of the red dog sediment-hosted Zn-Pb-Ag deposit, Brooks Range, Alaska. *Economic Geology*, *99*(7), 1569-1576.

Morelli, R., Creaser, R. A., Seltmann, R., Stuart, F. M., Selby, D., & Graupner, T. (2007). Age and source constraints for the giant Muruntau gold deposit, Uzbekistan, from coupled Re-Os-He isotopes in arsenopyrite. *Geology*, 35(9), 795-798.

Morelli, R. M., Bell, C. C., Creaser, R. A., & Simonetti, A. (2010). Constraints on the genesis of gold mineralization at the Homestake Gold Deposit, Black Hills, South Dakota from rhenium–osmium sulfide geochronology. *Mineralium Deposita*, 45(5), 461-480.

Munhá, J., Relvas, J. M. R. S., Barriga, F. J. A. S., Conceição, P., Jorge, R. C. G. S., Mathur, R., ... & Tassinari, C. C. G. (2005). Osmium isotope systematics in the Iberian Pyrite Belt. In *Mineral deposit research: Meeting the global challenge* (pp. 663-666). Springer, Berlin, Heidelberg.

Olson, R. A. (1984). Genesis of paleokarst and strata-bound zinc-lead sulfide deposits in a Proterozoic dolostone, northern Baffin Island, Canada. *Economic Geology*, 79(5), 1056-1103.

Pannalal, S. J., Symons, D. T. A., & Sangster, D. F. (2008). Paleomagnetic evidence for an early Permian age of the Lisheen Zn-Pb deposit, Ireland. *Economic Geology*, 103(8), 1641-1655.

Pannalal, S. J., Symons, D. T. A., & Sangster, D. F. (2008). Palaeomagnetic evidence of a Variscan age for the epigenetic Galmoy zinc–lead deposit, Ireland. *Terra Nova*, 20(5), 385-393.

Quinn, D., Meere, P. A., & Wartho, J. A. (2005). A chronology of foreland deformation: Ultra-violet laser $^{40}\text{Ar}/^{39}\text{Ar}$ dating of syn/late-orogenic intrusions from the Variscides of southwest Ireland. *Journal of Structural Geology*, 27(8), 1413-1425.

Riegler, T., & McClenaghan, S. H. (2017). Authigenic potassic silicates in the Rathdowney Trend, southwest Ireland: New perspectives for ore genesis from petrography of gangue phases in Irish-type carbonate-hosted Zn-Pb deposits. *Ore Geology Reviews*, *88*, 140-155.

Selby, D., & Creaser, R. A. (2003). Re–Os geochronology of organic rich sediments: an evaluation of organic matter analysis methods. *Chemical Geology*, *200*(3), 225-240.

Selby, D., & Creaser, R. A. (2004). Macroscale NTIMS and microscale LA-MC-ICP-MS Re-Os isotopic analysis of molybdenite: Testing spatial restrictions for reliable Re-Os age determinations, and implications for the decoupling of Re and Os within molybdenite. *Geochimica et Cosmochimica Acta*, *68*(19), 3897-3908.

Selby, D., Kelley, K. D., Hitzman, M. W., & Zieg, J. (2009). Re-Os sulfide (bornite, chalcopyrite, and pyrite) systematics of the carbonate-hosted copper deposits at Ruby Creek, southern Brooks Range, Alaska. *Economic Geology*, *104*(3), 437-444.1.

Sharma, M., Wasserburg, G. J., Hofmann, A. W., & Butterfield, D. A. (2000). Osmium isotopes in hydrothermal fluids from the Juan de Fuca Ridge. *Earth and Planetary Science Letters*, *179*(1), 139-152.

Sharma, M., Rosenberg, E. J., & Butterfield, D. A. (2007). Search for the proverbial mantle osmium sources to the oceans: Hydrothermal alteration of mid-ocean ridge basalt. *Geochimica et Cosmochimica Acta*, *71*(19), 4655-4667.

Sherlock, R. L., Lee, J. K., & Cousens, B. L. (2004). Geologic and geochronologic constraints on the timing of mineralization at the Nanisivik zinc-lead Mississippi Valley-type deposit, northern Baffin Island, Nunavut, Canada. *Economic Geology*, *99*(2), 279-293.

Steadman, J. A., Large, R. R., Meffre, S., Olin, P. H., Danyushevsky, L. V., Gregory, D. D., ... & Holden, P. (2015). Synsedimentary to early diagenetic gold in black shale-hosted pyrite nodules at the Golden Mile Deposit, Kalgoorlie, Western Australia. *Economic Geology*, *110*(5), 1157-1191.

Stein, H. J., Morgan, J. W., & Scherstén, A. (2000). Re-Os dating of low-level highly radiogenic (LLHR) sulfides: The Harnas gold deposit, southwest Sweden, records continental-scale tectonic events. *Economic Geology*, *95*(8), 1657-1671.

Stein, H., Scherstén, A., Hannah, J., & Markey, R. (2003). Subgrain-scale decoupling of Re and ¹⁸⁷Os and assessment of laser ablation ICP-MS spot dating in molybdenite. *Geochimica et Cosmochimica Acta*, *67*(19), 3673-3686.

Sykora, S., Cooke, D. R., Meffre, S., Stephanov, A. S., Gardner, K., Scott, R., ... & Harris, A. C. (2018). Evolution of pyrite trace element compositions from porphyry-style and epithermal conditions at the Lihir gold deposit: implications for ore genesis and mineral processing. *Economic Geology*, *113*(1), 193-208.

Symons, D. T. A., Symons, T. B., & Sangster, D. F. (2000). Paleomagnetism of the Society Cliffs dolostone and the age of the Nanisivik zinc deposits, Baffin Island, Canada. *Mineralium Deposita*, *35*(7), 672-682.

Symons, D. T. A., Pannalal, S. J., Kawasaki, K., Sangster, D. F., Stanley, G. A., & Andrew, C. J. (2007). Paleomagnetic age of the Magcobar Ba deposit, Silvermines, Ireland. *Mineral exploration and research: Digging deeper: Dublin, Irish Association for Economic Geology*, 377-380.

Turner, E. C. (2009). Mesoproterozoic carbonate systems in the Borden Basin, Nunavut. *Canadian Journal of Earth Sciences*, *46*(12), 915-938.

Turner, E. C. (2011). Structural and stratigraphic controls on carbonate-hosted base metal mineralization in the Mesoproterozoic Borden Basin (Nanisivik District), Nunavut. *Economic Geology*, 106(7), 1197-1223.

Turner, E. C., Long, D. G., Rainbird, R. H., Petrus, J. A., & Rayner, N. M. (2016). Late Mesoproterozoic rifting in Arctic Canada during Rodinia assembly: impactogens, trans-continental far-field stress and zinc mineralisation. *Terra Nova*, 28(3), 188-194.1.

Van Acken, D., Su, W., Gao, J., & Creaser, R. A. (2014). Preservation of Re-Os isotope signatures in pyrite throughout low-T, high-P eclogite facies metamorphism. *Terra Nova*, 26(5), 402-407.

Vernon, R., Holdsworth, R. E., Selby, D., Dempsey, E., Finlay, A. J., & Fallick, A. E. (2014). Structural characteristics and Re–Os dating of quartz-pyrite veins in the Lewisian Gneiss Complex, NW Scotland: Evidence of an Early Paleoproterozoic hydrothermal regime during terrane amalgamation. *Precambrian Research*, 246, 256-267.

Vorlicek, T. P., Kahn, M. D., Kasuya, Y., & Helz, G. R. (2004). Capture of molybdenum in pyrite-forming sediments: role of ligand-induced reduction by polysulfides 1. *Geochimica et Cosmochimica Acta*, 68(3), 547-556.

Waters, C. N. (2011). A revised correlation of Carboniferous rocks in the British Isles. Geological Society of London.

Wilkinson, J. J., Eyre, S. L., Boyce, A. J. (2005). Ore-Forming Processes in Irish-Type Carbonate-Hosted Zn-Pb Deposits: Evidence from Mineralogy, Chemistry, and Isotopic Composition of Sulfides at the Lisheen Mine. *Economic Geology*, 100 (1), 63–86.

Wilkinson, J.J., 2010, A Review of Fluid Inclusion Constraints on Mineralization in the Irish Ore Field and Implications for the Genesis of Sediment-Hosted Zn-Pb Deposits: *Economic Geology*, v. 105, p. 417–442.

Wilkinson, J.J., and Hitzman, M.W, 2014, The Irish Zn-Pb Orefield: The View from 2014.1. In S.M. Archibald and S.J. Piercey, eds., *Current Perspectives in Zinc Deposits*. Irish Association of Economic Geology, 59-73.

Wilkinson, J. J., Vowles, K., Muxworthy, A. R., & Mac Niocaill, C. (2017). Regional remagnetization of Irish Carboniferous carbonates dates Variscan orogenesis, not Zn-Pb mineralization. *Geology*, 45(8), 747-750.

Woodcock, N., and Strachan, R., 2000, *Geological history of Britain and Ireland: Oxford, Blackwell Science*, 423 p.

Yin, L., Li, J., Liu, J., Li, C., Sun, S., Liang, H., & Xu, J. (2017). Precise and accurate Re–Os isotope dating of organic-rich sedimentary rocks by thermal ionization mass spectrometry with an improved H₂O₂-HNO₃ digestion procedure. *International Journal of Mass Spectrometry*, 421, 263-270.

Zhang, L., Xiao, W., Qin, K., Qu, W., & Du, A. (2005). Re–Os isotopic dating of molybdenite and pyrite in the Baishan Mo–Re deposit, eastern Tianshan, NW China, and its geological significance. *Mineralium Deposita*, 39(8), 960-969.

Zhang, P., Huang, X. W., Cui, B., Wang, B. C., Yin, Y. F., & Wang, J. R. (2016). Re-Os isotopic and trace element compositions of pyrite and origin of the Cretaceous Jinchang porphyry Cu-Au deposit, Heilongjiang Province, NE China. *Journal of Asian Earth Sciences*, 129, 67-80.

Figure Captions

Figure 1: (A) Map of Ireland showing Zn-Pb mineralization (modified from Wilkinson, 2010) (B) Location of samples referenced in this study.

Figure 2: Paragenetic sequence for Lisheen (A) The generalized paragenetic sequence and the subjective location of the various observed textures seen in processed samples from this study (8S08FW and LK 359) and LK 451 from Creaser et al. (2009) (B) Observed textures – LG5/LG6 (Backscattered electron (BSE) image from LK 359), LG1/LG2 (BSE image from LK 451), LG3/LG4 (Reflected light image from LK 451), LG7 (BSE image from 8S08FW). Large star = major component, small star = minor component.

Figure 3: (A) Hand sample of 8S08FW (B) Backscattered electron image (BSE) emphasizing the different phases present.

Figure 4: (A) Hand sample LK 359 (B) Representative BSE image of LK 359 (C) Reflected light on the left side of the image and transmitted light on the right side of the image showing the boundary between LG6 sphalerite/illite intermixed with LG1-LG3 pyrite (D) Reflected light image showing the transitions between LG1-LG3.

Figure 5: Location of Nanisivik and Hawker Creek (modified from Turner, 2011).

Figure 6: (A) Hand Sample of 03-HC-8D from Hawker Creek (B) Highly fractured area in 03-HC-8D (C) Reflected light image of 03-HC-8D showing clean coarse pyrite cores.

Figure 7: Representative BSE images of mineral separates of high and low magnetic susceptibility that have underwent heavy liquid separation and magnetic separation. (A)-(B) Sample 8S08FW (C)-(D) Sample LK 359 (E)-(F) Sample 03-HC-8D.

Figure 8: (A) Model 3 isochron for 8S08FW, modified from Hnatyshin et al. (2015) (B) Expanded region for the samples that have undergone HCl leaching procedures, showing that they do not deviate from the regression line of the isochron. Orange ellipses represent leached data points and blue ellipses represent non-leached data points.

Figure 9: (A) Model 3 Isochron for LK 359. Samples selected for SIMS sulfur isotope measurements are indicated (B) Model 3 isochron using the samples that contain the lowest impurities (LK359B NM1.6 and samples leached in 10N HCl). Orange ellipses represent leached data points, blue ellipses represent non-leached data points.

Figure 10: Histograms of SIMS sulfur isotope measurements for Lisheen. Lightly dashed lines indicate interpreted divisions between specific generations. (A) Main Zone sample 8S08FW (B) Derryville Sample LK 359.

Figure 11: SIMS sulfur isotope measurements for the Main Zone and Derryville Zones along transects highlighted in Figure A3. (A)-(D) Main Zone sample 8S08FW-1 (E)-(G) Derryville samples LK 359-1 and LK 359-2. Data points are scaled to the sizes of SIMS spots.

Figure 12: LA-ICPMS images for Lisheen Main Zone rock fragment 8S08FW-1.

Figure 13: LA-ICPMS images for Lisheen Derryville Zone rock fragment LK 359-1.

Figure 14: LA-ICPMS images for Hawker Creek rock fragment HC.

Figure 15: Areas containing anomalous Mo and Re contents that may indicate micron scale molybdenite crystals in LK 359-1 Map Location 3.

Figure 16: Correlograms for Derryville Sample LK 359. (A) Non-normalized. (B) Normalized to Re (Concentration of Re - Concentration of element X).

Figure 17: Single pixel concentrations of selected elements (Mo, Co, As, and K) vs. Re from LA-ICPMS maps. Datapoints were screen to obtain primarily sulfide phases (total ppm > 500000, Zn (ppm) < 10000, Pb (ppm) < 10000, Si (ppm) < 10000). *Unpublished map data from sample LK 451 from Lisheen Bog Zone. ** Unpublished map data from Nanisivik sample NOV4 (see Hnatyshin et al. 2016 for sample description).

Table Captions

Table 1: The concentrations of these phases should be taken as upper estimates as not all phases are accounted for. A designation of "x" means the abundance of that phase is expected to be < 5%, while a designation of "xx" means the phase is expected to be > 5%. The relative magnetic susceptibility (χ) between rocks or rock fragments is given in the second column where higher values refer to higher χ values. Rock fragments that cannot be compared via χ are separated by a dotted border or an empty row. Bracketed values are estimated values based known trends and observations. *Includes marcasite.

Table 2: Lisheen Main Zone Re-Os data. In the "Separation Procedure" column the first value reported is the grain size of the mineral separate in μm . If the sample has undergone magnetic separation the designation "Mag" is given. If the sample has undergone acid leaching the concentration of HCl used for the leaching procedure is given, and if the temperature was elevated beyond room temperature the temperature is also given. For example, the designation "74-210 / Mag / 10N HCl @ 80C" states that the sample contains grains 74-210 μm in size, has underwent magnetic separation, and has been leached with 10N HCl at 80°C. All samples unless otherwise stated (i.e. 'No HL') have underwent heavy liquid separation. The relative magnetic susceptibility (χ) between rocks or rock fragments is given in the third column where higher values refer to higher χ values. Model ages are determined using an initial Os ratio of 0.25. Initial ratio calculations are based off an age of 347 Ma. Original data and blanks can be obtained from Hnatyshin et al. (2015).

Table 3: Lisheen Derryville Zone Re-Os data. The meaning of each data column is described in the caption of Table 1. *Blanks values: Os = 0.05 ± 0.01 pg, $^{187}\text{Os}/^{188}\text{Os}$ = 0.18 ± 0.06 , Re = 1.1 ± 0.6 pg. ** Blanks values: Os = 0.34 ± 0.03 pg, $^{187}\text{Os}/^{188}\text{Os}$ = 0.23 ± 0.05 , Re = 2.5 ± 1.5 pg.

Table 4: Hawker Creek Re-Os data from Hnatyshin et al. (2016). The meaning of each data column is described in the caption of Table 1. Original blank data can be obtained from Hnatyshin et al. (2016).

Supplementary Information:

Figure A1: Leaching experiments using pure mineral samples obtained from the Mineralogy and Petrology Collection at the University of Alberta. The procedure was as follows: These minerals were first crushed to a size equivalent used for typical Re-Os analysis (74-210 μm) and $\sim 100\text{mg}$ was added to a 22 mL glass vial, which is then weighed. The samples are then leached at either room temperature ($\sim 21^\circ\text{C}$) or $\sim 80^\circ\text{C}$ using HCl at a concentration of 0.2N, 1N, 6N, or 10N. After ~ 24 hours the acid was decanted, the sample rinsed, and then dried. The vial + sample is then reweighed, which is then used to calculate the amount of sample that was dissolved (or lost during rinsing). Although not indicated on the plot, identical experiments were also done on calcite and dolomite, resulting in full dissolution after 24hrs. Magnetite and galena were not experimented with using 10N HCl at 80°C as complete dissolution was completed in prior experiments.

Figure A2: ICPMS analyses of mineral separates that have underwent magnetic separation and heavy liquid separation. (A) 8S08FW (B) LK 359A (C) LK 359B (D) 03-HC-8D. *Concentrations of Re are at the ppb level, Os at the ppt level, and other elements at the ppm level.

Figure A3: Areas chosen for SIMS sulfur isotope measurements and LA-ICPMS compositional mapping. All images are scale to the same size.

Figure A4: Hypothetical dataset with variable VIOs. The $^{187}\text{Re}/^{188}\text{Os}$ values of 1000 - 6000, 2σ errors of 10%, and a rho value of 0.75 were chosen arbitrarily, but fall within normal ranges seen in pyrite analyses. The $^{187}\text{Os}/^{188}\text{Os}$ values are calculated based on these parameters at an age of 350 Ma and then a regression is calculated using Isoplot. (A) VIOs is invariant with each $^{187}\text{Os}/^{188}\text{Os}$ being calculated using an initial $^{187}\text{Os}/^{188}\text{Os}$ of 1.00. (B) $^{187}\text{Os}/^{188}\text{Os}$ is calculated using an initial $^{187}\text{Os}/^{188}\text{Os}$ of 1.00 or 1.10. (C) $^{187}\text{Os}/^{188}\text{Os}$ is calculated using an initial $^{187}\text{Os}/^{188}\text{Os}$ of 1.00 or 1.50. (D) $^{187}\text{Os}/^{188}\text{Os}$ is calculated using an initial $^{187}\text{Os}/^{188}\text{Os}$ of 1.00 or 2.00. From these figures the Model 3 regressions correctly identify the approximate variability $^{187}\text{Os}/^{188}\text{Os}$ experienced by a hypothetical sample. However, this variability greatly affects the precision of the data. In practice it would be imperative to find relationships (e.g. paragenetic relationships) between the samples that lie on the red "True Regression" lines to support the assumption that variability in initial osmium is real.

Figure A5: SIMS sulfur isotope measurements compared to the trace element character at the spot locations. (A) Lisheen data (B) Baffin Island data using the sulfur isotope measurements from Hnatyshin et al. (2016), and unpublished compositional data for Nanisivik sample NOV4, which is described in Hnatyshin et al. (2016).

Figure A6: Rhenium concentration as a function of the magnetic susceptibility of the mineral separate. For these samples, the Frantz isodynamic separator was run at identical settings with the horizontal axis representing the current used. Data in the 0 - 2.0 amp range used a side slope of 5° . Data in the > 2.0 amp band are mineral separates that remain non-magnetic at 2.0 amps and a side slope at 5° . Separates in the >2.0+ amp band remain non-magnetic at 2.0 amps and a side slope of 3° . The colored horizontal bars represent the range in magnetic susceptibility within a single mineral separate.¹Creaser et al. (2009), ²Hnatyshin et al. (2015), ³Acken et al. (2014).

Figure 1 - Lisheen Map and Crosssection

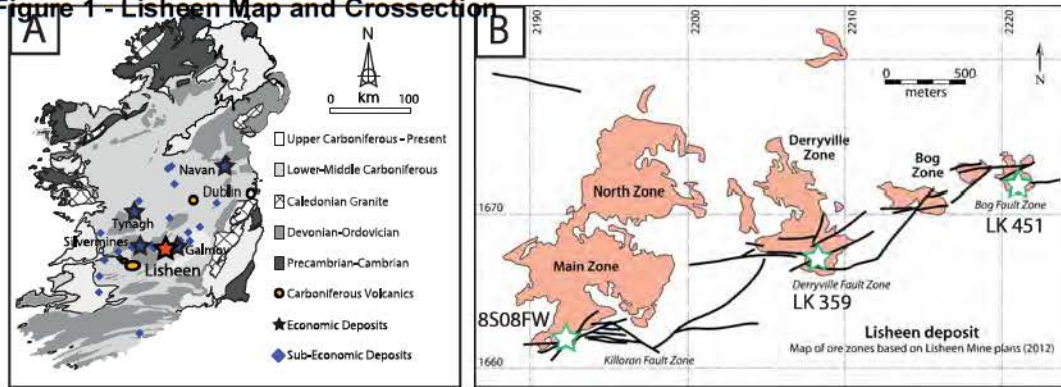


Figure 2- Pargenetic Sequence - Lisheen

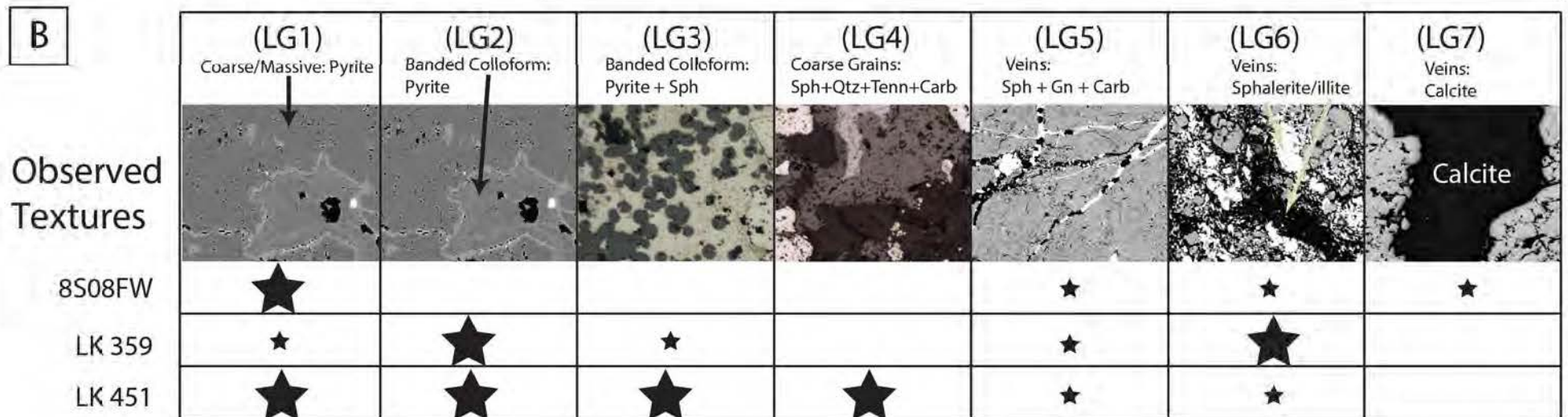
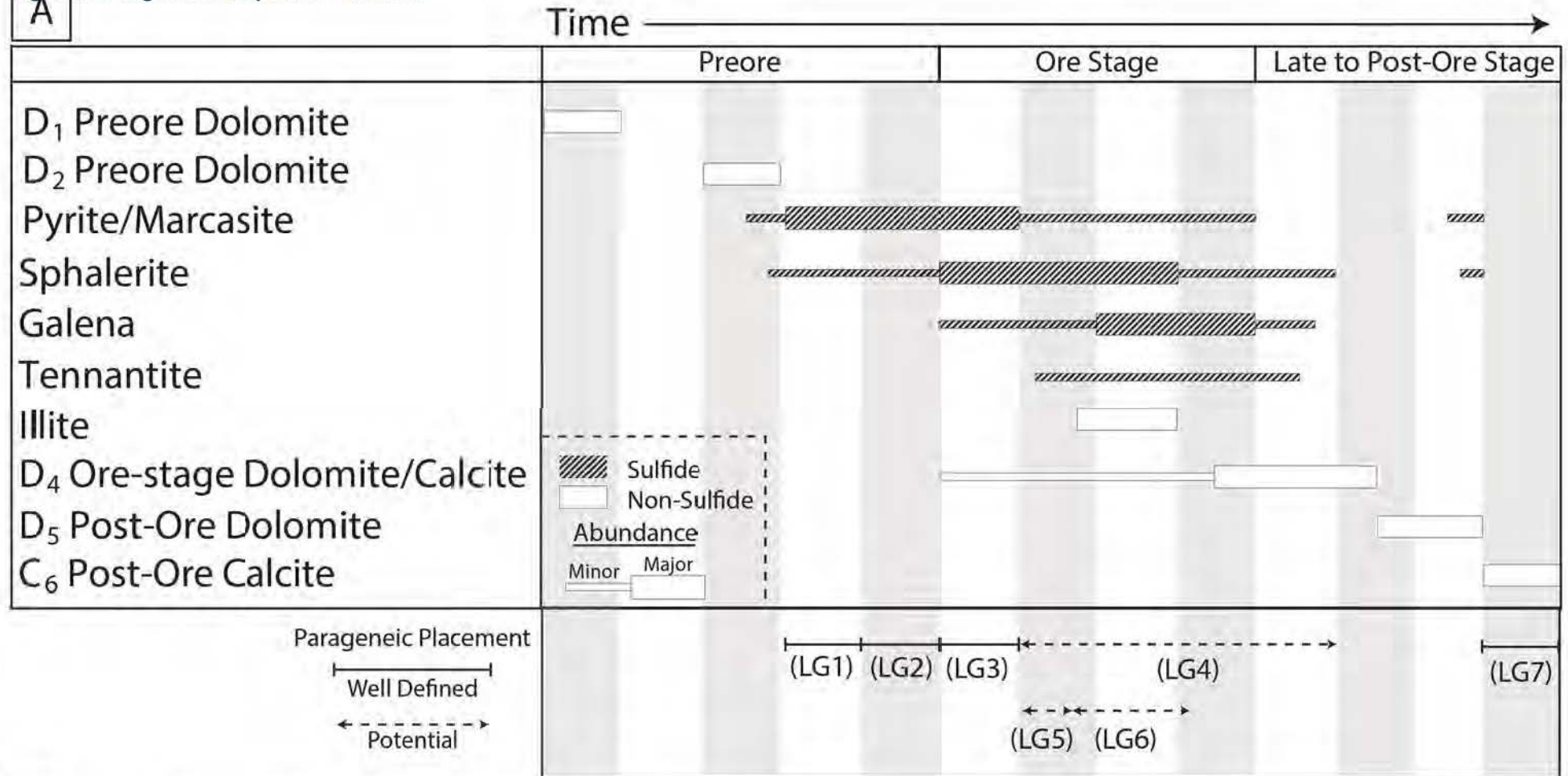


Figure 3-18S08FW Rock BS Microscope Pictures

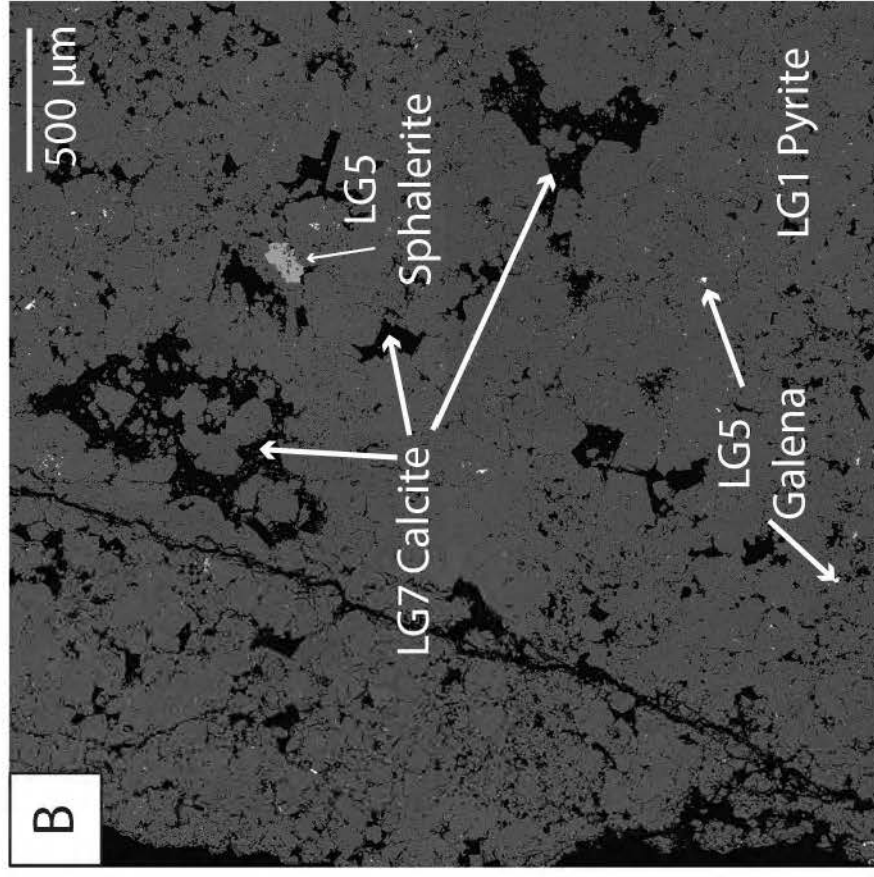
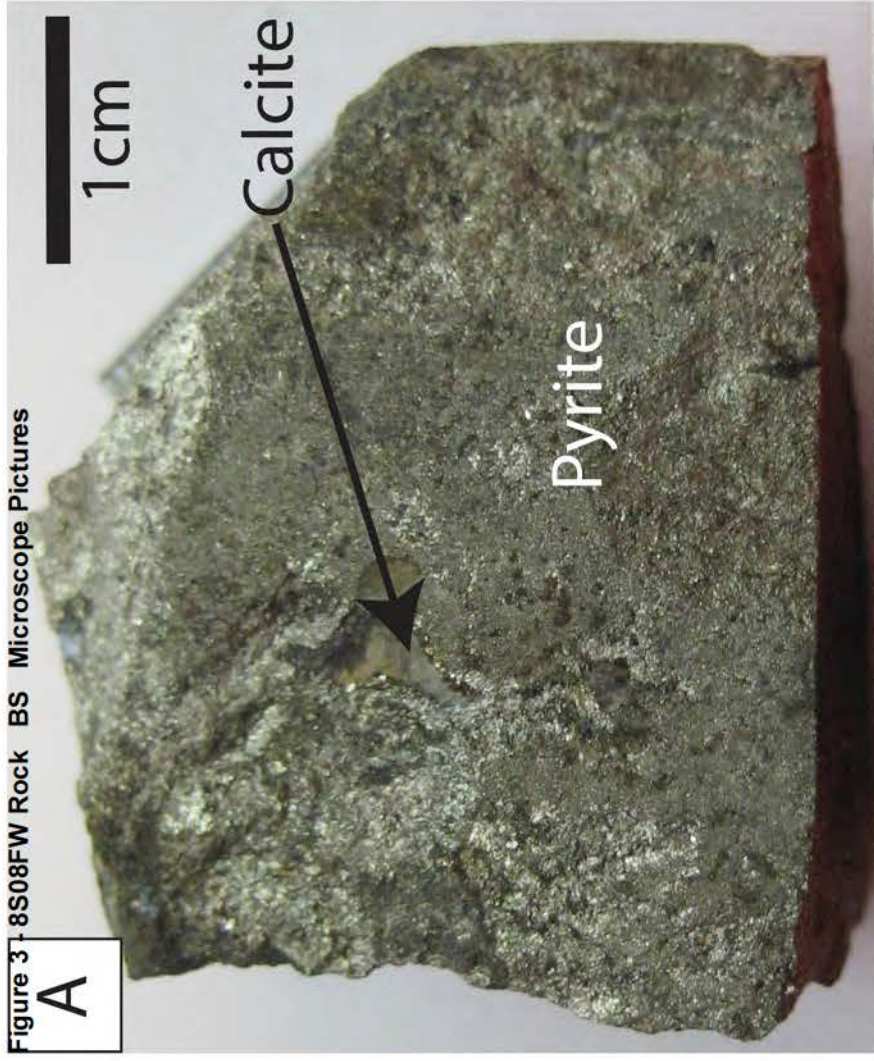


Figure 4: LK389 Rock - BS - Microscope Pictures

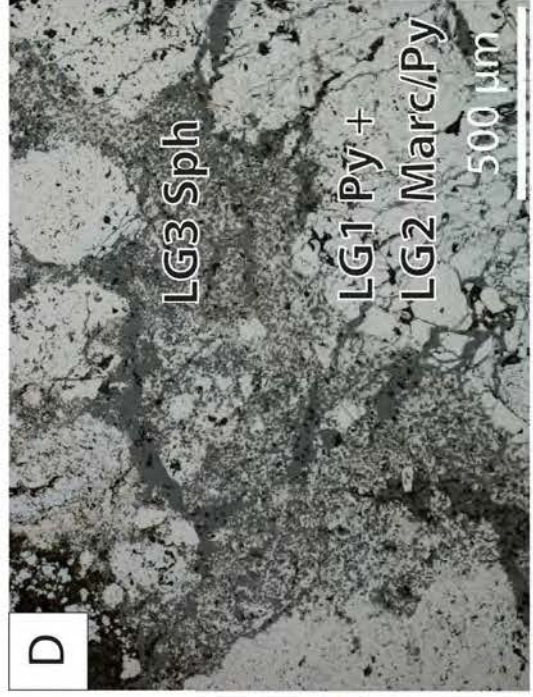
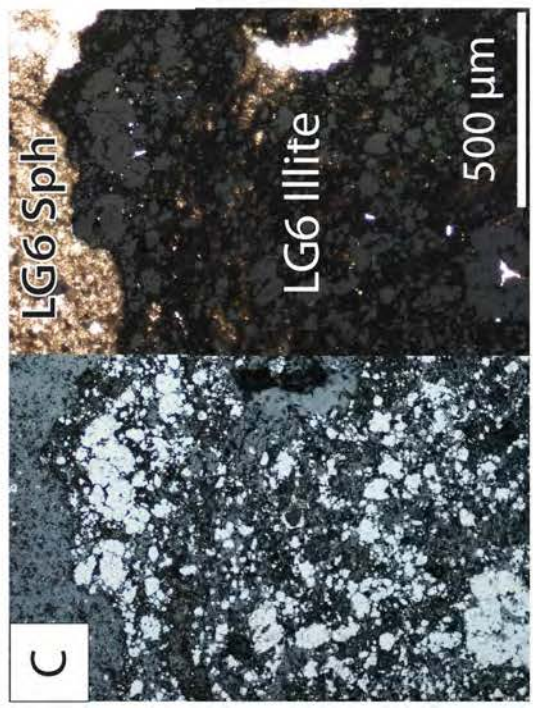
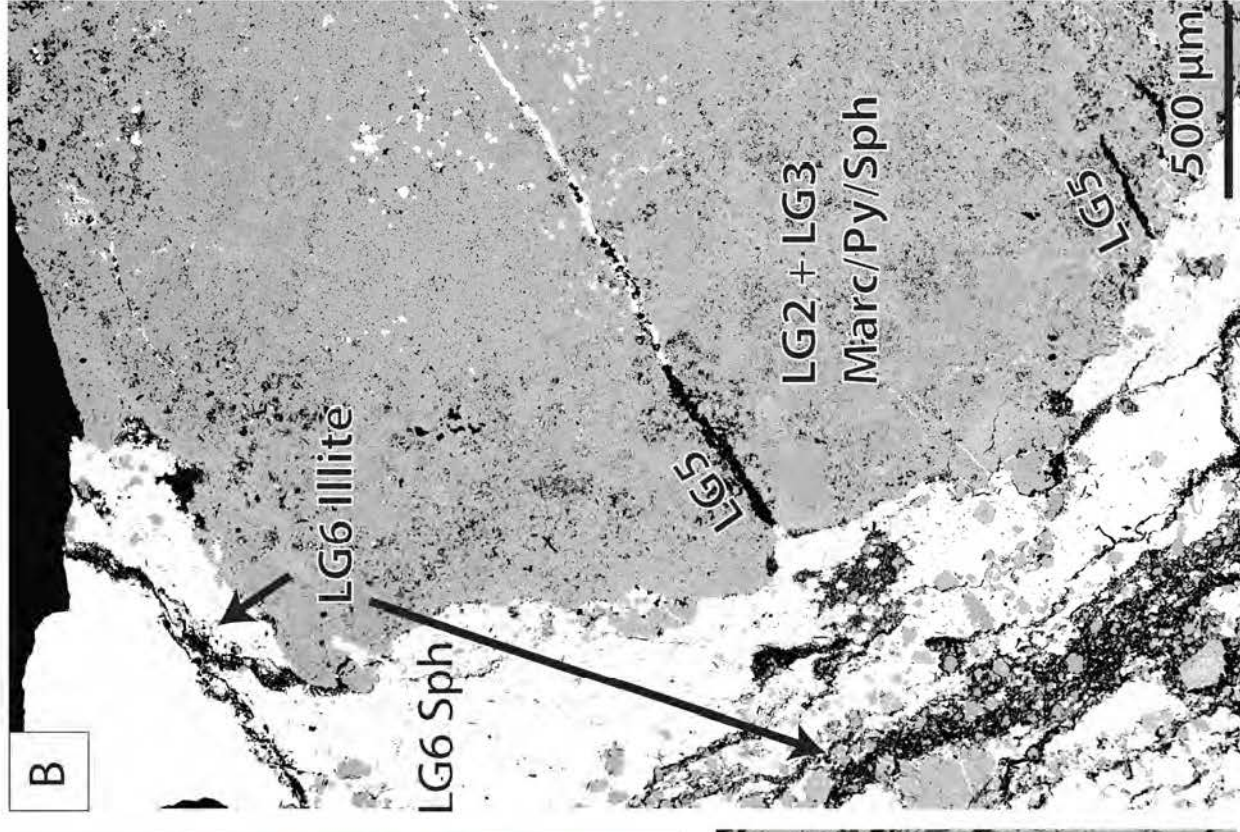
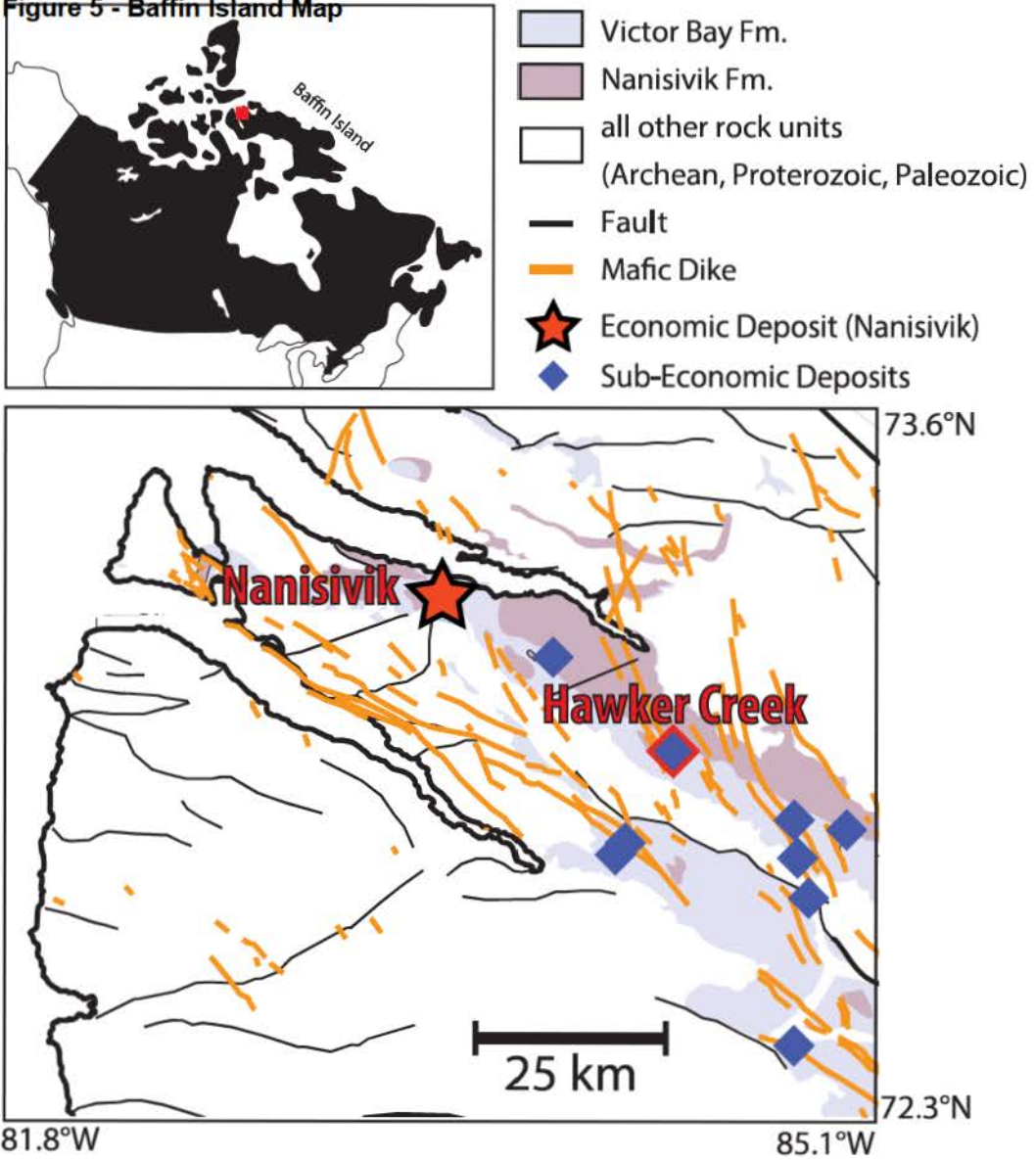
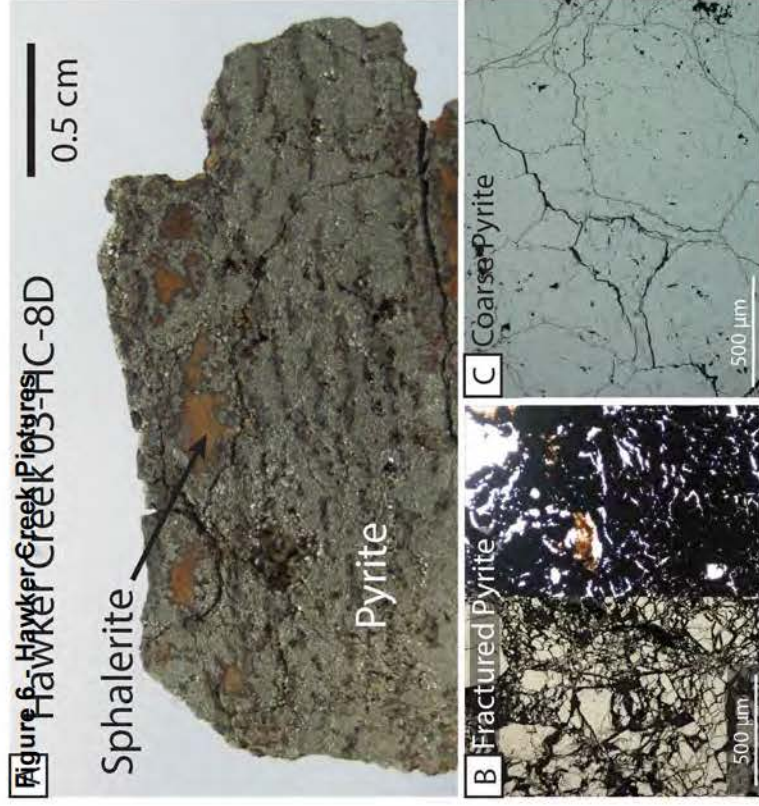


Figure 5 - Baffin Island Map





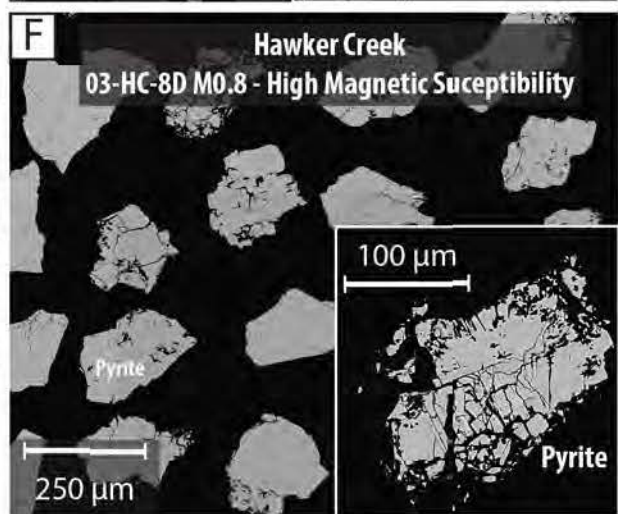
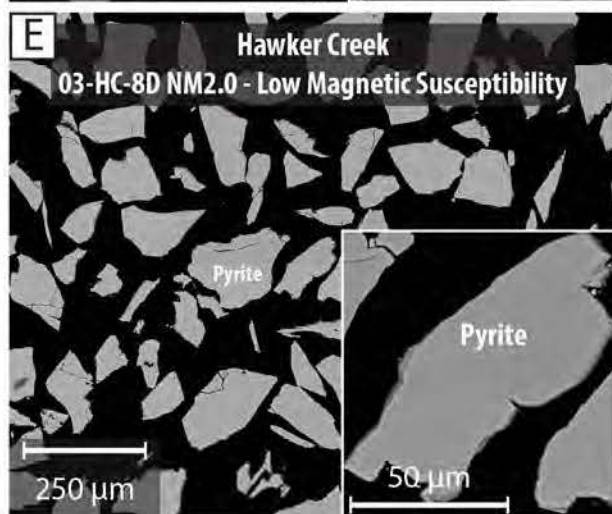
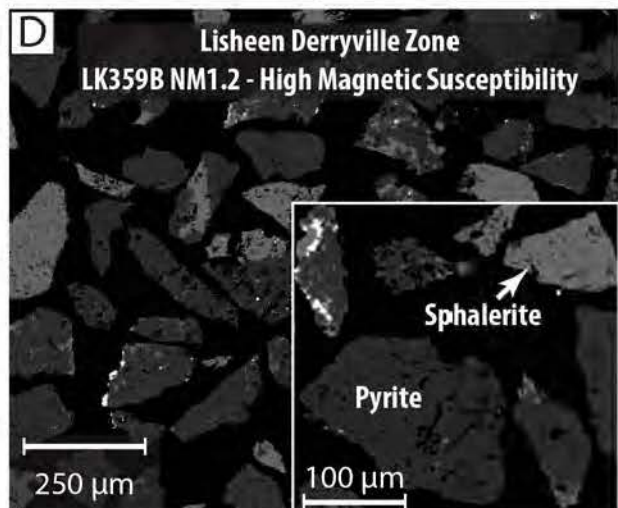
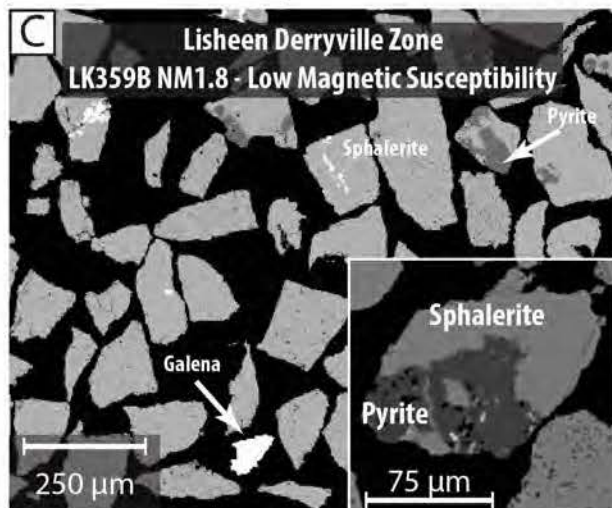
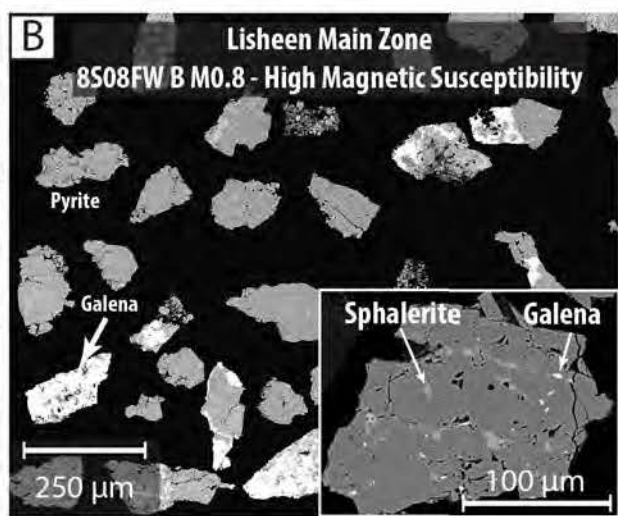
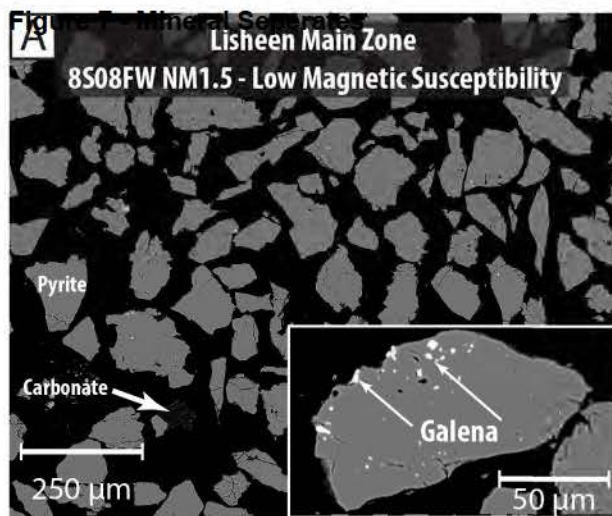
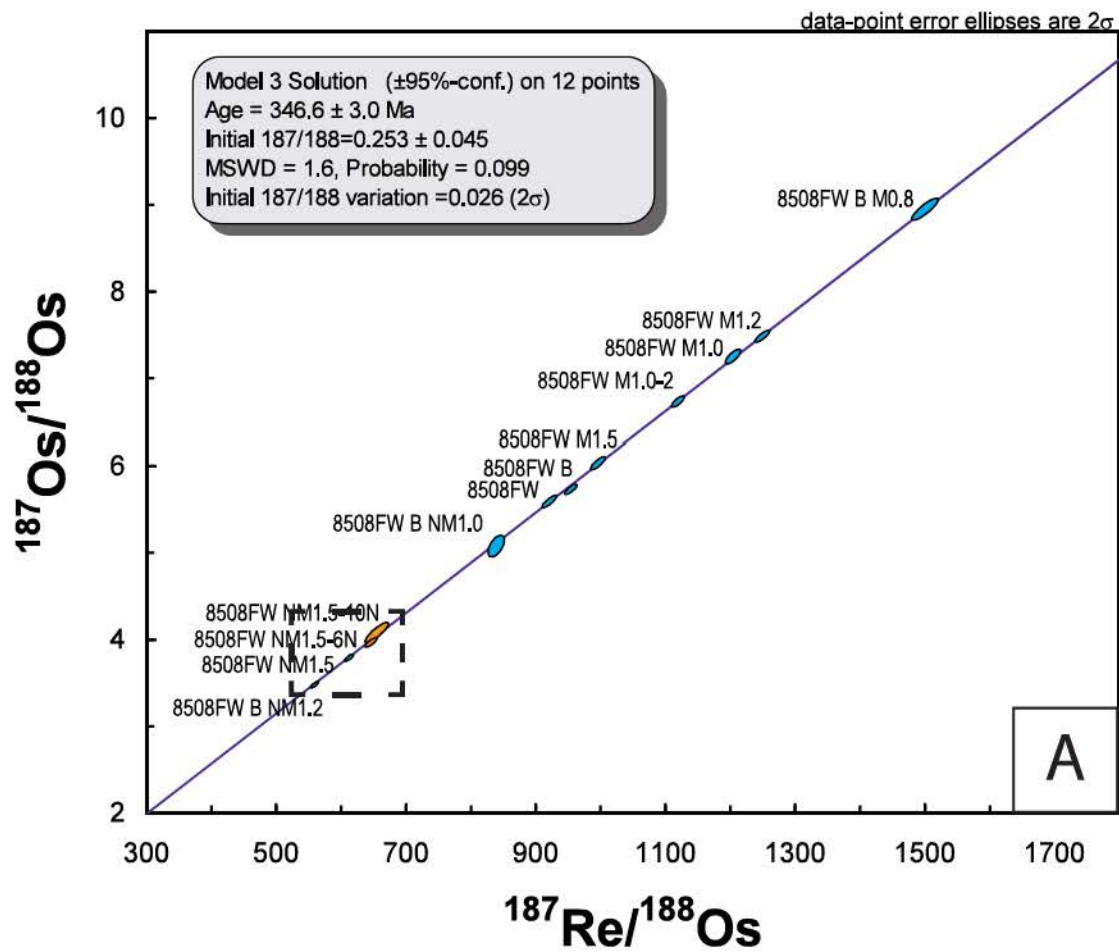


Figure 8 - 8S08FW Isochron

Lisheen Main Zone - 8S08FW



Location of Leached Pyrite

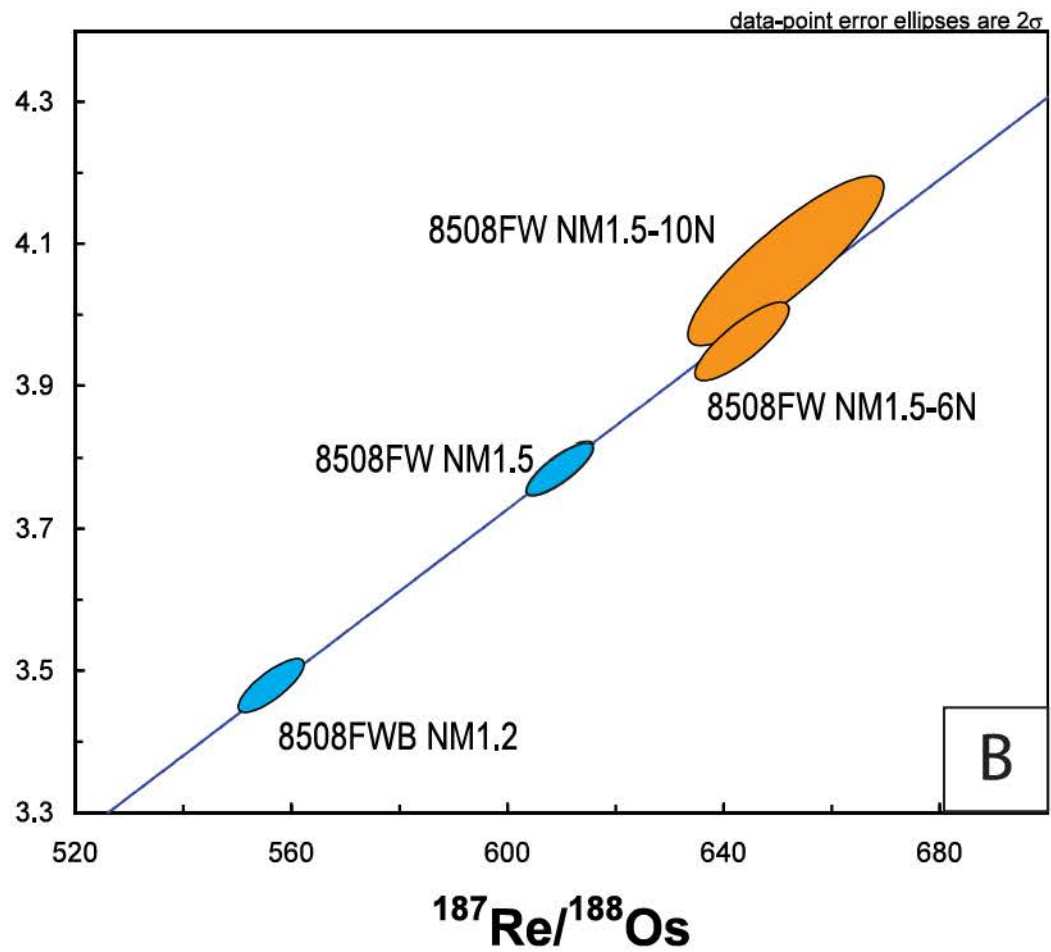


Figure 9 - LK 359 Isochron

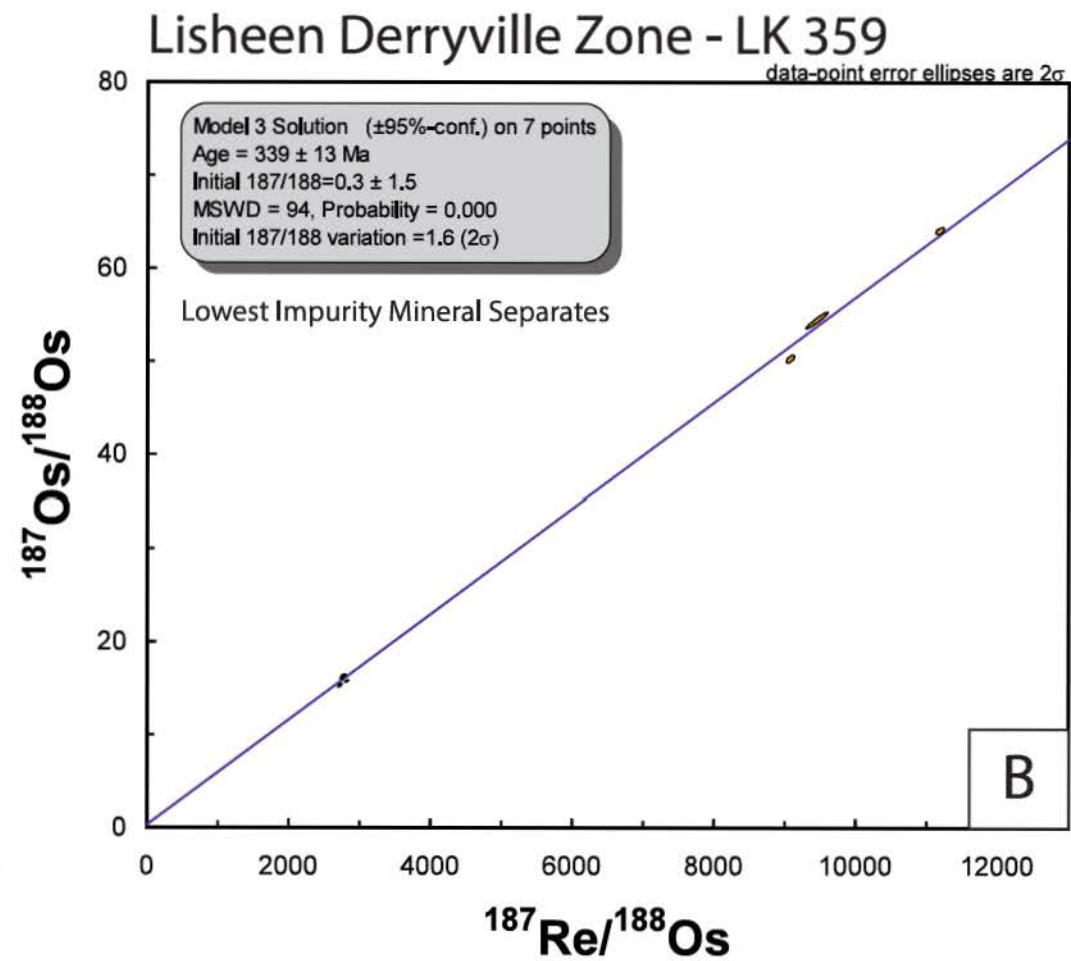
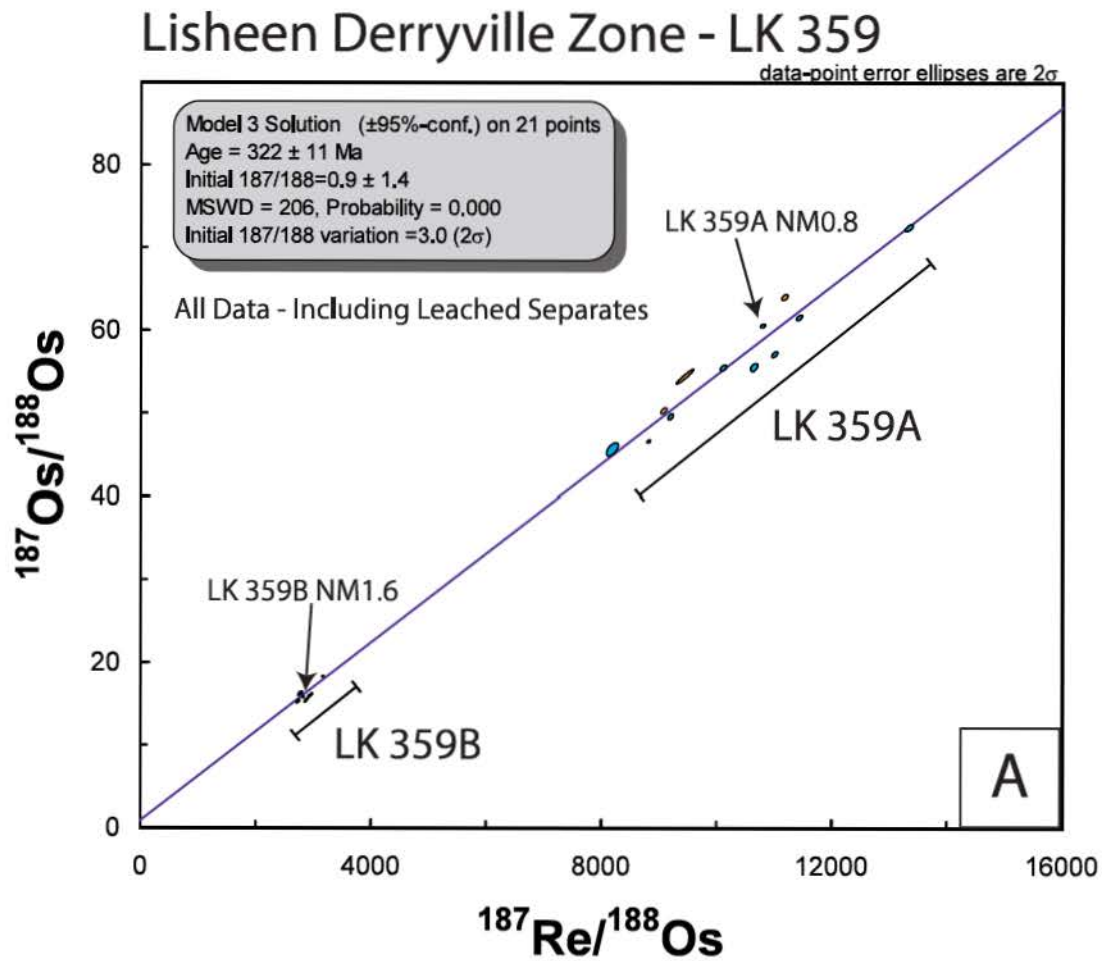
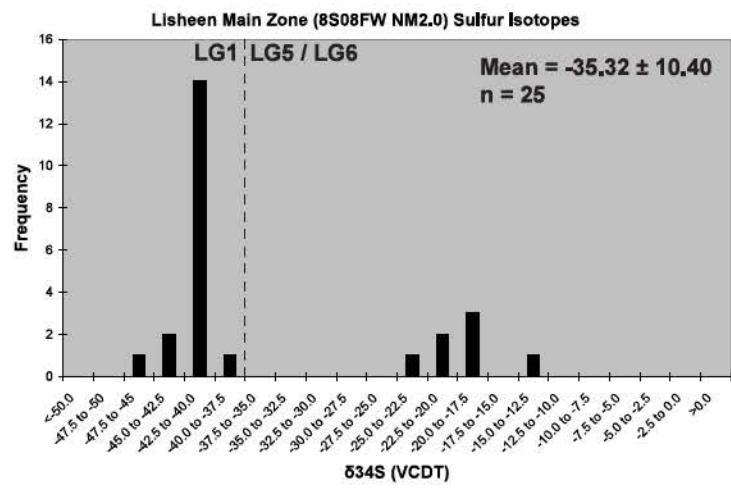
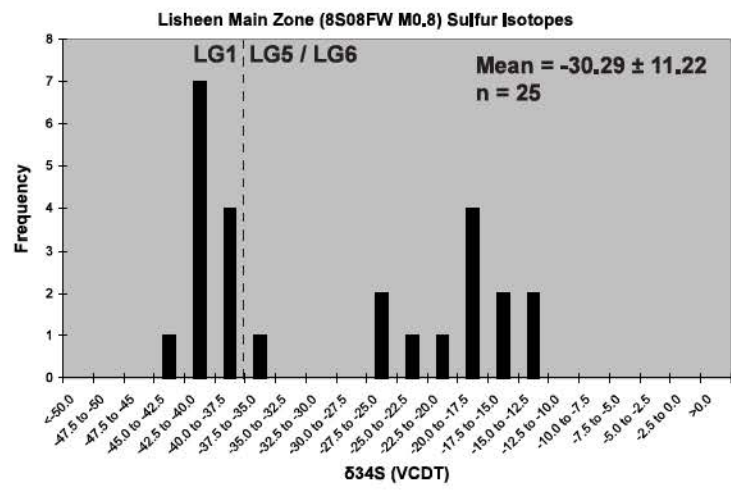
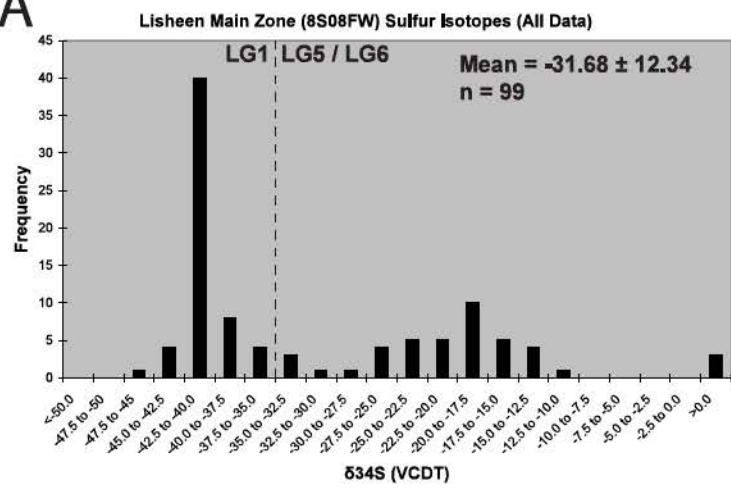
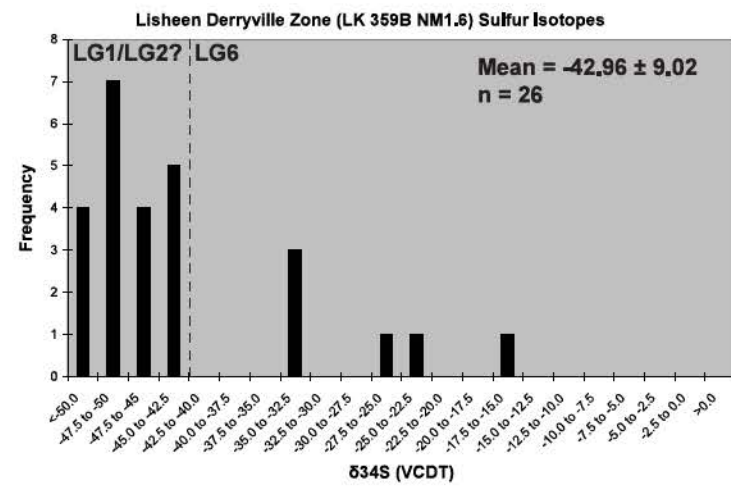
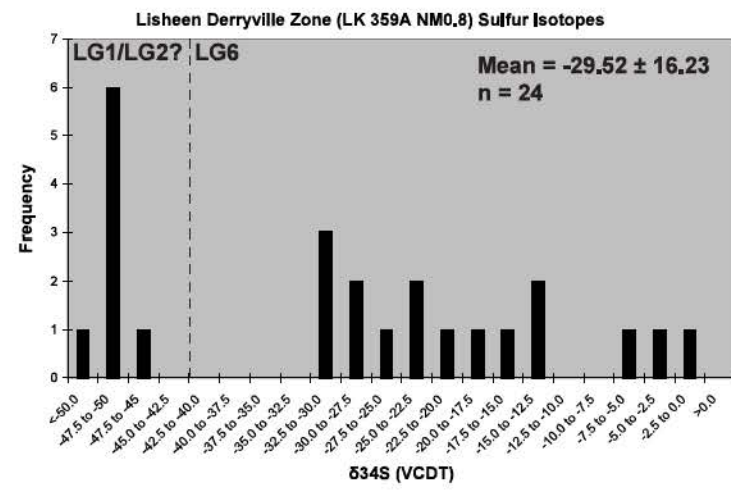
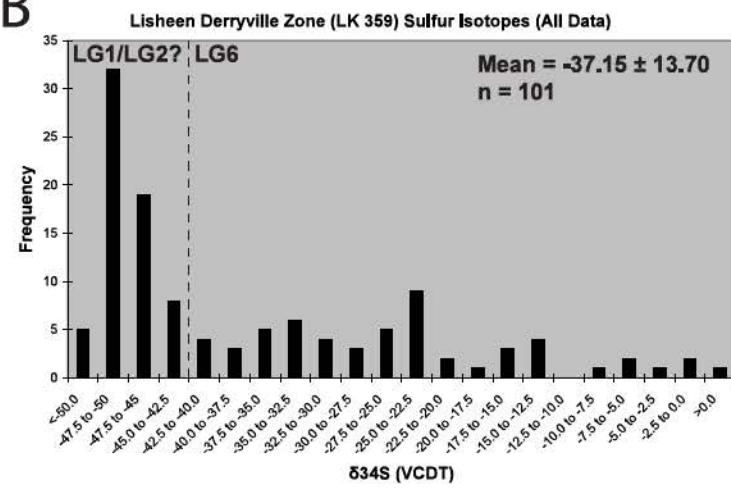


Figure 10 - Sulfur Isotope Histograms Lisheen

A

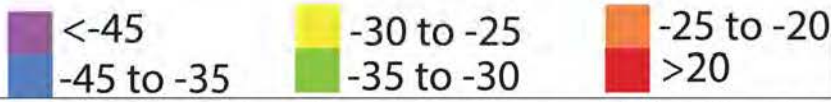


B

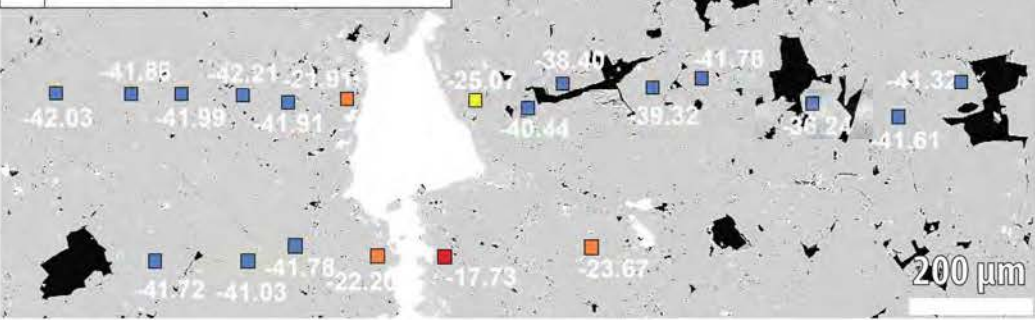


SIMS Sulphur Isotope Measurements

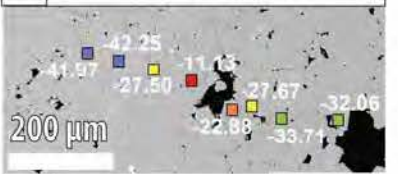
$\delta^{34}\text{S}$



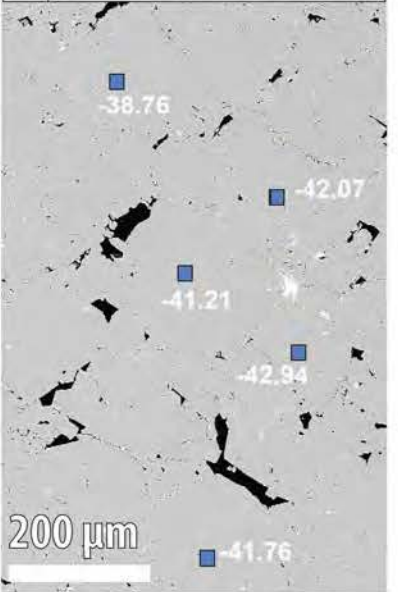
A 8S08FW Transect 1 and 2



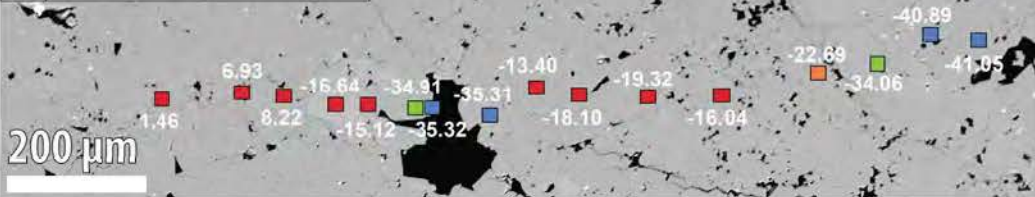
B 8S08FW Transect 3



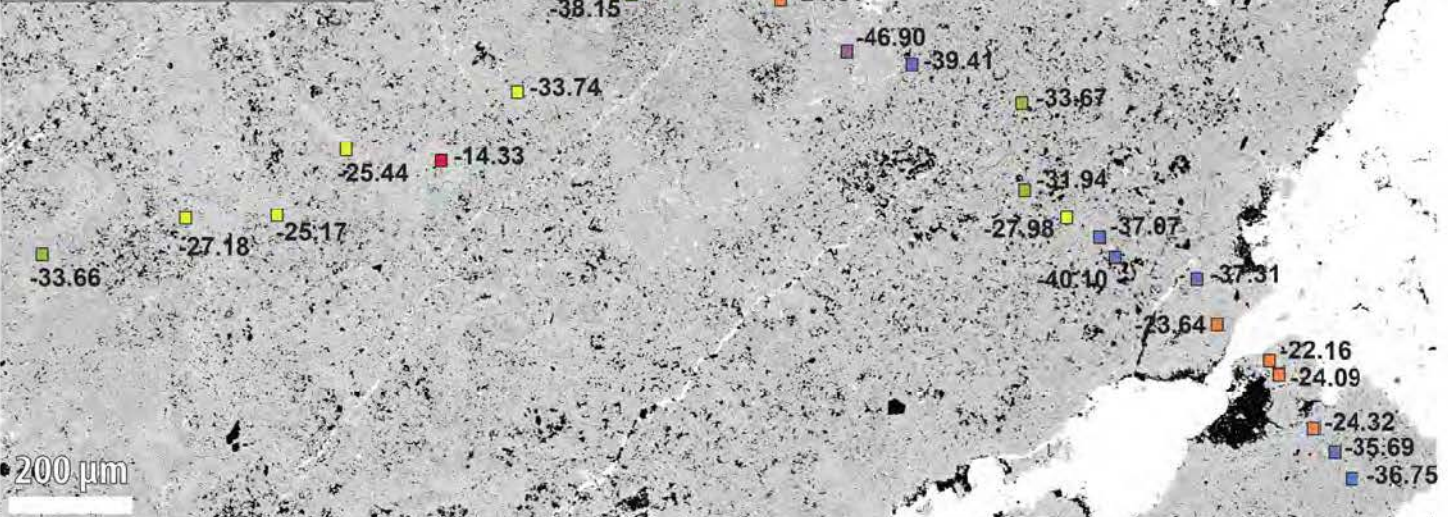
D 8S08FW Transect 5



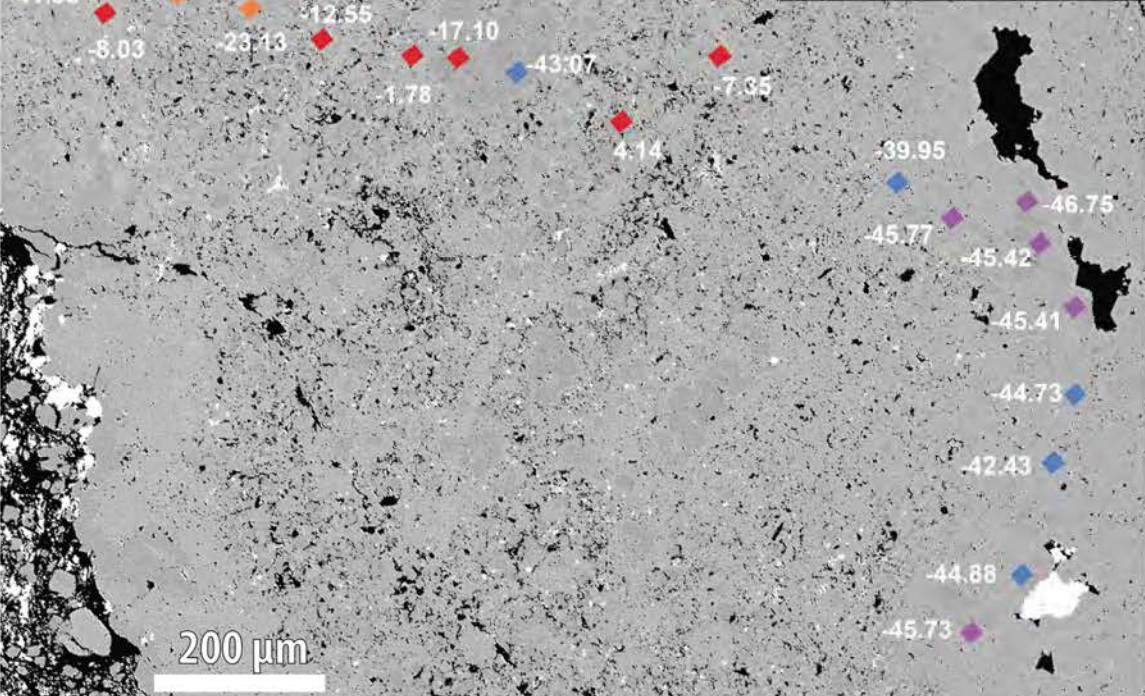
C 8S08FW Transect 4



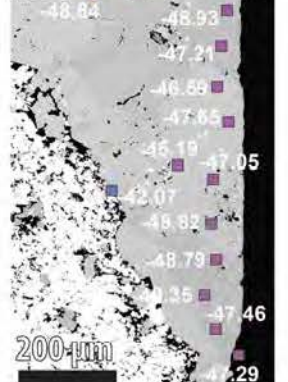
E LK 359-1 Transect



F LK 359-2 Location 1



G LK 359-2 Location 2



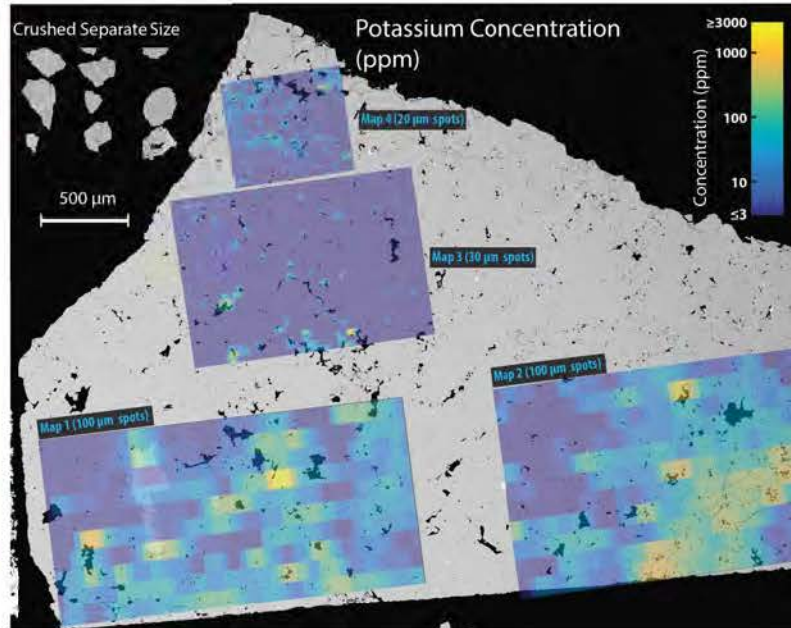
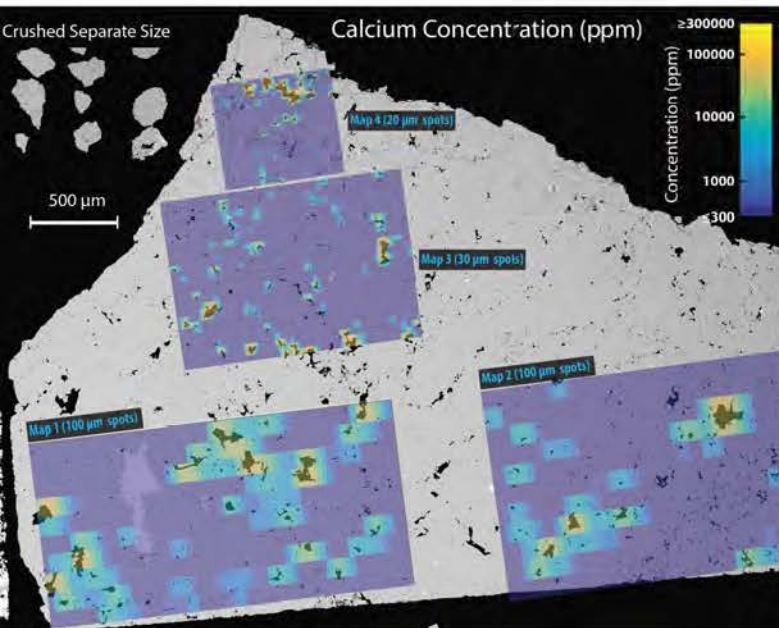
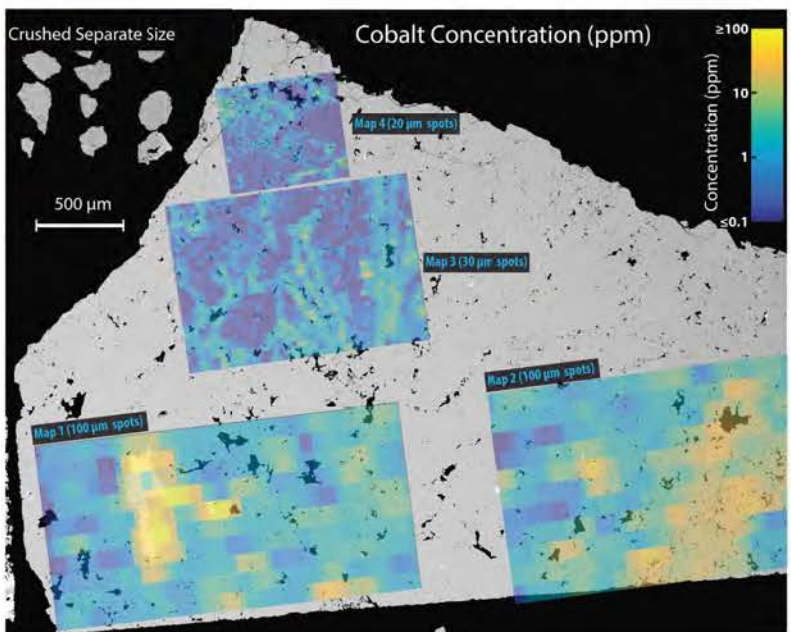
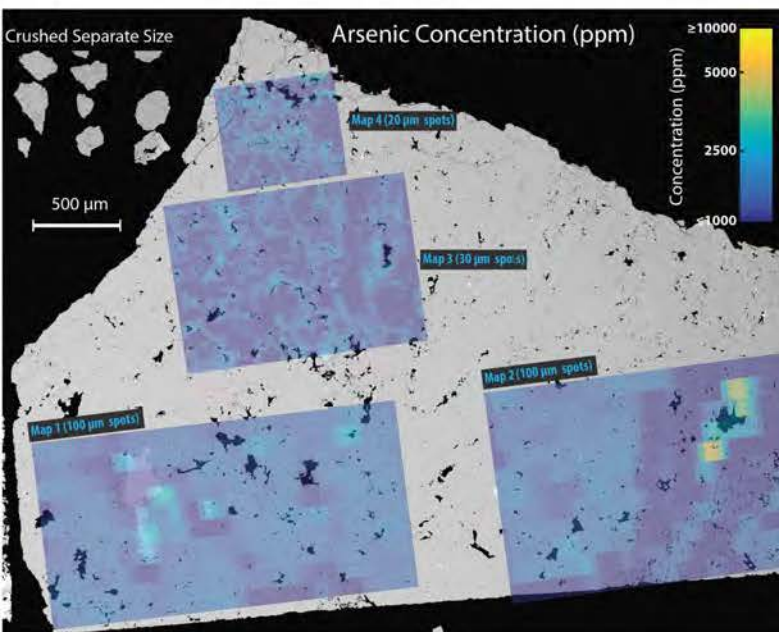
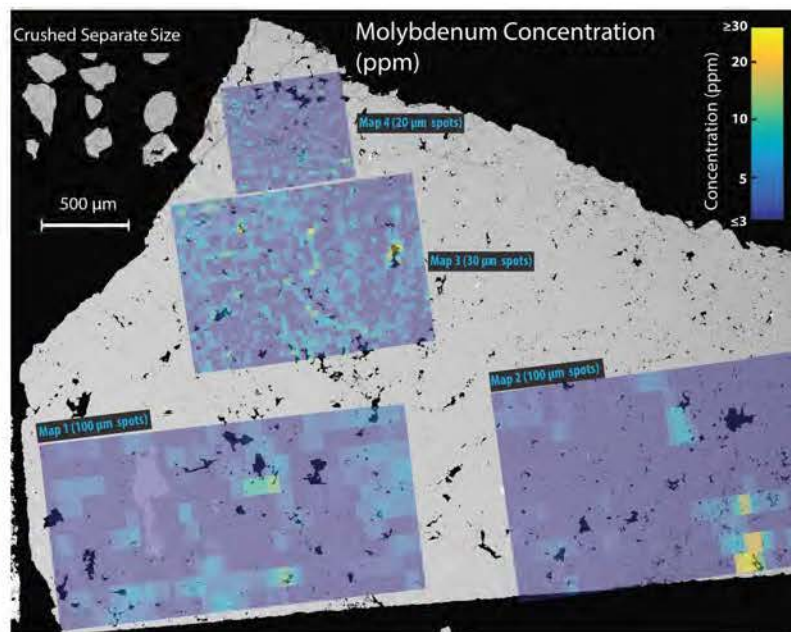
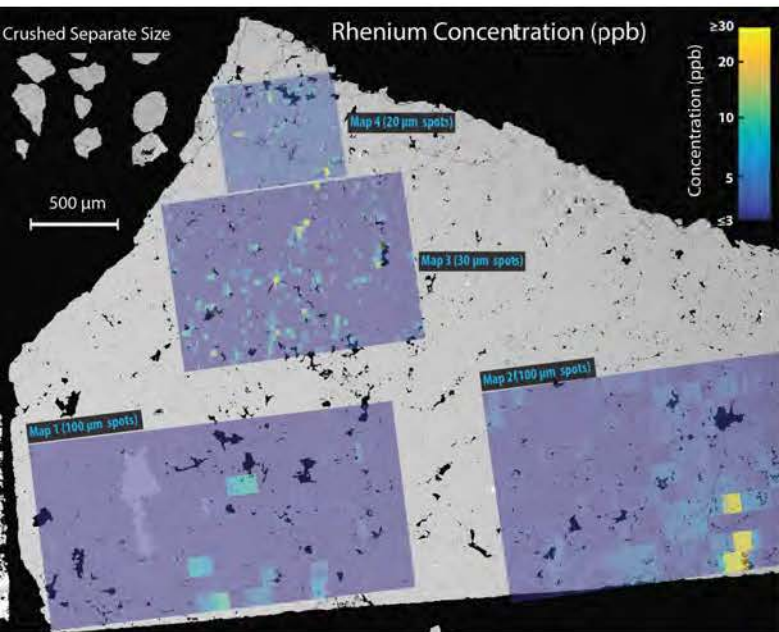
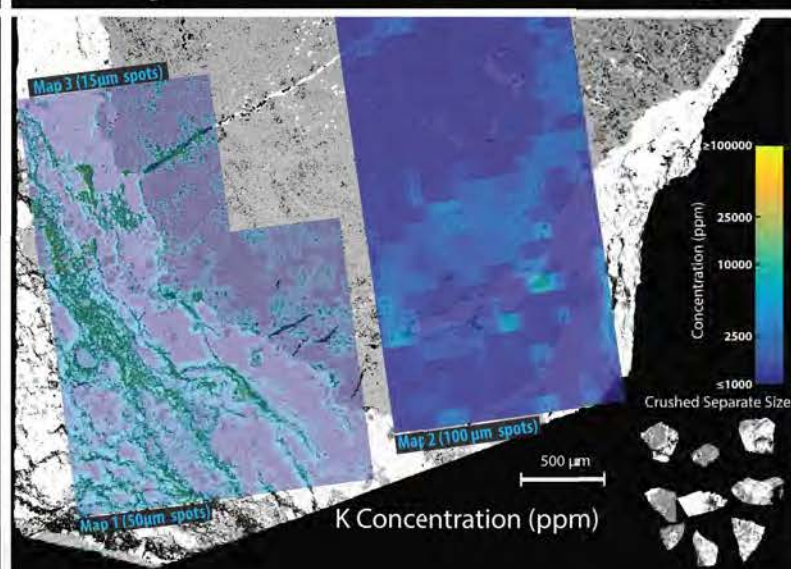
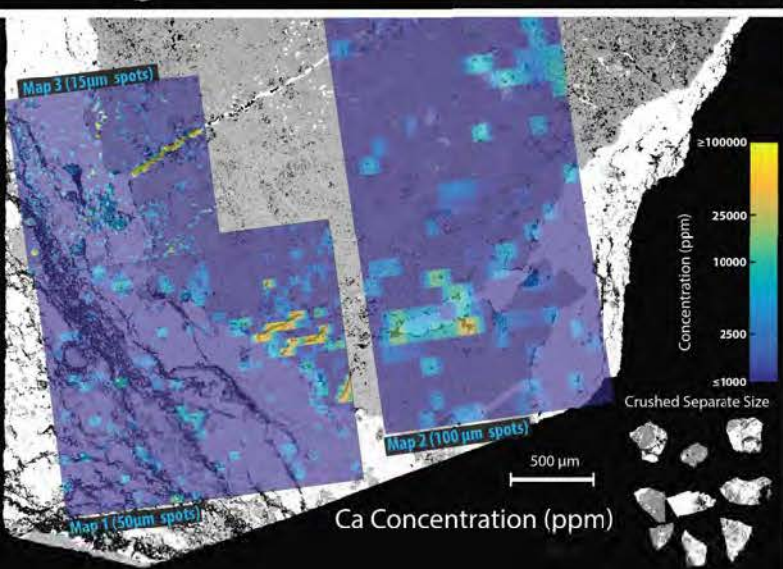
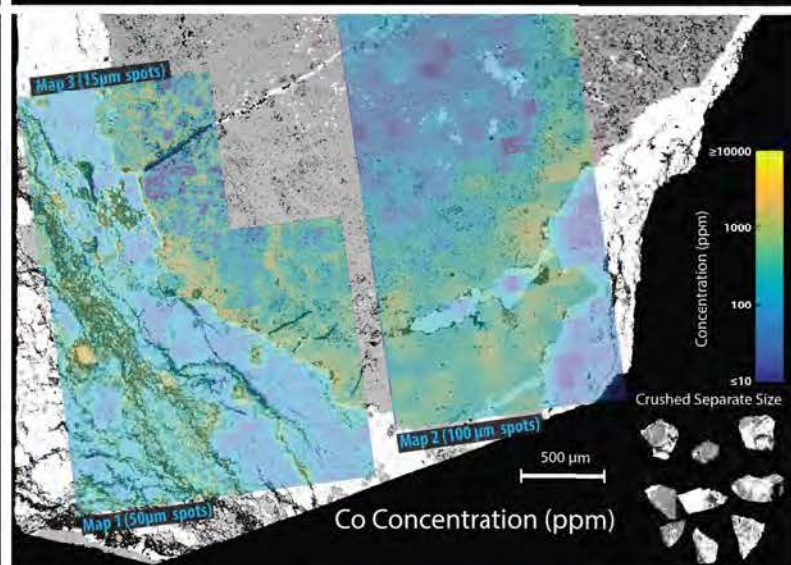
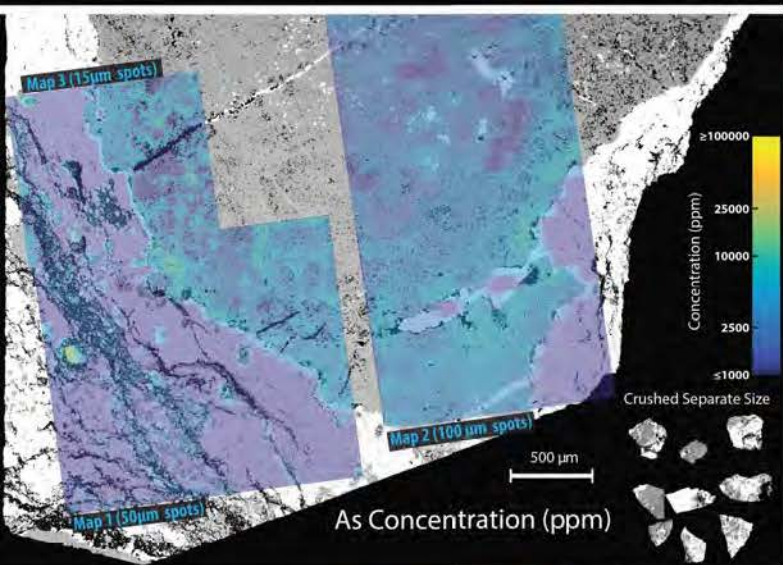
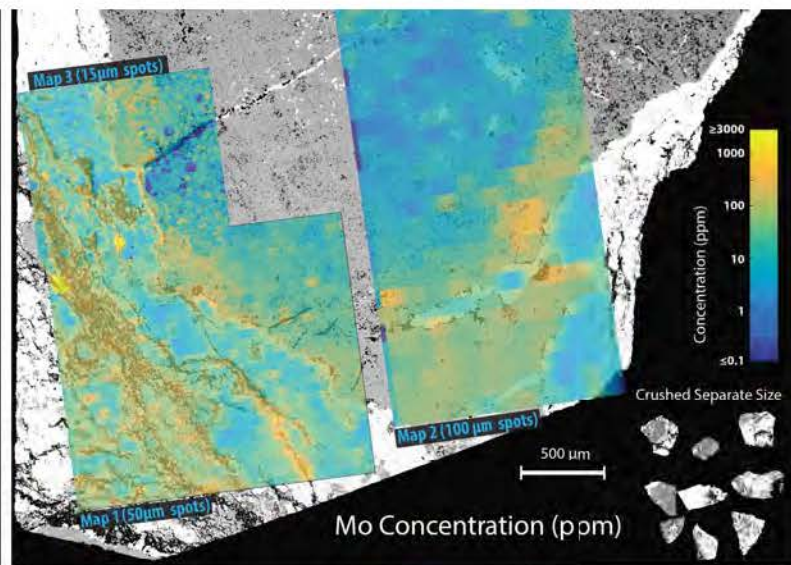
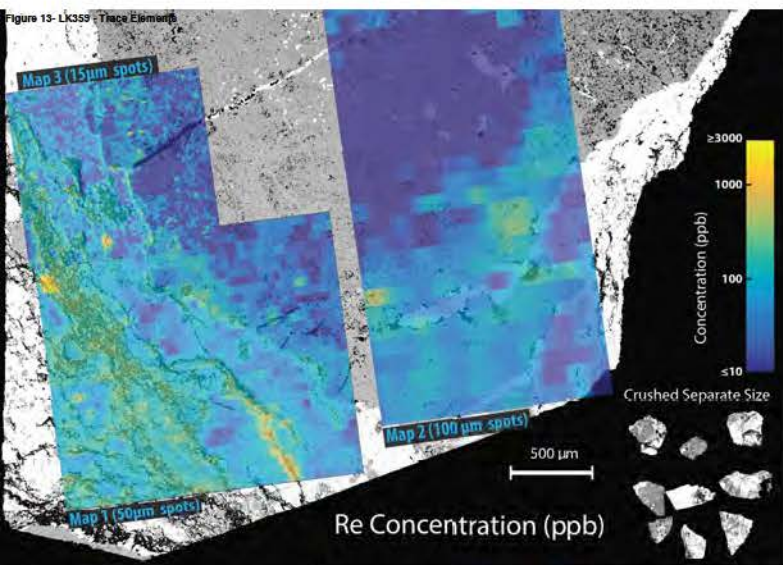


Figure 13- LK359 - Trace Element



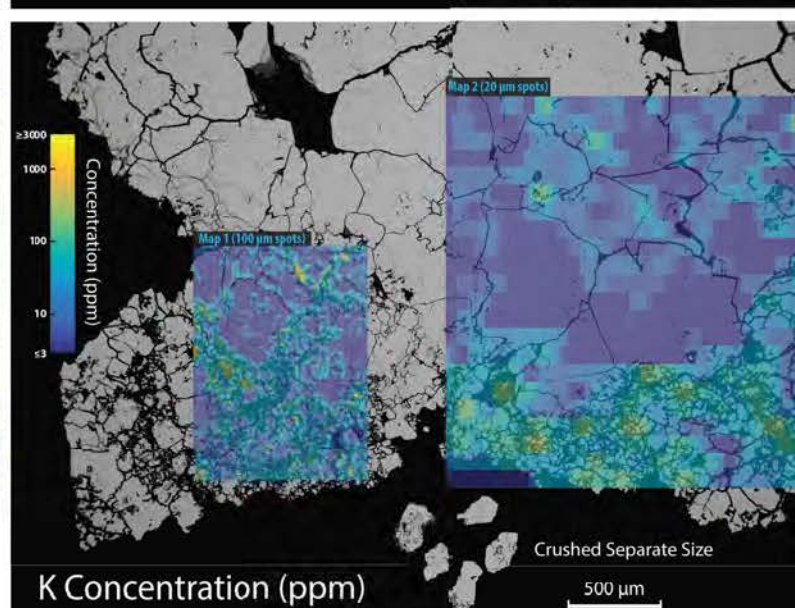
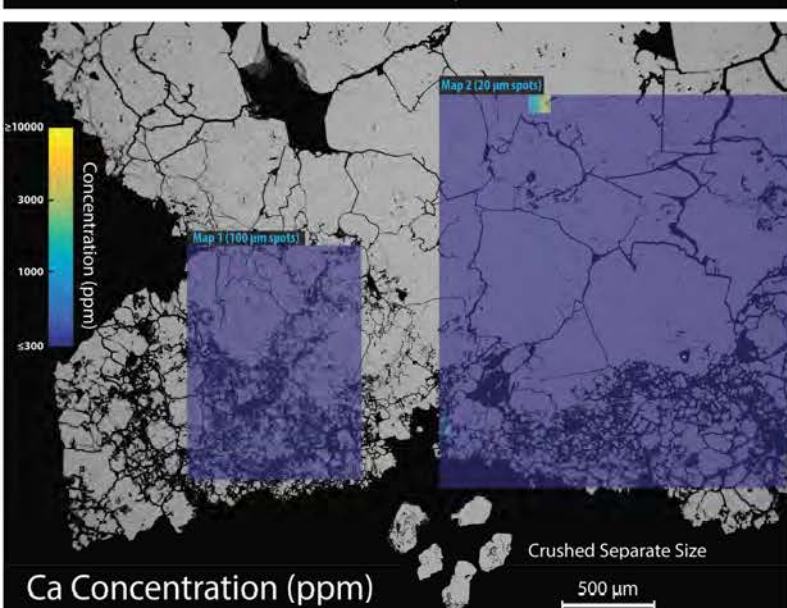
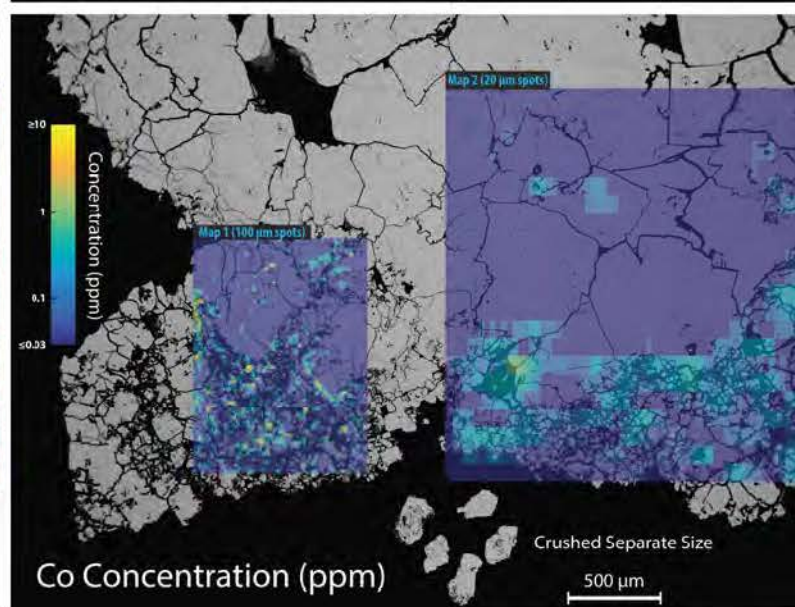
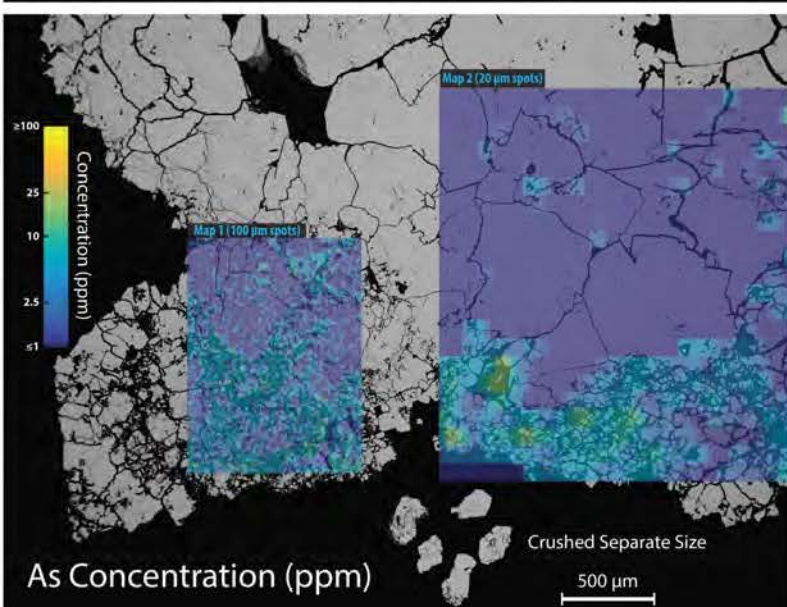
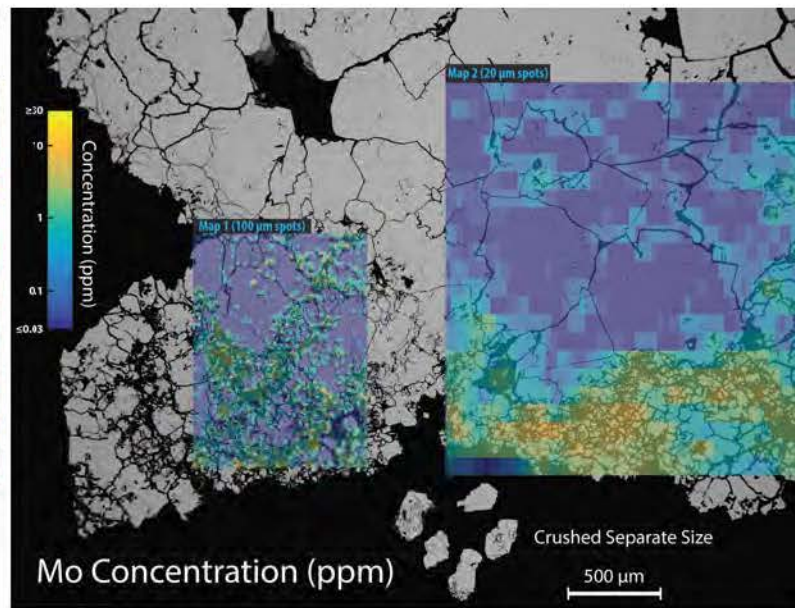
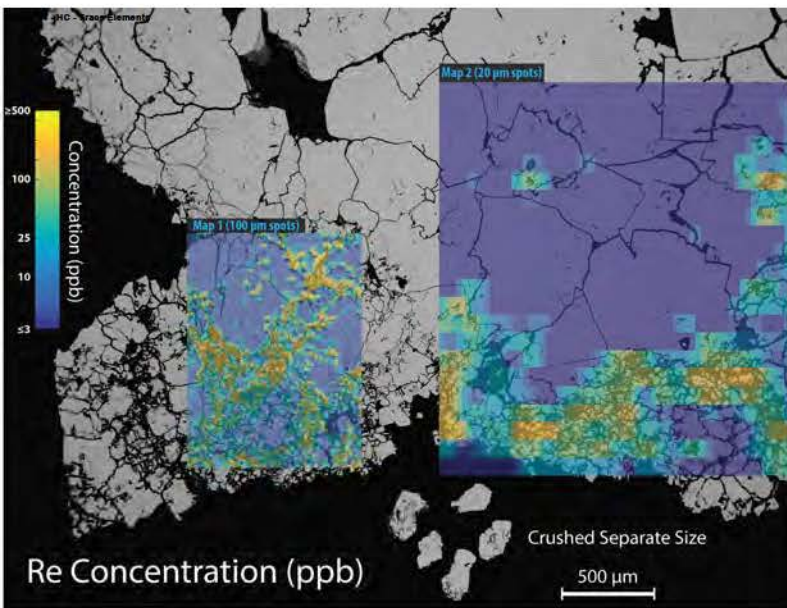
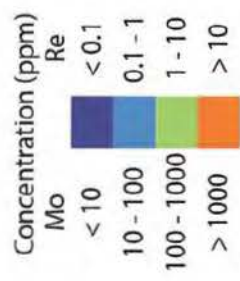
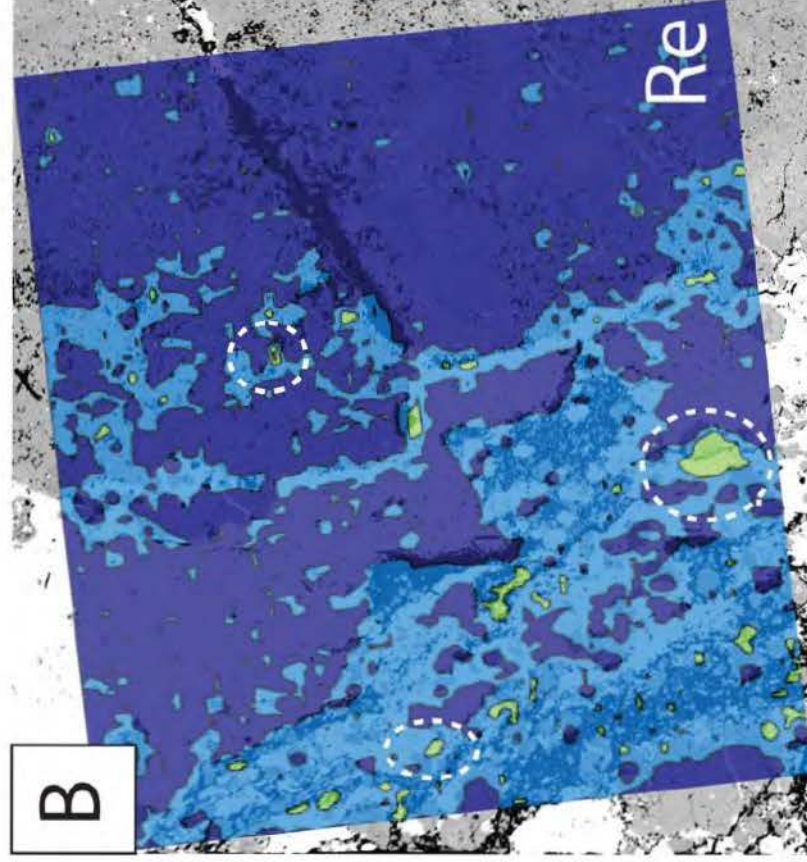
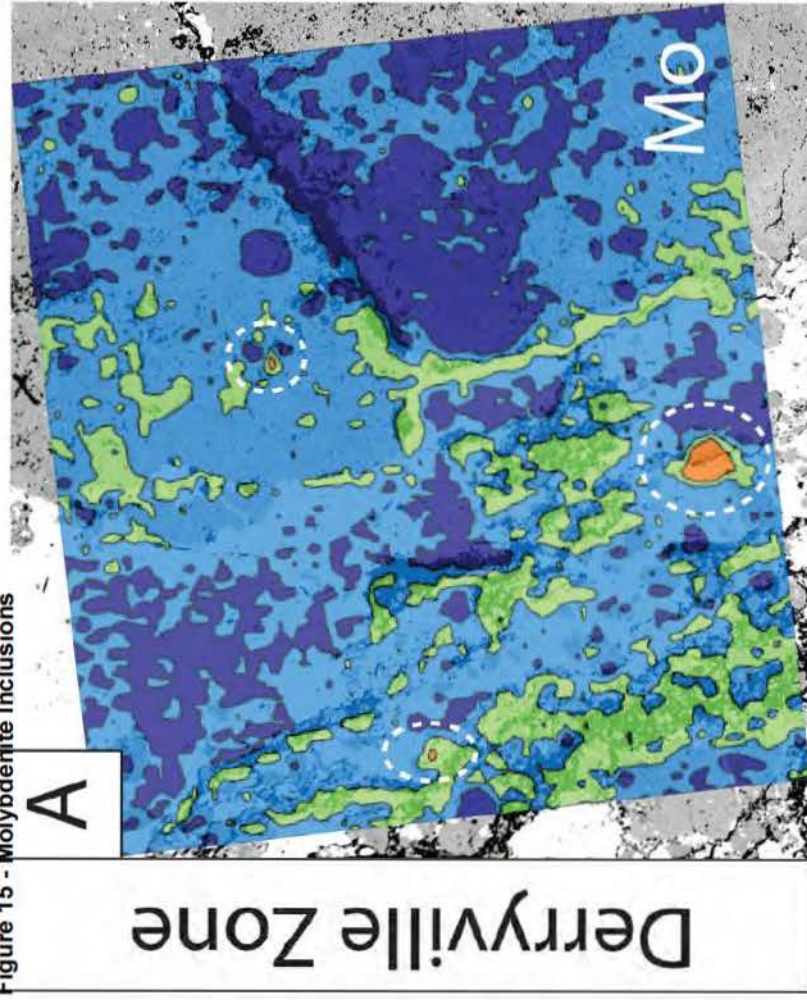


Figure 15 - Molybdenite Inclusions



Possible
Molybdenite
Inclusions

500 μ m

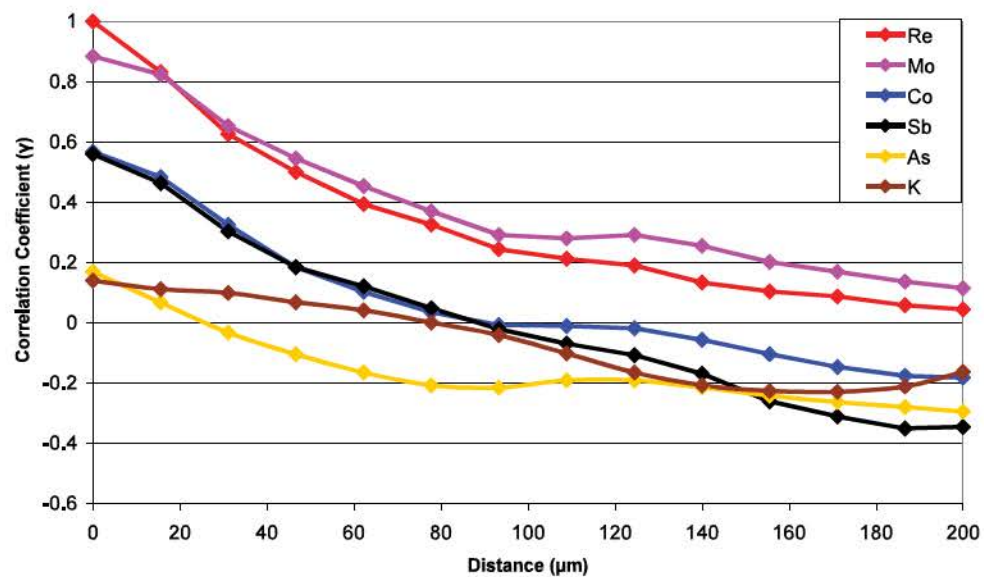
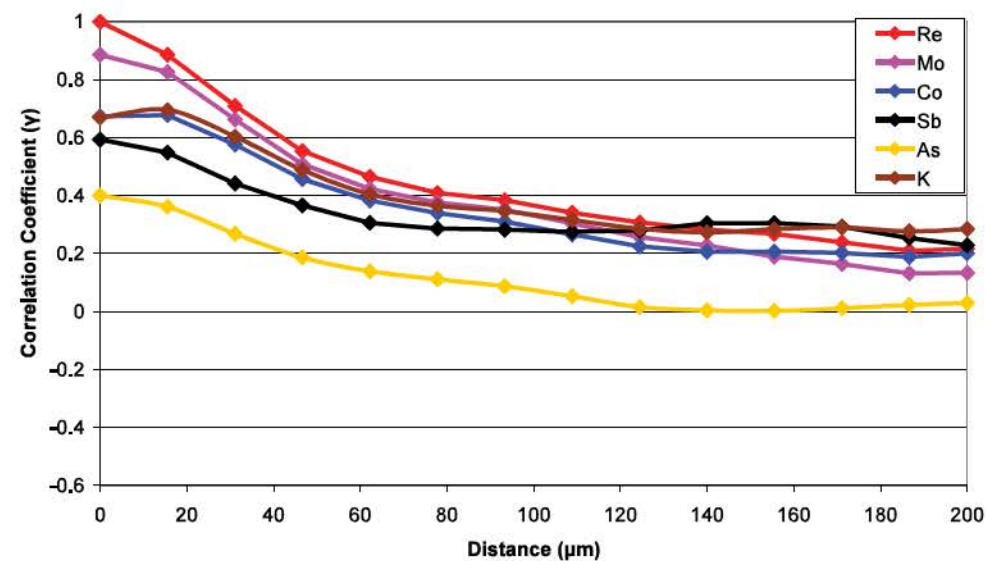
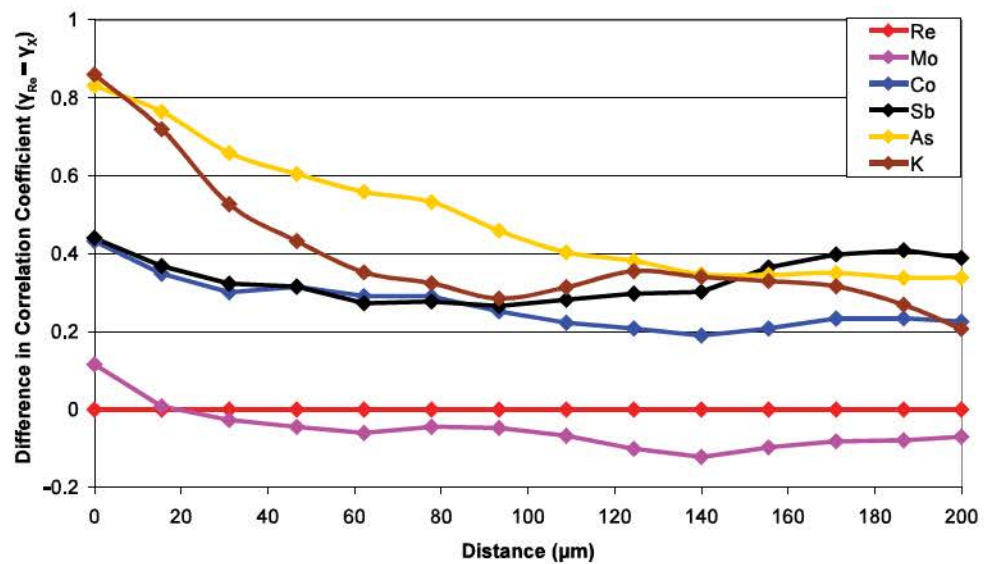
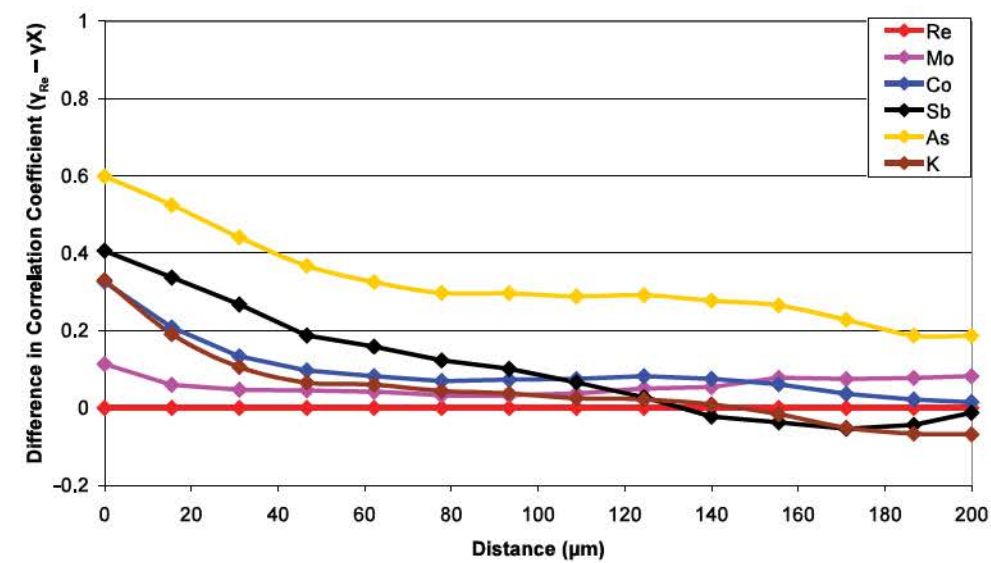
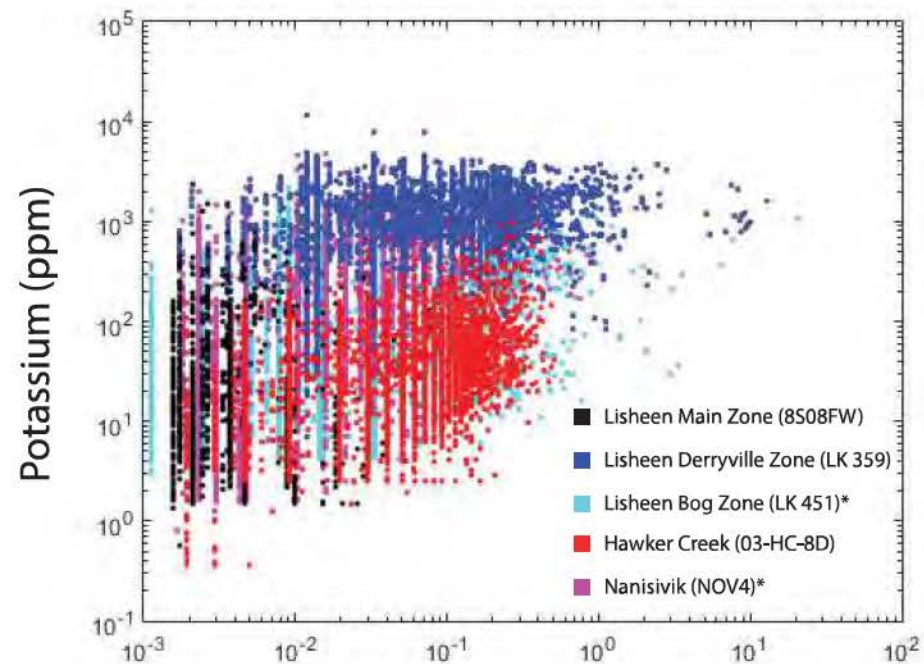
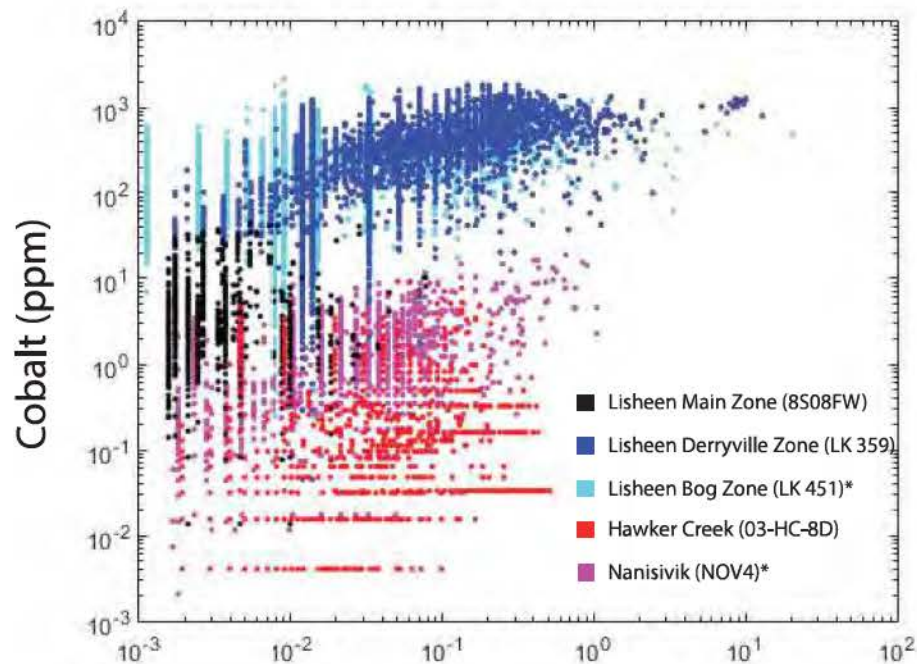
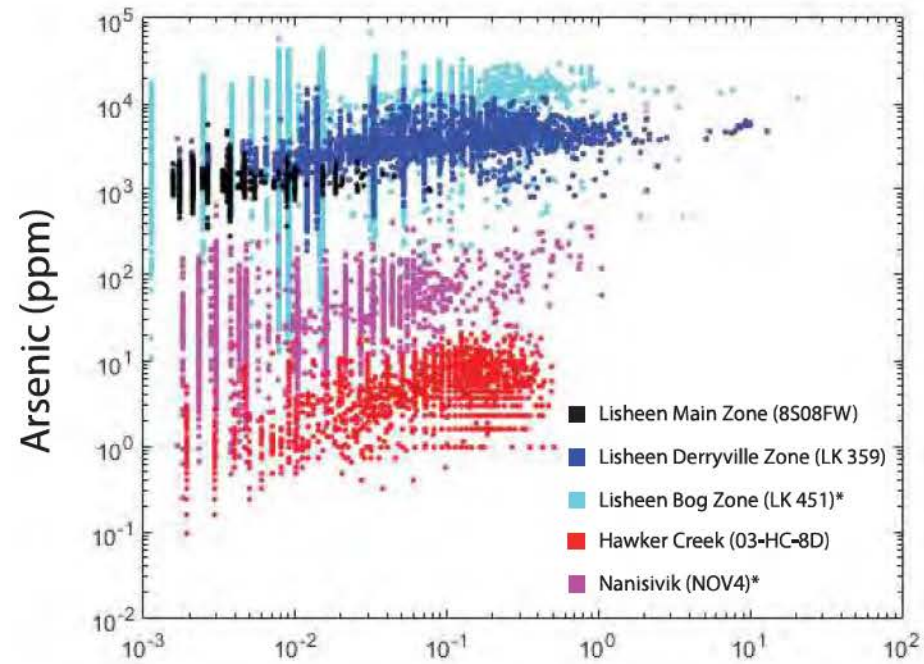
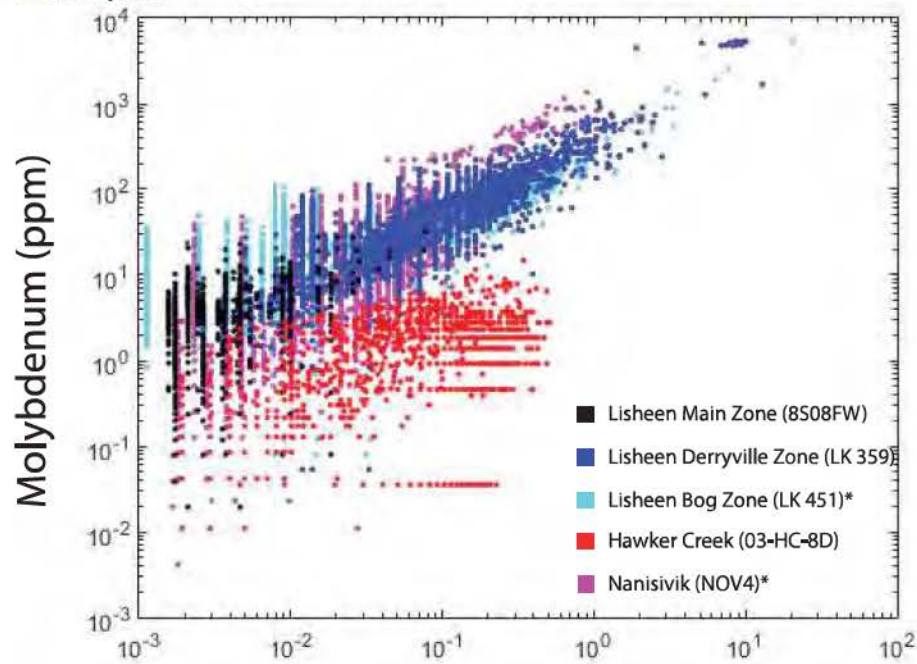
A**Correlogram for Pyrite****Correlogram for Sphalerite****B****Normalized Correlogram for Pyrite****Normalized Correlogram for Sphalerite**

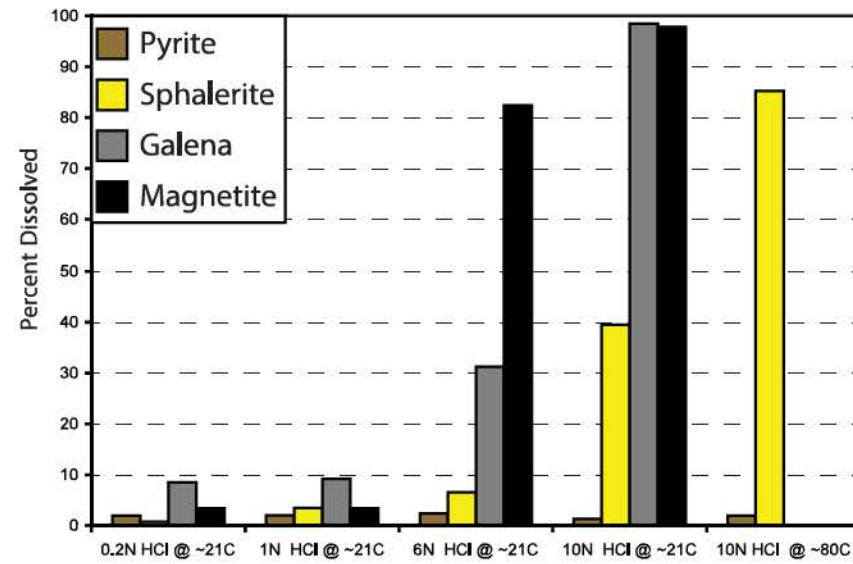
Figure 17- Scatterplots



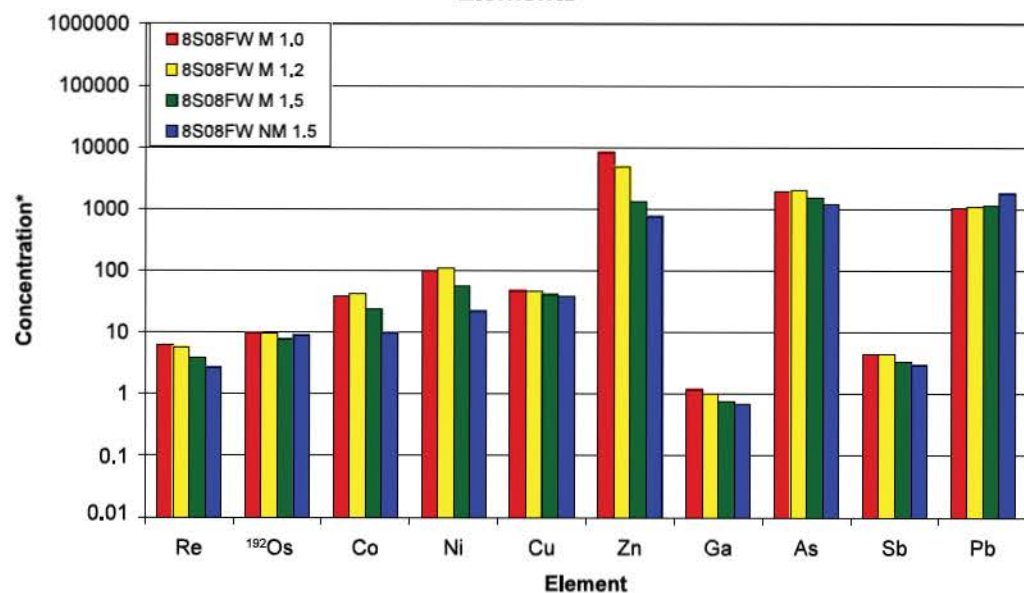
Rhenium (ppm)

Rhenium (ppm)

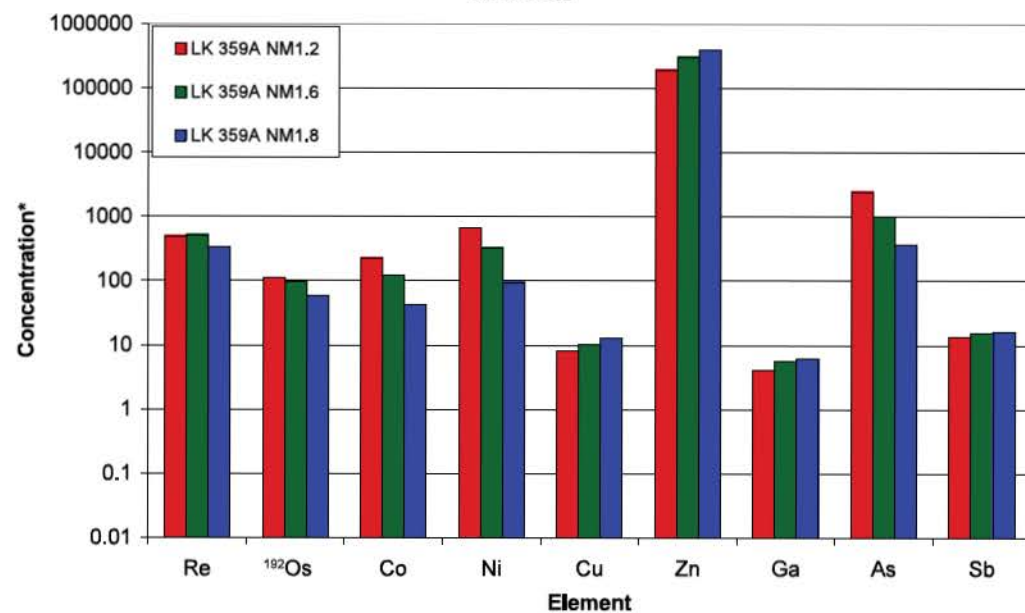
Figure A1- Leaching Experiment Composition
Leaching Experiments on Select Minerals



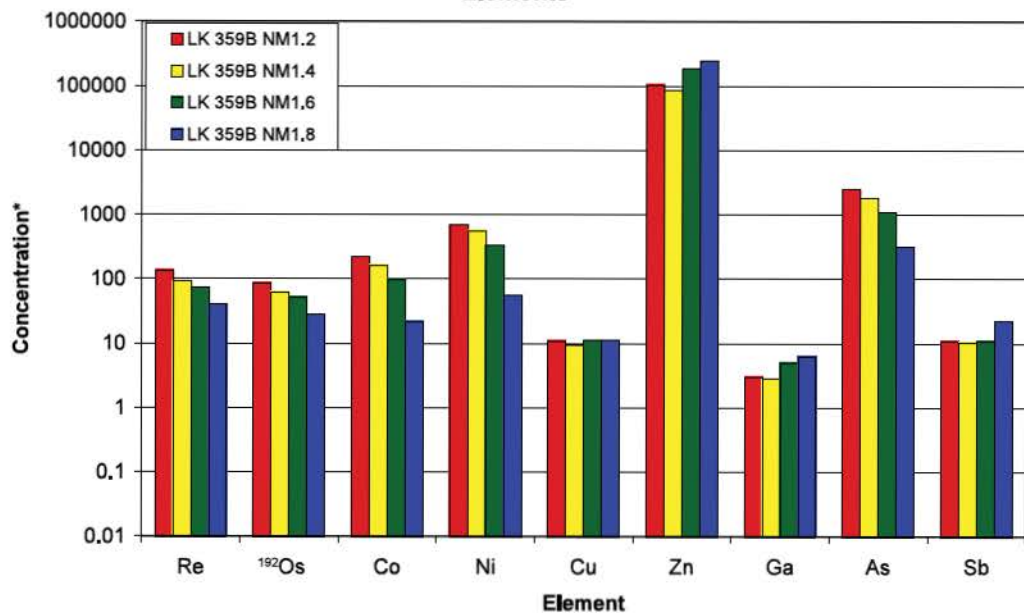
A Lisheen Main Zone (8S08FW) Siderophile and Chalcophile Elements



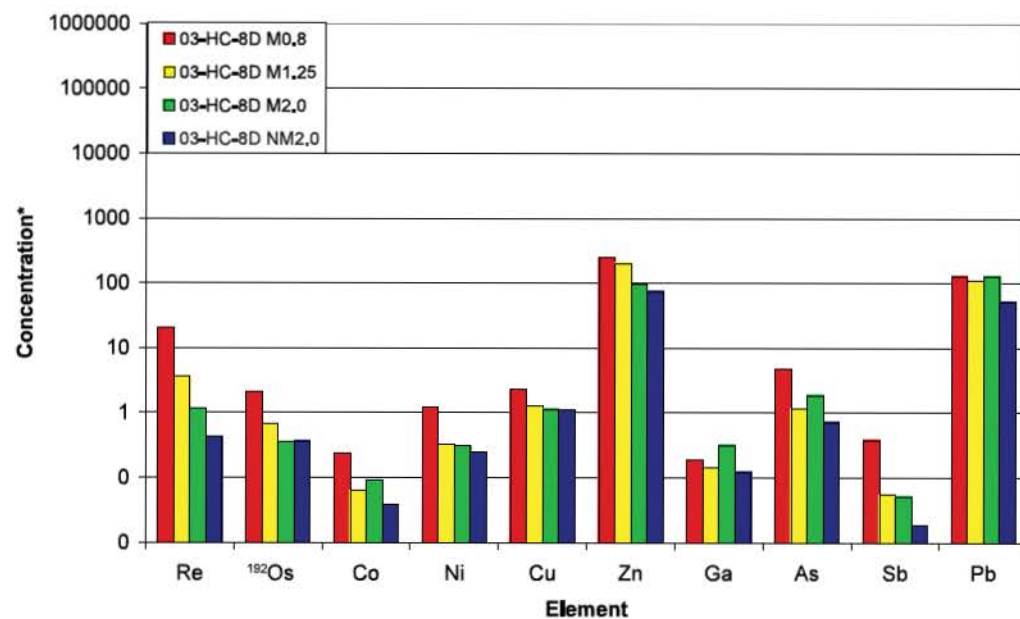
B Lisheen Derryville Zone (LK 359A) Siderophile and Chalcophile Elements



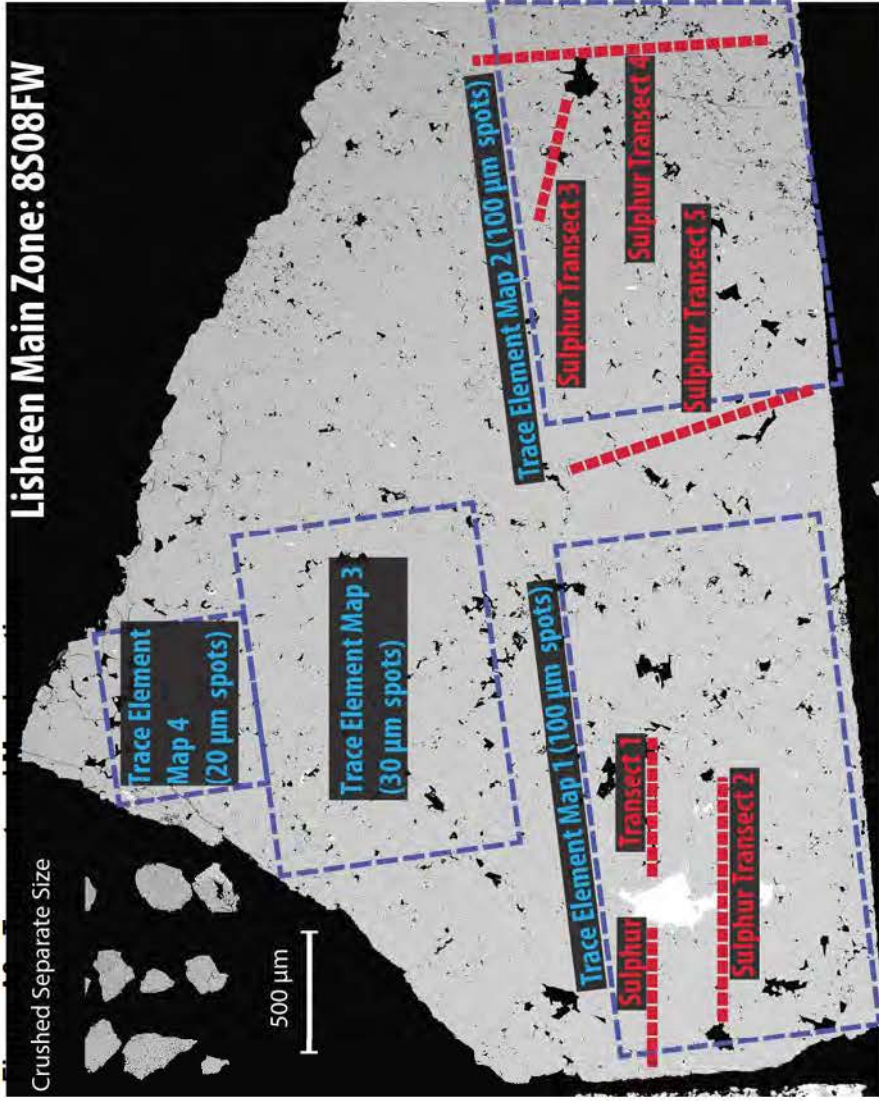
C Lisheen Derryville Zone (LK 359B) Siderophile and Chalcophile Elements



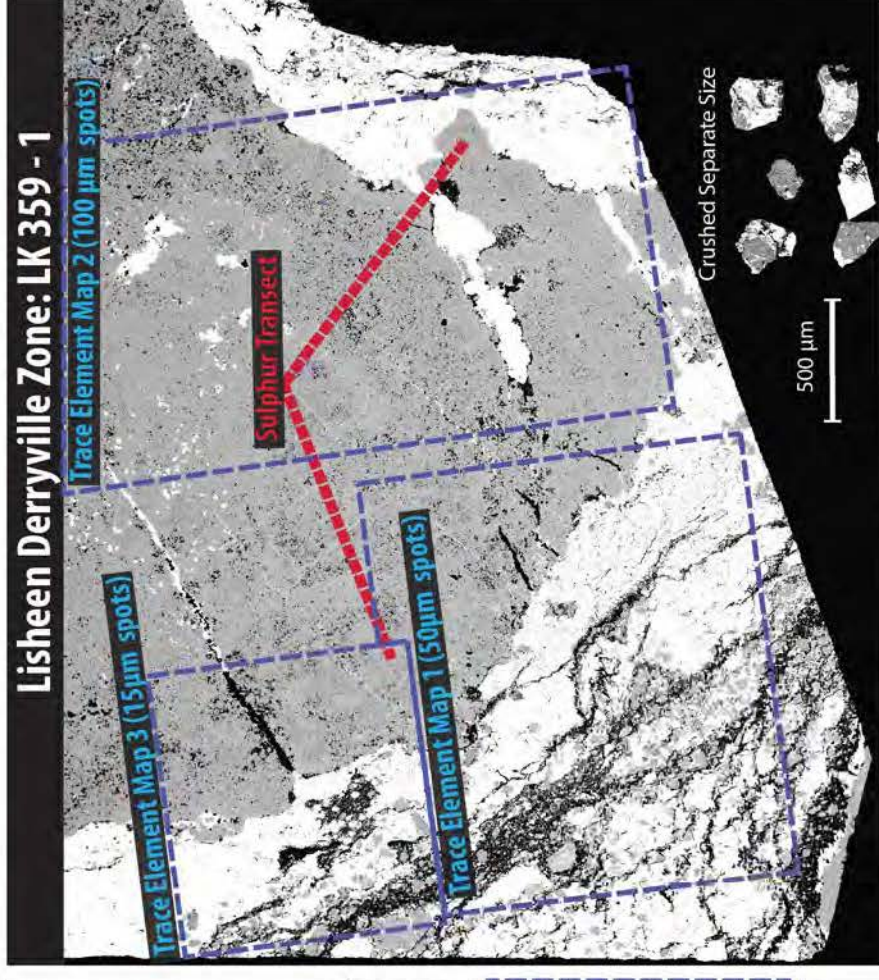
D Hawker Creek (03-HC-8D) Siderophile and Chalcophile Elements



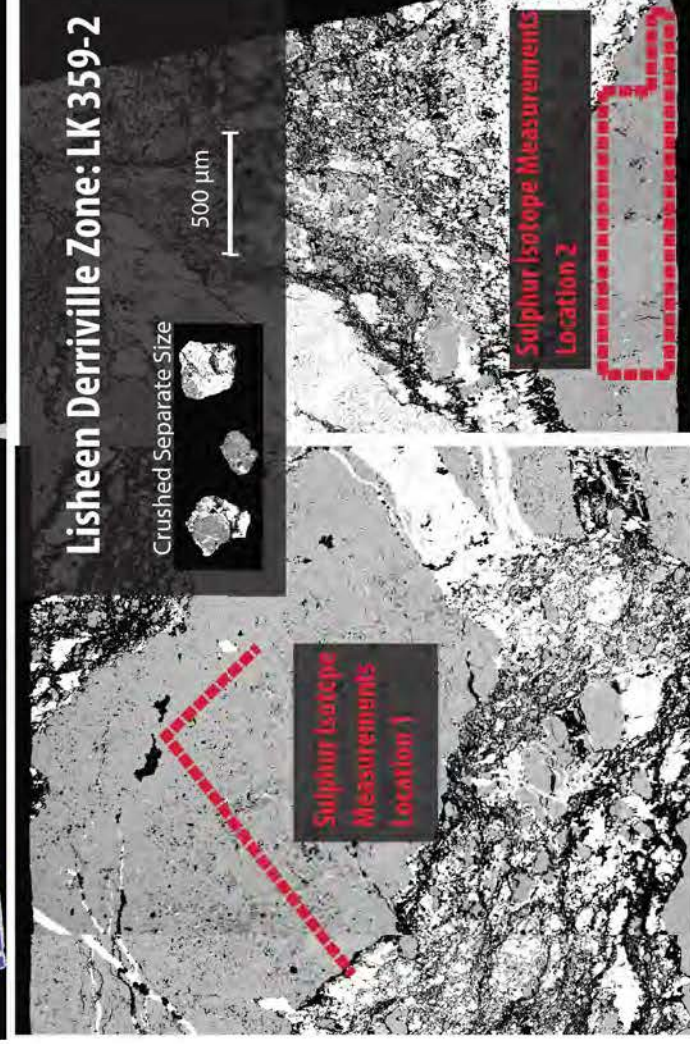
Lisheen Main Zone: 8S08FW



Lisheen Derryville Zone: LK 359 - 1



Lisheen Derryville Zone: LK 359-2



Hawker Creek: HC

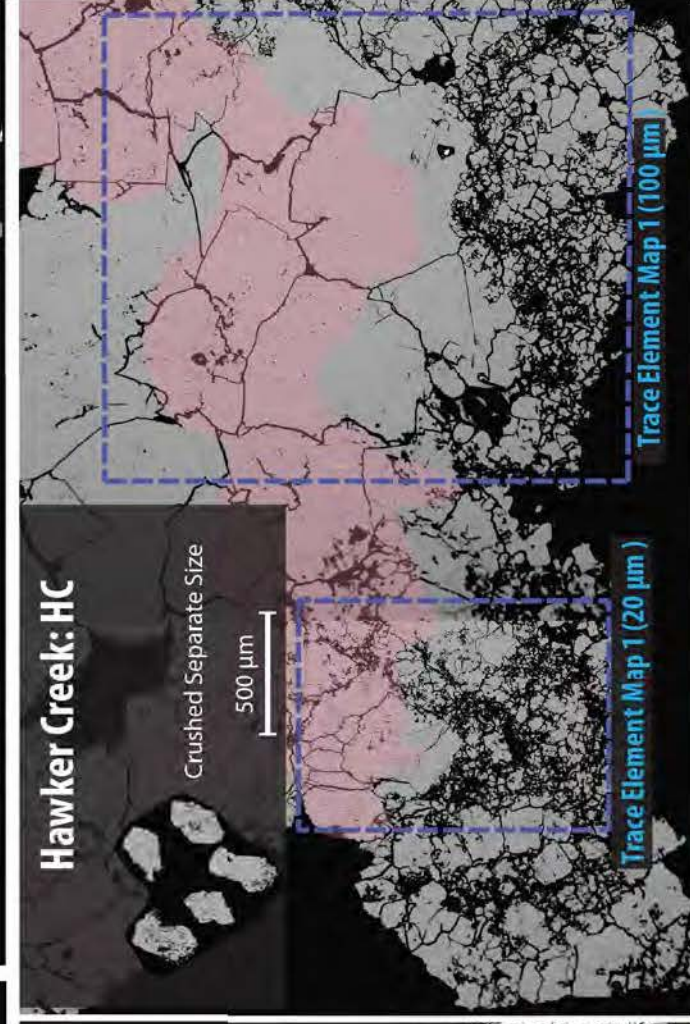
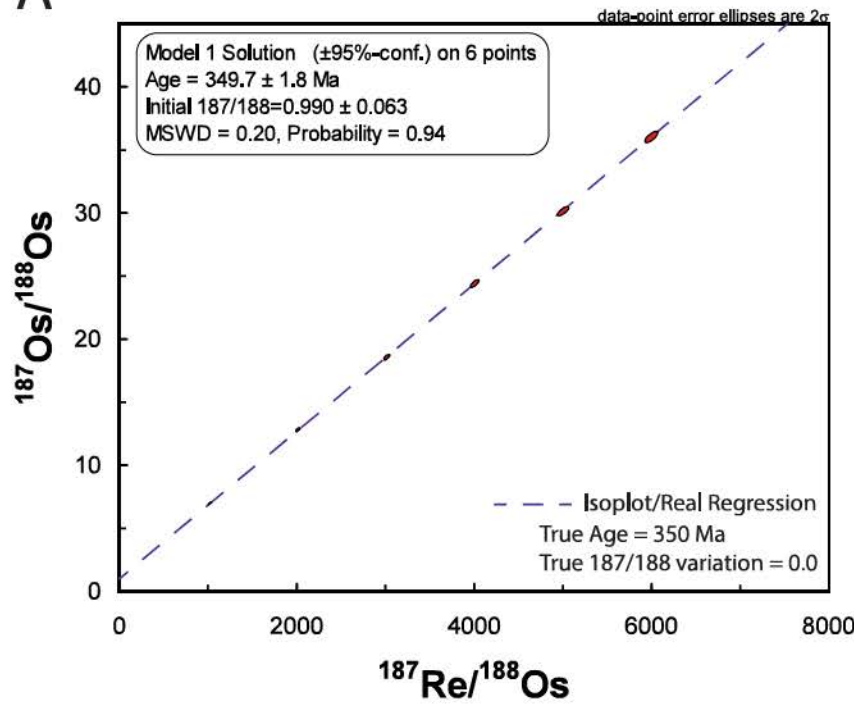
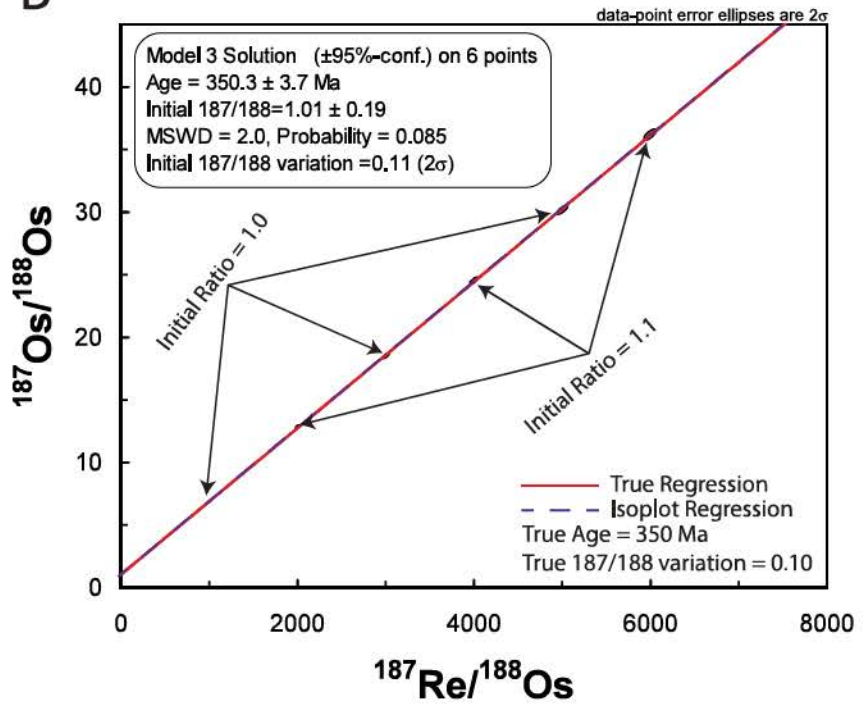


Figure A4 - Hypothetical Isochron

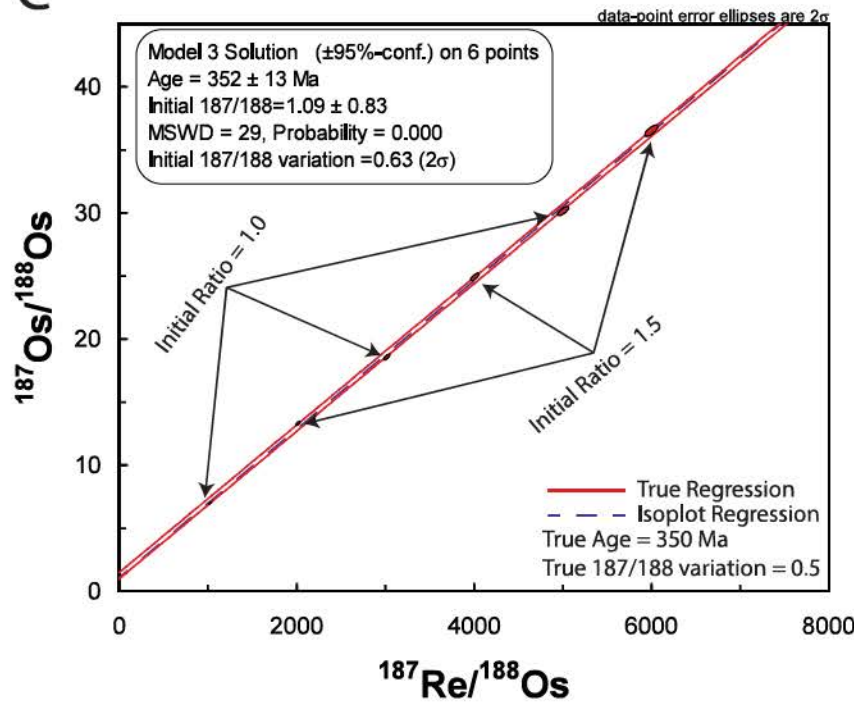
A



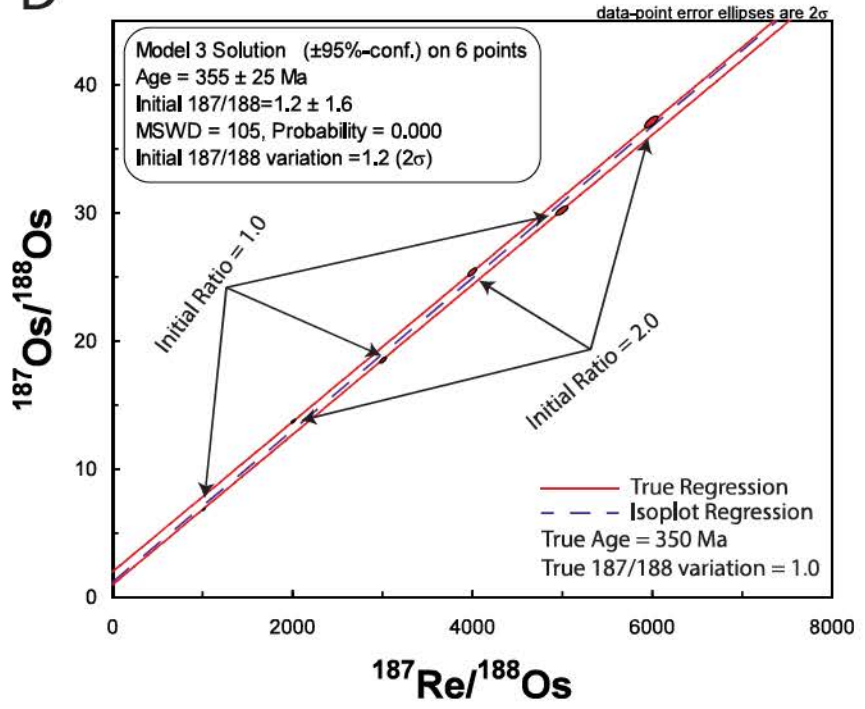
B



C



D



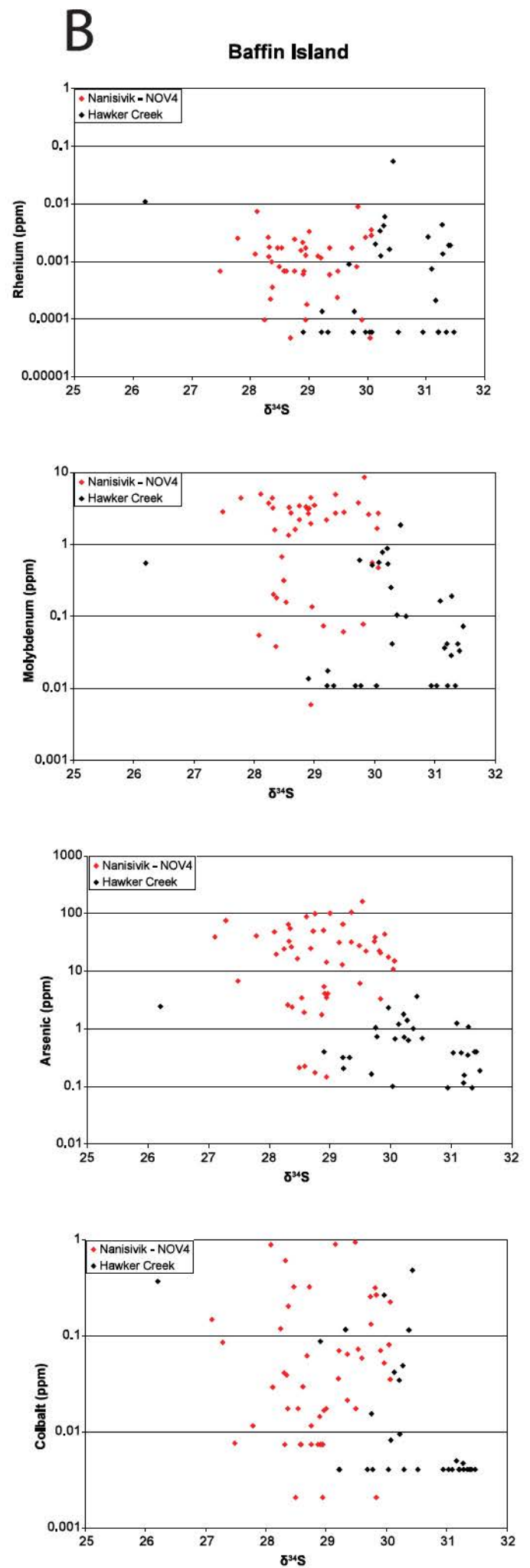
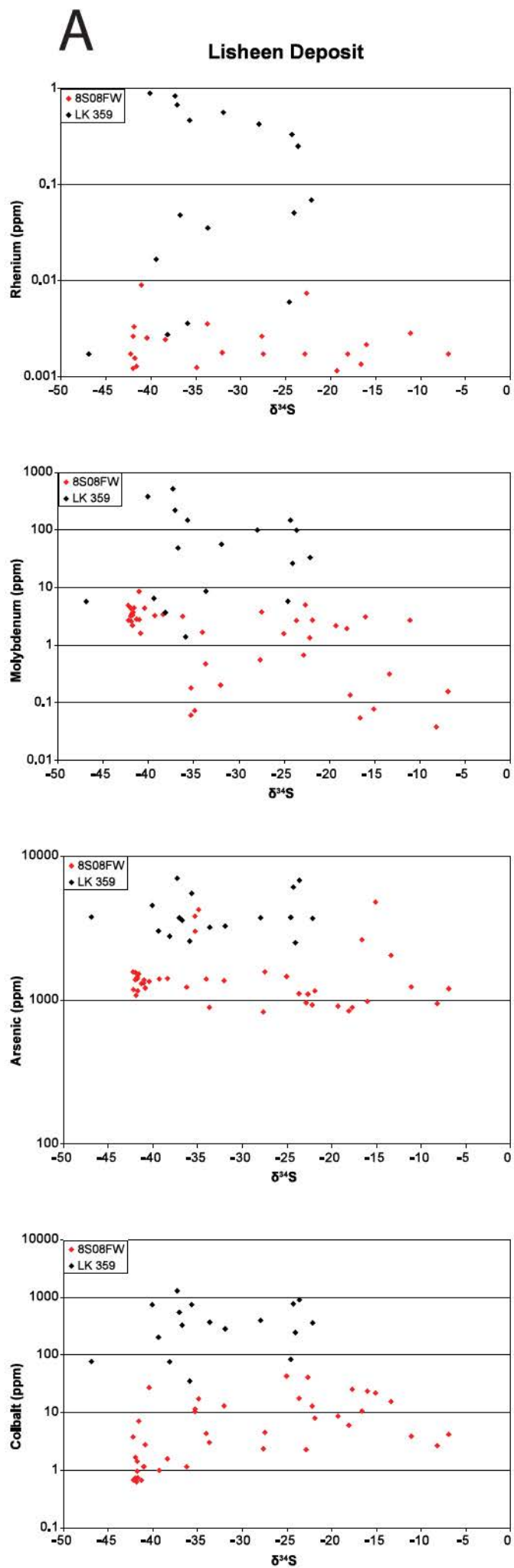


Figure A6 - Re vs. Mag

Increasing Magnetic Susceptibility

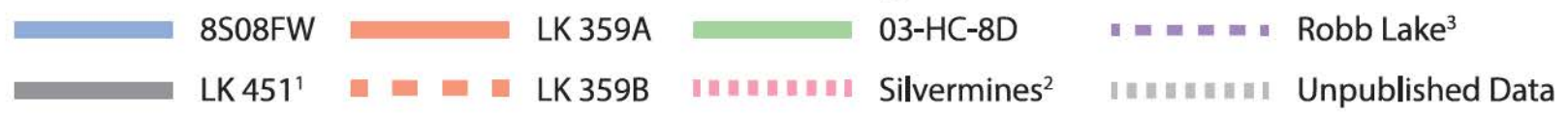
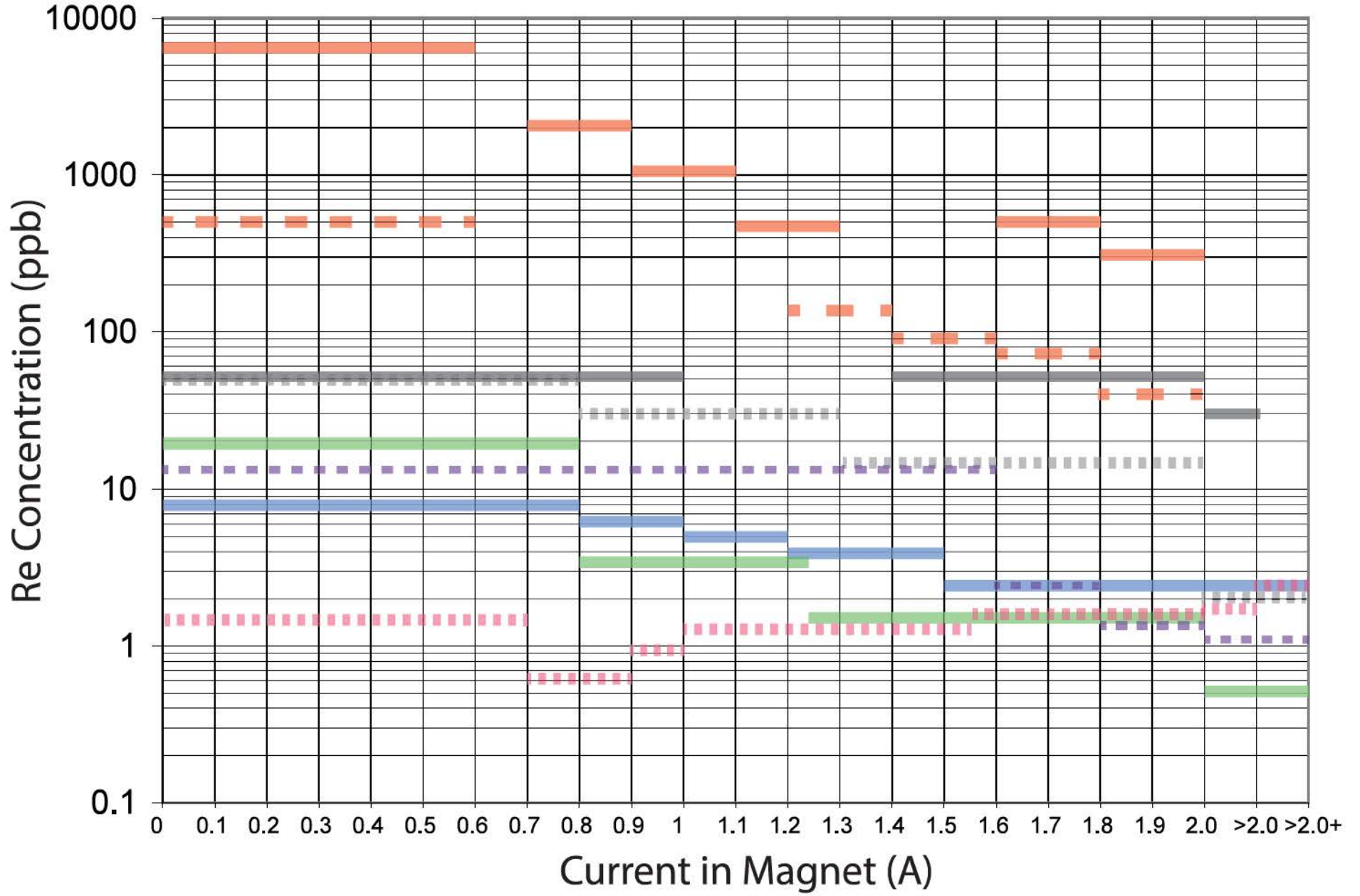
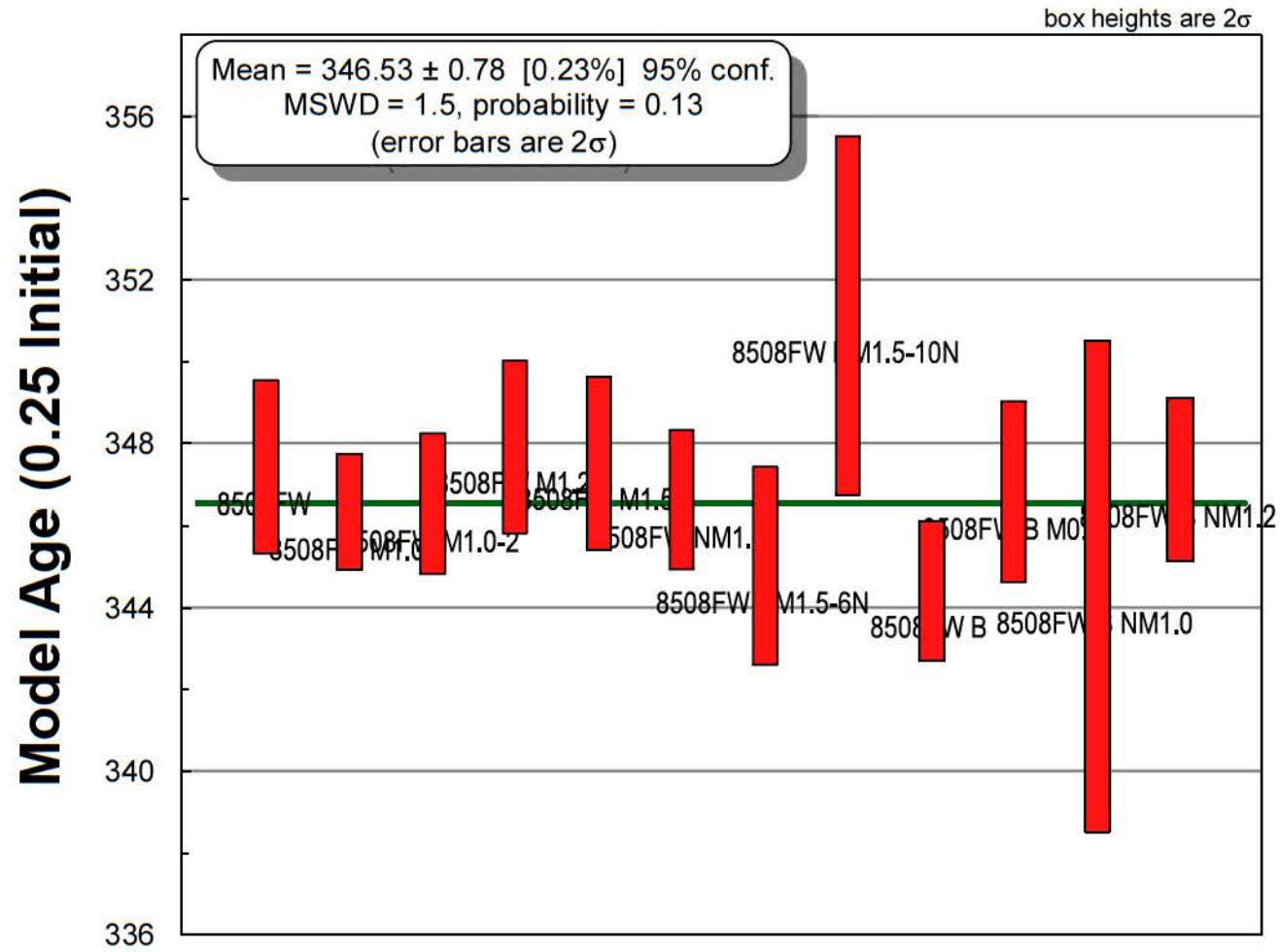


Table 1 - Mineral Separate Mineralogy

[Click here to download Table: Table 1 - Mineral Separate Mineralogy.xls](#)

Mineral Separate	Qualitative χ	Mineralogy (Modal Abundance)				
		Pyrite	Sphalerite	Galena	Silicates	Carbonate
8S08FW M1.0	4	83.2%	5.4%	0.1%	2.1%	9.1%
8S08FW M1.2	3	XX	X	X	X	X
8S08FW M1.5	2	XX	X	X	X	X
8S08FW NM1.5	1	94.3%	0.4%	<0.1%	3.0%	2.3%
8S08FW B M0.8	3	81.2%	8.8%	X	X	(10%)
8S08FW B NM1.0	2	XX	X	X	X	X
8S08FW B NM1.2	1	XX	X	X	X	X
LK 359A M0.6	6	XX	XX	X	X	X
LK 359A NM 0.8	5	47.2%	47.3%	0.50%	X	X
LK 359A NM 1.0	4	39.6%	54.3%	0.30%	4.7%	1.2%
LK 359A M1.2	>3	XX	XX	X	X	X
LK 359A NM 1.2	3	XX	XX	X	X	X
LK 359A NM 1.6	2	XX	XX	X	X	X
LK 359A NM 1.8	1	9.0%	69.1%	19.0%	2.5%	0.4%
LK 359B M0.6	5	XX	XX	X	X	X
LK 359B NM 1.2	4	74.2%	24.1%	0.3%	0.9%	0.5%
LK 359B NM 1.4	3	XX	XX	X	X	X
LK 359B NM 1.6	2	81.1%	17.9%	X	X	X
LK 359B NM 1.8	1	4.3%	93.8%	1.6%	0.3%	<0.1%
03-HC-8D M0.8	5	XX	X	X	X	X
03-HC-8D M1.25	4	XX	X	X	X	X
03-HC-8D M1.25-2	3	XX	X	X	X	X
03-HC-8D M2.0	2	XX	X	X	X	X
03-HC-8D NM2.0	1	XX	X	X	X	X



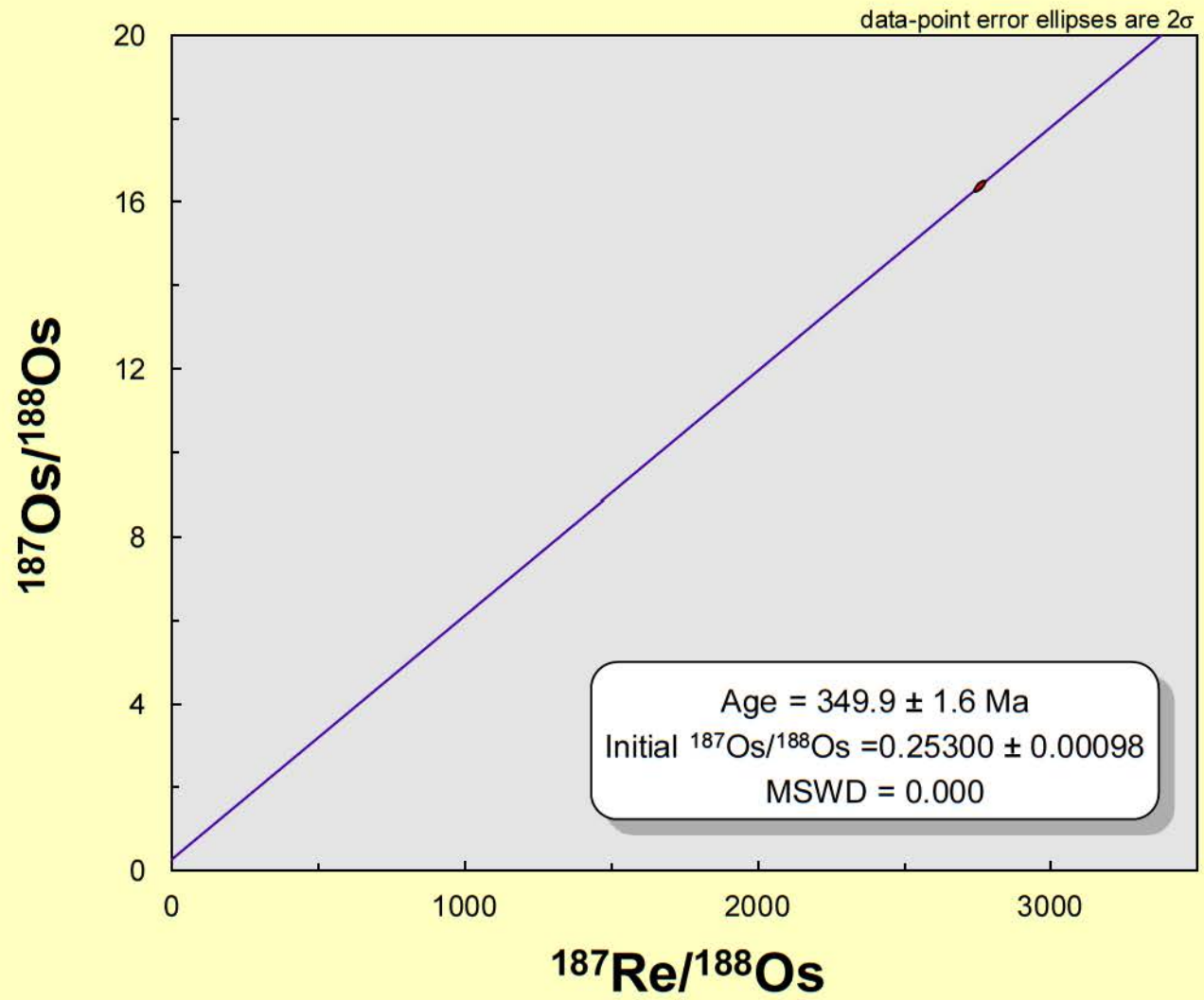


Table 4 - Re-Os for Baffin Island

[Click here to download Table: Table 4 - Re-Os for Baffin Island.xls](#)

Hawker Creek

Sample Name	Separation Procedure	Qualitative χ	Re ppb	Os ppt	$^{187}\text{Re} / ^{188}\text{Os}$	$\pm 2\sigma$
03-HC-8D M0.8	74-210 / Mag	4	20.34	93.69	19239.41	594.08
03-HC-8D M1.25	74-210 / Mag	3	3.62	22.85	10634.60	1005.87
03-HC-8D M1.25-2	74-210 / Mag	3	3.55	20.90	10327.38	973.47
03-HC-8D M2.0	74-210 / Mag	2	1.18	9.07	6478.95	1130.85
03-HC-8D M2.0-2	74-210 / Mag	2	1.60	12.12	9080.00	1648.17
03-HC-8D NM2.0	74-210 / Mag	1	0.44	4.65	2380.18	408.73
03-HC-8F M1.2	74-210 / Mag	2	8.37	88.47	8281.62	290.34
03-HC-8F NM1.2	74-210 / Mag	1	1.75	22.06	4509.50	381.59

* Data From Hnatyshin et al. (2016), refer to Hnatyshin et al. (2016) for blank corrections

Table A1 - Mineral Seperate ICPMS

[Click here to download Table: Table A1 - Mineral Seperate ICPMS.xls](#)

Analyte		Re	192Os	Li	Be	B
Detection Limits				0.3	0.1	2.0
Sample Name	Deposit	ppb	ppt	ppm	ppm	ppm
8S08FW M1.0	Lisheen - Main Zone	6.18	9.84	0.6	<DL	<DL
8S08FW M1.2	Lisheen - Main Zone	5.78	9.54	3.5	<DL	<DL
8S08FW M1.5	Lisheen - Main Zone	3.88	7.76	<DL	<DL	<DL
8S08FW NM1.5	Lisheen - Main Zone	2.73	8.91	0.5	<DL	<DL
LK 359A NM1.2	Lisheen - Derryville Zone	497.120	112.21	3.7	0.6	<DL
LK 359A NM1.6	Lisheen - Derryville Zone	519.679	97.16	5.5	0.6	<DL
LK 359A NM1.8	Lisheen - Derryville Zone	338.184	58.81	9.7	3.0	<DL
LK 359B NM1.2	Lisheen - Derryville Zone	137.032	87.13	2.4	0.3	<DL
LK 359B NM1.4	Lisheen - Derryville Zone	92.417	63.55	2.4	0.3	<DL
LK 359B NM1.6	Lisheen - Derryville Zone	73.437	52.31	4.3	1.1	<DL
LK 359B NM1.8	Lisheen - Derryville Zone	40.862	28.57	4.3	1.4	<DL
03-HC-8D M0.8	Hawker Creek	20.3	2.1	<DL	N/A	N/A
03-HC-8D M1.25	Hawker Creek	3.6	0.7	<DL	N/A	N/A
03-HC-8D M2.0	Hawker Creek	1.2	0.3	<DL	N/A	N/A
03-HC-8D NM2.0	Hawker Creek	0.4	0.1	<DL	N/A	N/A

Table A2 - 8S08FW Sulfur Isotopes

[Click here to download Table: Table A2 - 8S08FW Sulfur Isotopes.xls](#)

Name	Type	Session	$^{34}\text{S}/^{32}\text{S}$	1σ (%) intra- session	$\delta^{34}\text{S}$ (VCDT)	2σ (‰) inter- session
8S08FW M0.8	MS	1	0.04223708	0.00687	-43.60	0.14
8S08FW M0.8	MS	1	0.04232883	0.00659	-41.52	0.13
8S08FW M0.8	MS	1	0.04312045	0.00643	-23.60	0.13
8S08FW M0.8	MS	1	0.04234759	0.00702	-41.10	0.14
8S08FW M0.8	MS	1	0.04243688	0.00709	-39.08	0.14
8S08FW M0.8	MS	1	0.04241291	0.00713	-39.62	0.14
8S08FW M0.8	MS	1	0.04298212	0.00672	-26.73	0.13
8S08FW M0.8	MS	1	0.04256229	0.00668	-36.24	0.13
8S08FW M0.8	MS	1	0.04233773	0.00821	-41.32	0.16
8S08FW M0.8	MS	1	0.04250238	0.00644	-37.59	0.13
8S08FW M0.8	MS	1	0.04244052	0.01310	-38.99	0.26
8S08FW M0.8	MS	1	0.04344540	0.00717	-16.24	0.14
8S08FW M0.8	MS	1	0.04236389	0.00776	-40.73	0.16
8S08FW M0.8	MS	1	0.04342828	0.00834	-16.63	0.17
8S08FW M0.8	MS	1	0.04232621	0.00720	-41.58	0.14
8S08FW M0.8	MS	1	0.04233870	0.00655	-41.30	0.13
8S08FW M0.8	MS	1	0.04332298	0.01146	-19.01	0.23
8S08FW M0.8	MS	1	0.04333522	0.00573	-18.73	0.12
8S08FW M0.8	MS	1	0.04319016	0.00789	-22.02	0.16
8S08FW M0.8	MS	1	0.04336437	0.00697	-18.07	0.14
8S08FW M0.8	MS	1	0.04357137	0.00770	-13.39	0.15
8S08FW M0.8	MS	1	0.04301199	0.00746	-26.05	0.15
8S08FW M0.8	MS	1	0.04229405	0.00760	-42.31	0.15
8S08FW M0.8	MS	1	0.04335833	0.00594	-18.21	0.12
8S08FW M0.8	MS	1	0.04356498	0.00771	-13.53	0.15
8S08FW NM2.0	MS	1	0.04331996	0.00750	-19.08	0.15
8S08FW NM2.0	MS	1	0.04235396	0.00742	-40.95	0.15
8S08FW NM2.0	MS	1	0.04236496	0.00751	-40.70	0.15
8S08FW NM2.0	MS	1	0.04232130	0.00689	-41.69	0.14
8S08FW NM2.0	MS	1	0.04228204	0.00708	-42.58	0.14
8S08FW NM2.0	MS	1	0.04230218	0.00667	-42.13	0.13
8S08FW NM2.0	MS	1	0.04328041	0.00735	-19.97	0.15
8S08FW NM2.0	MS	1	0.04225457	0.00711	-43.20	0.14
8S08FW NM2.0	MS	1	0.04230801	0.00646	-41.99	0.13
8S08FW NM2.0	MS	1	0.04247885	0.00917	-38.13	0.18
8S08FW NM2.0	MS	1	0.04356880	0.01010	-13.44	0.20
8S08FW NM2.0	MS	1	0.04238436	0.00787	-40.26	0.16
8S08FW NM2.0	MS	1	0.04309481	0.00973	-24.18	0.19
8S08FW NM2.0	MS	1	0.04337386	0.01081	-17.86	0.22
8S08FW NM2.0	MS	1	0.04229901	0.00741	-42.20	0.15
8S08FW NM2.0	MS	1	0.04234783	0.00675	-41.09	0.14
8S08FW NM2.0	MS	1	0.04237418	0.00695	-40.50	0.14
8S08FW NM2.0	MS	1	0.04325964	0.00703	-20.45	0.14
8S08FW NM2.0	MS	1	0.04230793	0.00709	-42.00	0.14
8S08FW NM2.0	MS	1	0.04233280	0.00700	-41.43	0.14
8S08FW NM2.0	MS	1	0.04234041	0.00687	-41.26	0.14
8S08FW NM2.0	MS	1	0.04327751	0.00625	-20.04	0.13
8S08FW NM2.0	MS	1	0.04231157	0.00710	-41.91	0.14

Table A3 - LK359 Sulphur Isotopes

[Click here to download Table: Table A3 - LK359 Sulphur Isotopes.xlsx](#)

Name	Type	Session	$^{34}\text{S}/^{32}\text{S}$	1σ (%) intra- session	$\delta^{34}\text{S}$ (VCDT)	2σ (‰) inter- session
LK 359A NM0.8	MS	1	0.04211248	0.00919	-46.42	0.18
LK 359A NM0.8	MS	1	0.04180765	0.00955	-53.32	0.19
LK 359A NM0.8	MS	1	0.04196206	0.00653	-49.83	0.13
LK 359A NM0.8	MS	1	0.04205835	0.00727	-47.65	0.15
LK 359A NM0.8	MS	1	0.04275719	0.01517	-31.82	0.30
LK 359A NM0.8	MS	1	0.04277271	0.00981	-31.47	0.20
LK 359A NM0.8	MS	1	0.04294546	0.01765	-27.56	0.35
LK 359A NM0.8	MS	1	0.04295127	0.00752	-27.43	0.15
LK 359A NM0.8	MS	1	0.04338021	0.00772	-17.71	0.15
LK 359A NM0.8	MS	1	0.04391438	0.00742	-5.62	0.15
LK 359A NM0.8	MS	1	0.04359814	0.00697	-12.78	0.14
LK 359A NM0.8	MS	1	0.04355439	0.00665	-13.77	0.13
LK 359A NM0.8	MS	1	0.04310493	0.01441	-23.95	0.29
LK 359A NM0.8	MS	1	0.04405122	0.00688	-2.52	0.14
LK 359A NM0.8	MS	1	0.04406171	0.00673	-2.28	0.14
LK 359A NM0.8	MS	1	0.04294171	0.00586	-27.64	0.12
LK 359A NM0.8	MS	1	0.04276680	0.00694	-31.60	0.14
LK 359A NM0.8	MS	1	0.04202693	0.00617	-48.36	0.12
LK 359A NM0.8	MS	1	0.04342079	0.00606	-16.80	0.12
LK 359A NM0.8	MS	1	0.04320300	0.00744	-21.73	0.15
LK 359A NM0.8	MS	1	0.04315286	0.00725	-22.86	0.15
LK 359A NM0.8	MS	1	0.04200740	0.00772	-48.80	0.15
LK 359A NM0.8	MS	1	0.04199767	0.00686	-49.02	0.14
LK 359A NM0.8	MS	1	0.04206220	0.00604	-47.56	0.12
LK 359B NM1.6	MS	1	0.04193138	0.00681	-50.52	0.14
LK 359B NM1.6	MS	1	0.04204957	0.00711	-47.85	0.14
LK 359B NM1.6	MS	1	0.04204556	0.00619	-47.94	0.12
LK 359B NM1.6	MS	1	0.04193744	0.00724	-50.38	0.15
LK 359B NM1.6	MS	1	0.04209490	0.00719	-46.82	0.14
LK 359B NM1.6	MS	1	0.04267050	0.01058	-33.79	0.21
LK 359B NM1.6	MS	1	0.04218516	0.00800	-44.78	0.16
LK 359B NM1.6	MS	1	0.04201374	0.00806	-48.66	0.16
LK 359B NM1.6	MS	1	0.04209314	0.00672	-46.86	0.14
LK 359B NM1.6	MS	1	0.04192126	0.00612	-50.75	0.12
LK 359B NM1.6	MS	1	0.04200379	0.00722	-48.88	0.14
LK 359B NM1.6	MS	1	0.04201418	0.00638	-48.65	0.13
LK 359B NM1.6	MS	1	0.04310833	0.00929	-23.87	0.19
LK 359B NM1.6	MS	1	0.04205424	0.00660	-47.74	0.13
LK 359B NM1.6	MS	1	0.04204144	0.00627	-48.03	0.13
LK 359B NM1.6	MS	1	0.04194539	0.00641	-50.20	0.13
LK 359B NM1.6	MS	1	0.04221053	0.01085	-44.20	0.22
LK 359B NM1.6	MS	1	0.04218209	0.00627	-44.84	0.13
LK 359B NM1.6	MS	1	0.04217782	0.00708	-44.94	0.14
LK 359B NM1.6	MS	1	0.04262274	0.02541	-34.87	0.51
LK 359B NM1.6	MS	1	0.04210953	0.00581	-46.49	0.12
LK 359B NM1.6	MS	1	0.04223655	0.00708	-43.61	0.14
LK 359B NM1.6	MS	1	0.04264960	0.00835	-34.26	0.17
LK 359B NM1.6	MS	1	0.04303142	0.00995	-25.61	0.20

Table A4 - 8S08FW LA-ICPMS Map 1

[Click here to download Table: Table A4 - 8S08FW LA-ICPMS Map 1.xlsx](#)

x	y		Mg24	Al27	Si29	S34	K39	Ca43	Ti49
	0	200	0.005623	0.048369	12.93521	839.2142	0.328935	21.06325	0.235662
31.109		200	0.005623	0.048369	12.93521	839.2142	0.328935	21.06325	0.235662
62.218		200	0.005623	0.048369	12.93521	1389.433	0.328935	21.06325	0.235662
93.327		200	0.005623	0.048369	12.93521	1389.433	0.328935	21.06325	0.235662
124.436		200	0.005623	0.048369	26.44979	1364.579	0.328935	21.06325	0.235662
155.545		200	0.005623	0.048369	26.44979	1339.733	0.328935	21.06325	0.511232
186.654		200	0.005623	0.048369	12.93521	839.2142	0.328935	21.06325	0.511232
217.763		200	0.005623	0.048369	12.93521	839.2142	0.328935	21.06325	0.294941
248.872		200	0.005623	0.048369	12.93521	917.4649	0.328935	21.06325	0.235662
279.981		200	0.005623	0.048369	12.93521	917.4649	0.328935	21.06325	0.235662
311.09		200	0.005623	0.048369	12.93521	898.8399	0.328935	21.06325	0.235662
342.199		200	0.005623	0.048369	12.93521	886.4213	0.328935	21.06325	0.235662
373.308		200	0.005623	0.048369	12.93521	886.4213	0.630177	21.06325	0.235662
404.417		200	0.005623	0.048369	15.12558	1091.312	0.630177	21.06325	0.235662
435.526		200	0.005623	0.048369	15.12558	1811.946	0.780697	21.06325	0.511232
466.635		200	4.456493	74.96978	26.44979	51019.19	7.279665	265.2905	0.511232
497.744		200	9.733062	104.4906	62.04393	403423.6	14.87512	265.2905	3.106913
528.853		200	9.733062	104.4906	62.04393	565302.5	14.87512	63.31998	3.106913
559.962		200	4.385706	48.38293	50.7179	593261.8	14.87512	63.31998	3.106913
591.071		200	4.385706	35.06116	44.24608	603186.1	7.699077	44.08616	3.323221
622.18		200	4.385706	48.38293	31.3031	603186.1	3.022996	24.85311	3.539547
653.289		200	4.385706	56.18795	12.93521	561367.3	3.022996	21.06325	3.323221
684.398		200	6.651388	94.9702	31.3031	561367.3	8.991376	24.85311	2.890588
715.507		200	20.55273	103.6819	32.92096	561367.3	24.47435	3269.85	2.674279
746.616		200	50.12383	198.6744	173.719	550934.8	51.45468	7074.403	2.674279
777.725		200	50.12383	244.9206	173.719	550934.8	51.45468	7074.403	3.755872
808.834		200	30.57883	244.9206	52.33588	550934.8	22.05792	2961.358	3.755872
839.943		200	10.68986	347.7679	42.62823	541852	15.91904	2961.358	3.755872
871.052		200	10.68986	154.0388	52.33588	541852	15.91904	861.776	3.755872
902.161		200	16.68315	80.64399	24.83194	540953.4	16.32328	861.776	3.755872
933.27		200	18.1738	80.64399	102.4991	542903	18.44672	399.9557	3.755872
964.379		200	20.02003	99.7851	128.3944	561695.4	36.64761	149.8745	3.755872
995.488		200	20.02003	370.6528	139.7247	561695.4	36.64761	149.8745	3.755872
1026.597		200	15.51226	726.7421	207.7186	572974	37.5999	332.6212	5.053825
1057.706		200	15.1575	726.7421	227.1495	578630.5	37.5999	438.4341	3.755872
1088.815		200	15.51226	431.025	240.1043	578630.5	64.4672	448.0541	3.755872
1119.924		200	21.97356	431.025	240.1043	576354.4	71.88317	448.0541	3.755872
1151.033		200	21.97356	797.2799	304.8906	539714	77.93786	448.0541	3.539547
1182.142		200	20.2331	797.2799	379.4191	539714	141.9914	948.3866	3.539547
1213.251		200	15.86704	1033.535	638.8529	546707.6	141.9914	948.3866	4.621157
1244.36		200	15.86704	659.041	638.8529	546707.6	178.9447	226.8175	7.649921
1275.469		200	20.69479	484.7134	421.5557	557659.6	140.628	226.8175	9.164407
1306.578		200	32.53679	370.6218	421.5557	538064.7	160.2667	207.5813	7.649921
1337.687		200	33.42703	358.406	421.5557	561389.9	140.628	294.1466	9.164407
1368.796		200	33.42703	370.6218	262.7774	558507.9	93.32166	342.2404	7.649921
1399.905		200	23.00394	358.2825	144.5807	558507.9	64.39833	467.2941	3.755872

Table A5 - 8S08FW LA-ICPMS Map 2

[Click here to download Table: Table A5 - 8S08FW LA-ICPMS Map 2.xlsx](#)

x	y		Mg24	Al27	Si29	S34	K39	Ca43	Ti49
	0	200	0.012115	0.049538	16.48804	3532.084	0.304099	22.90519	0.212907
31.109		200	0.012115	0.049538	16.48804	4150.526	0.304099	22.90519	0.212907
62.218		200	0.012115	0.049538	16.48804	3532.084	0.304099	22.90519	0.212907
93.327		200	0.012115	0.049538	16.48804	2793.029	0.304099	22.90519	0.212907
124.436		200	0.012115	0.049538	16.48804	2793.029	0.304099	22.90519	0.212907
155.545		200	0.012115	0.049538	16.48804	2944.421	0.304099	22.90519	0.212907
186.654		200	0.012115	0.049538	16.48804	2944.421	0.304099	22.90519	0.212907
217.763		200	0.012115	0.049538	16.48804	2944.421	0.304099	22.90519	0.212907
248.872		200	0.012115	0.049538	16.48804	3301.813	0.304099	22.90519	0.212907
279.981		200	0.012115	0.049538	16.48804	3301.813	0.304099	22.90519	0.212907
311.09		200	0.012115	0.049538	16.48804	3410.884	0.304099	37.14183	0.212907
342.199		200	0.012115	0.049538	16.48804	3247.288	0.304099	37.14183	0.212907
373.308		200	0.012115	0.049538	16.48804	3247.288	0.304099	22.90519	0.212907
404.417		200	0.012115	0.049538	16.48804	3247.288	0.312252	22.90519	0.212907
435.526		200	0.012115	0.049538	16.48804	3241.23	0.312252	22.90519	0.212907
466.635		200	0.012115	0.049538	16.48804	3616.944	0.414653	22.90519	0.212907
497.744		200	1.514172	19.88585	16.48804	226684.4	1.507232	22.90519	0.496675
528.853		200	1.803087	62.22465	34.80706	301465.4	3.523081	22.90519	1.815502
559.962		200	2.850549	83.90936	44.78403	337606.4	7.132255	22.90519	3.134382
591.071		200	5.849735	187.8259	101.3285	367629.7	26.25029	22.90519	3.574021
622.18		200	5.849735	187.8259	101.3285	411484.2	26.25029	22.90519	3.134382
653.289		200	5.596719	111.0865	84.69626	428149.4	19.16508	27.31354	1.375881
684.398		200	4.65706	111.0865	74.71744	478029.5	8.896208	46.97012	1.375881
715.507		200	4.65706	189.7235	74.71744	478029.5	8.896208	27.31354	2.474934
746.616		200	10.00836	348.62	257.7336	478029.5	30.20777	66.6267	2.474934
777.725		200	10.00836	348.62	257.7336	493958.3	30.20777	22.90519	3.574021
808.834		200	5.560574	135.3378	56.4243	515200.3	20.42188	22.90519	2.474934
839.943		200	4.295705	88.10271	39.79541	534455.2	11.36466	22.90519	2.035313
871.052		200	2.489329	88.10271	38.13263	534455.2	7.234971	22.90519	2.035313
902.161		200	2.489329	112.415	38.13263	516462.5	6.601632	22.90519	3.134382
933.27		200	2.56157	210.6581	38.13263	516462.5	6.601632	22.90519	3.354193
964.379		200	4.295705	258.0169	31.4815	516462.5	5.985581	22.90519	3.134382
995.488		200	6.030469	258.0169	31.4815	518668.3	5.985581	22.90519	2.914554
1026.597		200	8.344473	147.1189	31.4815	518668.3	9.444516	56.79841	2.914554
1057.706		200	18.37274	147.1189	146.2419	518668.3	53.27906	56.79841	2.914554
1088.815		200	29.47548	277.166	359.2906	498913.2	135.1662	37.14183	5.772319
1119.924		200	62.31749	530.1784	814.3785	498913.2	355.9771	37.14183	14.78713
1151.033		200	132.3196	1213.921	1762.596	509726.8	640.1664	37.14183	17.64609
1182.142		200	180.733	1492.234	2108.118	509726.8	775.9894	37.14183	18.08596
1213.251		200	187.1849	1492.234	2108.118	509726.8	775.9894	22.90519	17.64609
1244.36		200	180.733	1083.658	1606.787	526174.9	566.9995	22.90519	12.80803
1275.469		200	133.2103	970.5306	1544.829	526174.9	519.7829	22.90519	9.729699
1306.578		200	81.37483	622.3274	974.6349	525205.8	334.1168	22.90519	5.992165
1337.687		200	67.33102	440.0681	712.6099	518440.2	222.723	22.90519	5.992165
1368.796		200	49.20468	364.2773	535.8789	523286.8	172.8139	22.90519	4.892989
1399.905		200	38.01965	332.9308	482.5541	523286.8	156.1151	22.90519	4.453316

Table A6 - 8S08FW LA-ICPMS Map 3

[Click here to download Table: Table A6 - 8S08FW LA-ICPMS Map 3.xlsx](#)

x	y	Mg24	Al27	Si29	S34	K39	Ca43	Ti49	
	0	40	0.076003	0.433558	112.5576	1926.233	2.186083	225.66	1.172329
6.2198		40	0.076003	0.433558	112.5576	2709.626	2.186083	225.66	1.172329
12.4396		40	0.076003	0.433558	112.5576	2709.626	2.186083	225.66	1.172329
18.6594		40	0.076003	0.433558	112.5576	2709.626	2.186083	225.66	1.172329
24.8792		40	0.076003	0.433558	112.5576	2108.084	2.186083	225.66	1.172329
31.099		40	0.076003	0.433558	112.5576	2108.084	2.186083	225.66	1.172329
37.3188		40	0.076003	0.433558	112.5576	2108.084	2.186083	225.66	1.172329
43.5386		40	0.076003	0.433558	112.5576	1926.233	2.186083	225.66	1.822143
49.7584		40	0.076003	0.433558	112.5576	2385.708	2.186083	225.66	1.822143
55.9782		40	0.076003	0.433558	112.5576	1926.233	2.186083	225.66	1.822143
62.198		40	0.076003	0.433558	112.5576	1926.233	2.186083	225.66	1.172329
68.4178		40	0.076003	0.433558	112.5576	1926.233	2.186083	225.66	1.172329
74.6376		40	0.076003	0.433558	112.5576	1926.233	2.326266	225.66	1.172329
80.8574		40	0.998396	2.861872	112.5576	294182.9	3.615697	225.66	1.172329
87.0772		40	1.671827	14.36403	112.5576	462849.5	3.615697	225.66	1.822143
93.297		40	1.671827	9.707942	112.5576	509907.9	2.487439	225.66	1.822143
99.5168		40	0.998396	9.981822	112.5576	528326.4	2.186083	225.66	1.172329
105.7366		40	0.998396	9.707942	112.5576	528326.4	2.186083	225.66	1.172329
111.9564		40	1.335125	1.21901	112.5576	528326.4	2.186083	225.66	1.172329
118.1762		40	1.335125	0.945196	112.5576	508350.3	2.186083	225.66	1.172329
124.396		40	0.998396	0.945196	112.5576	508350.3	2.186083	225.66	1.172329
130.6158		40	0.998396	6.147814	142.6656	502826.6	2.186083	225.66	1.822143
136.8356		40	1.335125	6.147814	142.6656	527721.7	2.186083	225.66	1.822143
143.0554		40	1.335125	7.243201	112.5576	578012.4	2.186083	225.66	1.822143
149.2752		40	0.324991	3.135686	112.5576	586653.8	2.186083	225.66	1.822143
155.495		40	0.324991	7.243201	112.5576	578012.4	3.293339	225.66	1.172329
161.7148		40	0.661693	452.7979	112.5576	565934.4	3.454525	225.66	1.172329
167.9346		40	0.661693	799.6237	112.5576	556359.5	3.293339	225.66	1.172329
174.1544		40	0.324991	452.7979	127.4883	556359.5	2.186083	225.66	1.172329
180.3742		40	0.324991	5.600142	112.5576	551552.2	2.186083	225.66	1.172329
186.594		40	0.998396	5.600142	112.5576	569129.3	2.186083	225.66	1.172329
192.8138		40	1.335125	2.861872	112.5576	569129.3	2.186083	225.66	1.172329
199.0336		40	1.335125	2.861872	112.5576	569129.3	2.186083	225.66	1.822143
205.2534		40	2.008557	0.433558	112.5576	537959.8	2.809796	225.66	1.172329
211.4732		40	1.671827	0.433558	112.5576	537959.8	3.293339	225.66	1.172329
217.693		40	2.008557	0.433558	112.5576	537959.8	3.293339	225.66	1.172329
223.9128		40	1.671827	0.433558	112.5576	549124.7	2.186083	225.66	1.172329
230.1326		40	2.345259	0.433558	112.5576	576945.8	2.186083	225.66	1.822143
236.3524		40	1.671827	0.433558	112.5576	576945.8	2.186083	225.66	1.822143
242.5722		40	1.671827	0.433558	112.5576	554385.5	2.186083	225.66	1.822143
248.792		40	1.671827	0.945196	112.5576	516292.9	2.186083	225.66	1.172329
255.0118		40	5.039121	1.492802	112.5576	516292.9	3.293339	1775.374	1.822143
261.2316		40	48.83699	6.969365	112.5576	486384.6	3.293339	8178.937	1.822143
267.4514		40	72.77564	6.969365	112.5576	486384.6	2.186083	10702.44	1.822143
273.6712		40	72.77564	5.873978	112.5576	486384.6	2.186083	10702.44	1.172329
279.891		40	38.72595	2.04043	112.5576	525555.2	2.186083	5947.02	1.172329

Table A7 - 8S08FW LA-ICPMS Map 4

[Click here to download Table: Table A7 - 8S08FW LA-ICPMS Map 4.xlsx](#)

x	y	Mg24	Al27	Si29	S34	K39	Ca43	Ti49	
	0	60	0.044272	0.222255	58.82614	33271.8	1.499086	116.2541	0.316848
	9.3327	60	0.044272	0.222255	58.82614	33383.67	1.499086	116.2541	0.316848
	18.6654	60	0.044272	0.222255	58.82614	33271.8	1.499086	116.2541	0.316848
	27.9981	60	0.044272	0.222255	58.82614	32824.29	1.499086	116.2541	0.316848
	37.3308	60	0.044272	0.222255	58.82614	32824.29	1.499086	116.2541	0.316848
	46.6635	60	0.044272	0.222255	58.82614	33383.67	1.499086	116.2541	0.316848
	55.9962	60	0.044272	0.222255	58.82614	33383.67	1.499086	116.2541	0.316848
	65.3289	60	0.044272	0.222255	58.82614	35219.23	1.499086	116.2541	0.316848
	74.6616	60	0.044272	0.222255	58.82614	33473.19	1.499086	116.2541	0.316848
	83.9943	60	0.044272	0.222255	58.82614	35219.23	1.499086	116.2541	0.316848
	93.327	60	0.044272	0.222255	58.82614	34749.05	1.499086	116.2541	0.316848
	102.6597	60	0.044272	0.222255	58.82614	35891.08	1.499086	116.2541	0.316848
	111.9924	60	0.174919	4.109493	64.7021	152126.9	1.499086	116.2541	0.316848
	121.3251	60	0.909103	6.505248	64.7021	405634.2	1.910601	116.2541	2.426546
	130.6578	60	0.909103	13.09508	58.82614	471497.3	1.910601	116.2541	2.426546
	139.9905	60	0.725561	13.09508	58.82614	573185.1	1.499086	116.2541	2.426546
	149.3232	60	0.725561	8.601773	58.82614	578504.4	1.499086	116.2541	2.426546
	158.6559	60	0.725561	3.06144	58.82614	578504.4	1.499086	116.2541	2.426546
	167.9886	60	0.358462	3.06144	58.82614	484347.8	1.499086	116.2541	1.188343
	177.3213	60	0.358462	6.954482	58.82614	471859.6	1.499086	116.2541	0.316848
	186.654	60	0.542004	18.93793	58.82614	471859.6	3.954638	116.2541	1.188343
	195.9867	60	1.459759	25.23215	58.82614	543443.5	4.221274	116.2541	2.426546
	205.3194	60	3.47893	25.23215	58.82614	549469.3	3.954638	116.2541	3.66475
	214.6521	60	3.47893	5.157606	58.82614	543443.5	2.888139	116.2541	2.426546
	223.9848	60	7.334183	2.163152	58.82614	538602.4	2.354925	128.8104	2.426546
	233.3175	60	7.334183	2.163152	58.82614	538602.4	2.354925	128.8104	2.426546
	242.6502	60	4.763946	1.115207	58.82614	559478.5	1.499086	128.8104	2.426546
	251.9829	60	1.459759	1.115207	58.82614	559478.5	1.499086	128.8104	2.426546
	261.3156	60	0.542004	28.52993	58.82614	561309.3	1.499086	116.2541	2.426546
	270.6483	60	1.459759	28.52993	58.82614	533346.3	1.499086	116.2541	3.66475
	279.981	60	2.193987	5.307335	58.82614	526284.1	1.499086	116.2541	3.66475
	289.3137	60	3.662501	5.307335	64.7021	526284.1	1.499086	116.2541	3.66475
	298.6464	60	4.396788	24.18297	114.4852	540936.3	17.47212	116.2541	3.66475
	307.9791	60	17.43418	206.8281	131.0801	561521	122.5008	116.2541	3.66475
	317.3118	60	60.63622	503.0997	753.5703	601244.3	296.4603	116.2541	4.903052
	326.6445	60	60.63622	503.0997	753.5703	608257.1	296.4603	116.2541	4.903052
	335.9772	60	34.15433	299.0151	512.8319	608257.1	123.758	116.2541	4.903052
	345.3099	60	11.19004	74.60655	180.8658	586479.3	37.68883	116.2541	4.903052
	354.6426	60	1.276202	14.59309	58.82614	507299.4	5.554565	116.2541	1.188343
	363.9753	60	1.276202	1.863731	58.82614	507299.4	1.499086	116.2541	1.188343
	373.308	60	0.542004	1.863731	58.82614	528131.4	1.499086	116.2541	1.188343
	382.6407	60	0.542004	1.863731	58.82614	528131.4	1.499086	116.2541	1.188343
	391.9734	60	0.542004	1.564321	58.82614	492765.8	1.499086	116.2541	1.188343
	401.3061	60	0.542004	0.666105	64.7021	492765.8	1.499086	116.2541	1.188343
	410.6388	60	0.909103	0.5164	64.7021	514361.6	1.499086	116.2541	1.188343
	419.9715	60	0.909103	0.5164	58.82614	563291.4	1.499086	116.2541	1.188343

Table A8 - LK359 LA-ICPMS Map 1

[Click here to download Table: Table A8 - LK359 LA-ICPMS Map 1.xlsx](#)

x	y		Mg24	Al27	Si29	S34	K39	Ca43	Ti49
	0	100	0.049514	0.15053	50.32142	1085.296	0.869359	87.29622	0.51633
15.5545		100	0.049514	0.15053	50.32142	1085.296	0.869359	87.29622	0.51633
31.109		100	0.049514	0.15053	43.73931	1085.296	0.869359	87.29622	0.51633
46.6635		100	0.049514	0.15053	43.73931	1085.296	0.869359	87.29622	0.51633
62.218		100	0.049514	0.15053	43.73931	1085.296	0.869359	87.29622	0.51633
77.7725		100	0.049514	0.15053	43.73931	1085.296	1.011203	87.29622	0.51633
93.327		100	0.049514	0.15053	43.73931	1085.296	1.011203	87.29622	0.51633
108.8815		100	0.049514	0.15053	43.73931	1085.296	0.869359	87.29622	0.51633
124.436		100	0.049514	0.15053	43.73931	1085.296	0.869359	166.6374	0.51633
139.9905		100	0.049514	0.15053	43.73931	1085.296	0.869359	166.6374	0.51633
155.545		100	0.049514	0.15053	43.73931	1085.296	0.869359	87.29622	0.51633
171.0995		100	0.049514	0.15053	43.73931	1085.296	0.869359	87.29622	0.51633
186.654		100	0.049514	0.15053	43.73931	1085.296	0.869359	87.29622	0.51633
202.2085		100	0.049514	0.15053	43.73931	1085.296	1.060664	87.29622	0.51633
217.763		100	43.79874	879.8949	2157.198	39294.12	1045.898	87.29622	110.8419
233.3175		100	721.0604	8806.583	11846.75	237866.1	4404.337	1031.061	504.3566
248.872		100	745.0986	8834.153	11846.75	339319.6	4404.337	1088.696	504.3566
264.4265		100	745.0986	8834.153	11247.32	356588.9	4251.022	1031.061	380.4983
279.981		100	691.7101	8022.861	10346.67	404032.3	3698.906	1002.243	380.4983
295.5355		100	542.5441	6150.83	7136.6	404032.3	2749.054	771.7119	282.5744
311.09		100	345.1095	3902.959	4674.546	404032.3	1743.848	656.4531	277.4237
326.6445		100	234.56	3107.421	4036.827	403880	1618.729	627.6379	200.8446
342.199		100	234.56	3107.421	4036.827	427069.4	1618.729	368.3189	200.8446
357.7535		100	293.087	3898.425	5178.186	421524.2	1931.332	368.3189	200.8446
373.308		100	386.7344	5121.504	6436.493	421524.2	2404.46	512.3814	334.7431
388.8625		100	629.6367	7974.959	15485.32	402515.2	4103.95	541.1967	635.5118
404.417		100	948.8465	12156.44	17622.24	353389.6	6048.241	1002.243	1208.416
419.9715		100	1009.578	13160.31	16261.12	331734.8	6048.241	1348.066	1208.416
435.526		100	1009.578	13160.31	16261.12	315977.4	6024.163	1348.066	919.8502
451.0805		100	739.1692	9666.275	11342.99	331734.8	4499.071	281.8824	876.3919
466.635		100	726.0883	8935.283	11342.99	358842.5	4227.678	281.8824	876.3919
482.1895		100	726.0883	8935.283	12855.45	360508.6	4227.678	570.0096	876.3919
497.744		100	804.8649	10529.61	13491.72	360508.6	5263.978	742.8966	803.1475
513.2985		100	912.3482	11571	14755.99	330750.8	5886.949	570.0096	803.1475
528.853		100	1148.828	14396.61	18426.02	322432.2	7073.215	829.3447	1171.314
544.4075		100	1148.828	14483.9	18426.02	317794.1	7073.215	570.0096	1209.718
559.962		100	1111.48	14396.61	18339.49	314680.5	6721.501	310.693	1209.718
575.5165		100	1036.499	13168.52	15870.57	314680.5	6395.38	224.2587	571.5236
591.071		100	1036.499	12981.49	15830.01	312487.3	6395.38	310.693	451.4363
606.6255		100	1036.499	12981.49	15830.01	312487.3	6395.38	397.1296	426.2786
622.18		100	664.2001	9183.549	11171.8	318653.1	4718.268	1722.742	316.7058
637.7345		100	614.9921	7905.339	9728.516	327139.2	3849.367	1722.742	217.5701
653.289		100	559.9865	7459.738	9035.662	357522.5	3542.389	1319.246	217.5701
668.8435		100	559.9865	7169.066	8865.073	404641.8	3488.75	627.6379	270.3419
684.398		100	589.2891	7157.077	8975.451	414247.2	3486.585	627.6379	270.3419
699.9525		100	597.2609	7157.077	8975.451	421595	3486.585	1751.565	258.1113

Table A9 - LK359 LA-ICPMS Map 2

[Click here to download Table: Table A9 - LK359 LA-ICPMS Map 2.xlsx](#)

x	y		Mg24	Al27	Si29	S34	K39	Ca43	Ti49
	0	200	0.007625	0.053091	17.9272	13471.48	0.361262	26.95585	0.127027
31.109		200	0.007625	0.053091	17.9272	13471.48	0.361262	26.95585	0.144012
62.218		200	0.007625	0.053091	17.9272	13758.26	0.361262	26.95585	0.144012
93.327		200	0.007625	0.053091	17.9272	13428.2	0.361262	26.95585	0.127027
124.436		200	0.007625	0.053091	17.9272	13428.2	0.361262	26.95585	0.127027
155.545		200	0.007625	0.053091	17.9272	13276.75	0.361262	29.90512	0.144012
186.654		200	0.007625	0.053091	17.9272	13276.75	0.361262	29.90512	0.144012
217.763		200	0.007625	0.053091	17.9272	13639.2	0.361262	26.95585	0.144012
248.872		200	0.007625	0.053091	17.9272	14061.39	0.361262	26.95585	0.144012
279.981		200	0.007625	0.053091	17.9272	14391.74	0.361262	26.95585	0.144012
311.09		200	0.007625	0.053091	17.9272	14061.39	0.361262	26.95585	0.144012
342.199		200	0.007625	0.053091	17.9272	13260.53	0.361262	26.95585	0.144012
373.308		200	0.007625	0.053091	17.9272	13260.53	0.361262	26.95585	0.144012
404.417		200	117.7437	1022.114	1475.516	300225.8	503.0845	122.0502	70.6274
435.526		200	192.5452	1618.728	2064.996	460618.6	742.4261	297.1458	92.03546
466.635		200	192.7947	1780.474	2261.337	514216.9	876.8364	370.8785	98.42004
497.744		200	199.8572	1780.474	2381.766	515282.8	876.8364	435.3977	98.42004
528.853		200	192.7947	1650.929	2435.665	523981.9	857.8937	527.5744	84.82891
559.962		200	199.8572	1560.906	2435.665	515282.8	829.7294	555.2283	68.98136
591.071		200	215.4832	1560.906	2489.578	523981.9	857.8937	1754.198	68.98136
622.18		200	225.7745	2022.184	2695.846	525071.6	1077.716	2418.758	92.8592
653.289		200	290.3731	2859.469	3661.684	525071.6	1634.727	2418.758	94.91862
684.398		200	372.598	4050.98	5029.799	524618.7	2290.338	859.4691	94.91862
715.507		200	414.3516	4997.793	5421.888	504411.7	2378.968	315.5788	69.80436
746.616		200	415.2488	5107.563	5853.393	504411.7	2378.968	315.5788	69.80436
777.725		200	415.2488	5107.563	5853.393	506631.9	2367.232	1634.247	94.71268
808.834		200	374.8585	4294.005	4911.034	512568.9	1956.589	3176.069	94.71268
839.943		200	221.648	2573.517	3532.54	506631.9	1110.211	3176.069	94.71268
871.052		200	155.2746	1631.473	1913.119	501513.2	756.4899	2557.256	52.73198
902.161		200	143.6233	1534.703	1913.119	482811.8	747.5006	2529.555	40.39736
933.27		200	137.4918	1522.964	1974.806	482811.8	739.5771	2529.555	52.73198
964.379		200	131.2981	1370.032	1974.806	488899	635.5709	1440.505	40.39736
995.488		200	128.4505	1142.915	1574.962	511046.1	597.3922	951.6783	40.8084
1026.597		200	131.2981	1142.915	1574.962	516512.3	597.3922	592.1024	40.8084
1057.706		200	159.1296	1514.973	1777.158	521017.4	739.1002	499.9205	86.27006
1088.815		200	206.2514	2155.057	2969.07	526728.2	1134.102	546.0103	123.9737
1119.924		200	243.2179	2431.277	3000.864	530027.6	1212.077	546.0103	540.3844
1151.033		200	243.2179	2431.277	2969.07	526728.2	1212.077	1348.259	624.0714
1182.142		200	243.2179	2457.631	3341.362	520754.4	1235.381	1661.927	624.0714
1213.251		200	293.3955	3121.806	3966.53	487342.6	1536.531	1661.927	258.3269
1244.36		200	318.8903	3992.71	4345.417	428436.3	1913.986	804.1466	107.6907
1275.469		200	390.192	4820.235	5577.964	351867.5	2118.018	804.1466	45.74165
1306.578		200	390.192	4820.235	5577.964	351867.5	2118.018	1477.406	45.74165
1337.687		200	325.9644	3927.559	4915.847	390929.5	1656.36	1477.406	52.32075
1368.796		200	152.7653	1933.433	2259.752	395722.6	945.362	767.2666	71.03893
1399.905		200	131.1223	1731.171	1984.298	395722.6	860.7101	601.3203	71.03893

Table A10 - LK359 LA-ICPMS Map 3

[Click here to download Table: Table A10 - LK359 LA-ICPMS Map 3.xlsx](#)

x	y	Mg24	Al27	Si29	S34	K39	Ca43	Ti49	
	0	30	0.122557	0.787496	227.3907	3430.058	5.028563	477.3417	1.675792
4.66635		30	0.122557	0.787496	227.3907	3430.058	5.028563	477.3417	1.675792
9.3327		30	0.122557	0.787496	227.3907	3430.058	5.028563	477.3417	1.675792
13.99905		30	0.122557	0.787496	227.3907	3430.058	5.028563	477.3417	1.675792
18.6654		30	0.122557	0.787496	227.3907	3430.058	5.028563	477.3417	1.675792
23.33175		30	0.122557	0.787496	227.3907	3430.058	5.028563	477.3417	1.675792
27.9981		30	0.122557	0.787496	227.3907	3430.058	5.028563	477.3417	1.675792
32.66445		30	0.122557	0.787496	227.3907	3430.058	5.028563	477.3417	1.675792
37.3308		30	0.122557	0.787496	227.3907	3430.058	5.028563	477.3417	1.675792
41.99715		30	0.122557	0.787496	227.3907	3430.058	5.028563	477.3417	1.675792
46.6635		30	0.122557	0.787496	227.3907	3430.058	5.028563	477.3417	1.675792
51.32985		30	0.122557	0.787496	227.3907	3430.058	5.028563	477.3417	1.675792
55.9962		30	0.122557	0.787496	227.3907	3430.058	5.028563	477.3417	1.675792
60.66255		30	1265.994	17648.69	22312.85	105383	8962.107	477.3417	1214.041
65.3289		30	1871.115	26503.87	33287.23	121401.4	12939.07	477.3417	2156.891
69.99525		30	1871.115	26503.87	33287.23	133474.8	12939.07	588.4659	2156.891
74.6616		30	1640.193	21987.24	28140.09	190676.9	10313.19	1933.494	1685.275
79.32795		30	1229.394	16065.98	19745.64	258906.3	7160.049	588.4659	1640.379
83.9943		30	822.5108	11213.53	14497.07	291936.6	4798.205	588.4659	940.4533
88.66065		30	585.7635	6168.671	6875.355	297237.3	2689.17	588.4659	411.5833
93.327		30	326.612	3819.465	4645.25	313611.7	1656.568	1741.347	254.8079
97.99335		30	179.2482	1980.751	4556.073	411968.9	867.091	1741.347	107.03
102.6597		30	119.4532	1048.957	1228.226	446356.7	458.896	588.4659	57.77888
107.3261		30	100.4064	460.6909	782.7469	516736.9	226.8769	588.4659	39.87057
111.9924		30	72.82869	460.6909	604.5702	547134.7	226.8769	588.4659	39.87057
116.6588		30	72.82869	677.4772	604.5702	547134.7	432.2313	588.4659	39.87057
121.3251		30	166.7601	1838.418	2594.675	547134.7	1145.154	477.3417	438.4633
125.9915		30	470.2695	4871.136	6131.846	493757.2	2592.381	588.4659	447.4236
130.6578		30	836.4183	9854.539	10892.77	371975.7	4268.895	972.7595	3321.852
135.3242		30	890.745	10764.01	14348.07	324510.1	4912.187	1357.053	4421.485
139.9905		30	1161.559	16272.91	18552.16	241061.1	6759.235	1357.053	4421.485
144.6569		30	1329.915	18466.95	23686.69	236604.1	8829.771	588.4659	2597.412
149.3232		30	1353.856	19047.53	23985.42	208899.2	10354.06	477.3417	1748.134
153.9896		30	1353.856	18466.95	23985.42	208899.2	8829.771	477.3417	1748.134
158.6559		30	1088.462	17241.35	18462.67	277143.6	7195.942	477.3417	1748.134
163.3223		30	694.1374	10114.57	12560.46	381915.2	4449.913	477.3417	1249.931
167.9886		30	262.7675	3293.143	3486.096	470821.7	1503.743	477.3417	371.2656
172.655		30	106.317	1294.246	1762.865	470821.7	567.3366	477.3417	44.34764
177.3213		30	106.317	1294.246	1762.865	461641.5	567.3366	477.3417	44.34764
181.9877		30	345.0501	4474.829	5745.277	392047.5	2417.633	477.3417	631.1402
186.654		30	868.2151	9782.301	13513.75	384954	5379.745	477.3417	1021.171
191.3204		30	1098.427	14647.12	19477.07	371791.7	6922.395	477.3417	1030.14
195.9867		30	1434.552	20334.85	24015.29	255990.9	10288.24	477.3417	1030.14
200.6531		30	1753.904	24441.09	29426.24	240424.3	12123.04	477.3417	935.9694
205.3194		30	1753.904	24441.09	29426.24	240424.3	12123.04	588.4659	904.5826
209.9858		30	1525.963	19533.25	21894.81	279333.9	9542.595	1357.053	886.6477

Table A11 - HC LA-ICPMS Map 1

[Click here to download Table: Table A11 - HC LA-ICPMS Map 1.xlsx](#)

x	y	Mg24	Al27	Si29	S34	K39	Ca43	Ti49	
	0	200	0.021073	0.05639	21.00587	7983.462	0.361785	21.05916	0.064138
31.109		200	0.021073	0.05639	21.00587	8047.713	0.361785	21.05916	0.064138
62.218		200	0.021073	0.05639	21.00587	8047.713	0.361785	21.05916	0.064138
93.327		200	0.021073	0.05639	21.00587	8176.23	0.361785	21.05916	0.064138
124.436		200	0.021073	0.05639	21.00587	7942.578	0.361785	26.98968	0.064138
155.545		200	0.021073	0.05639	21.00587	8176.23	0.361785	26.98968	0.064138
186.654		200	0.021073	0.05639	21.00587	7925.059	0.361785	26.98968	0.064138
217.763		200	0.021073	0.05639	21.00587	8217.125	0.361785	26.98968	0.064138
248.872		200	0.021073	0.05639	21.00587	8217.125	0.361785	26.98968	0.064138
279.981		200	0.021073	0.05639	21.00587	8316.455	0.361785	21.05916	0.064138
311.09		200	0.021073	0.05639	21.00587	8316.455	0.361785	21.05916	0.064138
342.199		200	0.021073	0.05639	21.00587	8076.919	0.361785	21.05916	0.064138
373.308		200	0.252879	9.669301	21.00587	8076.919	0.361785	21.05916	0.064138
404.417		200	0.337173	9.669301	169.5618	9070.606	0.361785	21.05916	0.064138
435.526		200	0.590066	1.888202	169.5618	9480.15	0.361785	21.05916	0.064138
466.635		200	0.337173	1.147858	169.5618	9480.15	0.361785	21.05916	0.064138
497.744		200	0.674366	1.888202	138.8281	9567.937	0.361785	21.05916	0.064138
528.853		200	0.674366	1.282456	156.1153	9567.937	0.361785	21.05916	0.064138
559.962		200	0.674366	2.69599	138.8281	9088.153	0.361785	21.05916	0.064138
591.071		200	0.590066	1.282456	133.0659	9088.153	0.361785	21.05916	0.064138
622.18		200	0.590066	1.753585	117.7008	9088.153	0.361785	21.05916	0.064138
653.289		200	0.590066	1.753585	133.0659	9445.036	0.361785	21.05916	0.064138
684.398		200	0.337173	1.753585	138.8281	9445.036	0.361785	21.05916	0.064138
715.507		200	0.337173	1.349757	138.8281	9579.642	0.361785	21.05916	0.244805
746.616		200	0.505768	1.349757	115.7803	9661.589	0.361785	21.05916	0.244805
777.725		200	0.590066	2.69599	115.7803	10182.74	0.361785	21.05916	0.244805
808.834		200	0.716519	19.18687	171.4829	11930.3	0.361785	21.05916	0.499534
839.943		200	1.138043	24.9343	179.1669	48125.56	0.465111	21.05916	1.009013
871.052		200	6.578569	30.11336	184.9302	128730.8	6.760308	21.05916	4.57553
902.161		200	7.506944	72.14052	223.355	218228.8	37.31371	21.05916	5.33982
933.27		200	7.506944	72.14052	223.355	293155.9	66.92282	21.05916	5.33982
964.379		200	4.131784	57.76923	254.0989	293155.9	66.92282	21.05916	5.33982
995.488		200	4.131784	38.89431	254.0989	240641.5	44.43938	26.98968	5.33982
1026.597		200	5.27067	38.89431	240.648	240641.5	42.16181	26.98968	5.849381
1057.706		200	7.000539	81.07334	215.6695	287756.5	42.16181	26.98968	7.123272
1088.815		200	7.295938	94.59207	202.2206	363905.9	74.81816	21.05916	6.104151
1119.924		200	8.730947	94.72953	173.4038	417374.3	120.6614	38.28493	6.104151
1151.033		200	8.815369	100.5753	165.7199	473059.4	128.515	38.28493	6.104151
1182.142		200	9.61746	100.5753	165.7199	486599.1	135.8745	49.57927	4.32076
1213.251		200	9.61746	154.2644	186.8511	491015.8	128.515	38.28493	8.142414
1244.36		200	10.54634	162.3159	200.2993	548627.6	95.44678	26.98968	6.358921
1275.469		200	11.13753	154.2644	194.5358	548627.6	95.44678	21.05916	6.358921
1306.578		200	11.17976	162.3159	236.805	540316.4	99.28188	21.05916	6.358921
1337.687		200	17.26424	127.4954	219.5122	533100.4	143.6907	21.05916	6.358921
1368.796		200	17.26424	127.4954	219.5122	533100.4	143.6907	38.28493	6.358921
1399.905		200	12.86923	127.4954	198.3781	537955.5	139.9145	49.57927	5.59459

Table A12 - HC LA-ICPMS Map 2

[Click here to download Table: Table A12 - HC LA-ICPMS Map 2.xlsx](#)

x	y	Mg24	Al27	Si29	S34	K39	Ca43	Ti49	
	0	40	0.101602	0.450701	119.1757	8693.408	2.512688	241.4314	0.599
6.2218		40	0.101602	0.450701	163.4	9512.738	3.410701	241.4314	0.599
12.4436		40	0.101602	0.460113	163.4	9512.738	3.410701	241.4314	0.599
18.6654		40	0.101602	0.460113	119.1757	9297.118	4.632453	241.4314	0.599
24.8872		40	0.101602	0.460113	119.1757	8822.77	4.632453	241.4314	0.599
31.109		40	0.101602	0.450701	119.1757	8262.232	2.887124	241.4314	0.599
37.3308		40	0.101602	0.450701	119.1757	7831.083	2.512688	241.4314	0.599
43.5526		40	0.101602	0.450701	163.4	7313.755	2.512688	241.4314	0.599
49.7744		40	0.101602	0.450701	163.4	7313.755	2.512688	241.4314	0.599
55.9962		40	0.101602	0.450701	119.1757	8952.132	2.512688	241.4314	0.599
62.218		40	0.101602	0.450701	119.1757	8952.132	2.512688	241.4314	0.599
68.4398		40	0.101602	0.450701	119.1757	8564.056	2.512688	241.4314	0.599
74.6616		40	0.101602	0.450701	119.1757	8564.056	2.538072	241.4314	0.599
80.8834		40	12.58367	91.58779	119.1757	270196.4	131.7028	241.4314	4.902656
87.1052		40	12.95427	91.58779	180.312	420106.7	206.0676	241.4314	4.902656
93.327		40	12.95427	67.12572	315.6069	420106.7	224.212	241.4314	2.391902
99.5488		40	11.47187	38.15315	349.4323	343432.6	224.212	241.4314	2.391902
105.7706		40	11.47187	38.15315	501.6528	210643.5	189.5211	241.4314	2.391902
111.9924		40	8.877727	28.80193	620.0532	210643.5	189.5211	241.4314	2.391902
118.2142		40	2.948833	25.48428	620.0532	365557.8	189.5211	241.4314	2.391902
124.436		40	2.948833	25.48428	586.2237	539354	159.2756	241.4314	7.41341
130.6578		40	1.466729	22.46848	119.1757	543847.1	91.71997	241.4314	7.41341
136.8796		40	1.466729	22.46848	119.1757	539354	69.82932	299.7973	7.41341
143.1014		40	1.466729	22.46848	119.1757	529953.1	61.42889	241.4314	4.902656
149.3232		40	5.54265	23.97637	119.1757	493249.4	58.45448	241.4314	12.43512
155.545		40	5.913191	23.97637	119.1757	493249.4	58.45448	241.4314	4.902656
161.7668		40	5.913191	13.42249	146.4893	495548.4	32.05179	241.4314	4.902656
167.9886		40	5.913191	6.187154	146.4893	495548.4	22.44253	299.7973	2.391902
174.2104		40	5.913191	6.187154	119.1757	504189.5	8.298097	241.4314	2.391902
180.4322		40	4.060456	4.679967	119.1757	504189.5	4.632453	299.7973	2.391902
186.654		40	1.466729	8.900255	119.1757	515385.4	2.512688	299.7973	4.902656
192.8758		40	1.466729	635.1262	119.1757	516185.9	2.512688	299.7973	4.902656
199.0976		40	3.689915	635.1262	119.1757	515385.4	8.123515	241.4314	2.391902
205.3194		40	5.54265	275.0799	119.1757	459011.8	9.17095	241.4314	2.391902
211.5412		40	5.54265	126.0415	119.1757	339227.9	17.37746	241.4314	0.599
217.763		40	3.319374	49.01539	146.4893	301139.1	17.37746	241.4314	0.599
223.9848		40	2.948833	12.518	146.4893	301139.1	8.996368	241.4314	0.599
230.2066		40	1.83724	12.518	119.1757	461763.9	8.996368	241.4314	0.599
236.4284		40	2.948833	12.518	119.1757	507574.2	8.996368	241.4314	0.599
242.6502		40	2.207781	11.91501	119.1757	529150.7	4.108833	241.4314	0.599
248.872		40	2.207781	5.282827	119.1757	525046	4.108833	241.4314	2.391902
255.0938		40	2.207781	5.282827	119.1757	525046	2.512688	241.4314	4.902656
261.3156		40	2.207781	5.282827	119.1757	525046	4.457913	241.4314	4.902656
267.5374		40	2.207781	12.81949	119.1757	525847.9	6.901583	241.4314	0.599
273.7592		40	1.466729	17.64369	119.1757	549859.1	6.901583	241.4314	0.599
279.981		40	1.096188	17.64369	119.1757	549859.1	8.298097	241.4314	2.391902